
Fermi-Edge Singularity and the Functional Renormalization Group

Fabian Kugler

Master's Thesis
Theoretical and Mathematical Physics



Chair of Theoretical Solid State Physics
Faculty of Physics
Ludwig-Maximilians-Universität München

Supervisor:
Prof. Dr. Jan von Delft

Munich, September 1, 2016

Abstract

We study the Fermi-edge singularity, describing the response of a degenerate electron system to optical excitation, in the framework of the functional renormalization group (fRG). Results for the (interband) particle-hole susceptibility are tested against the summation of all leading logarithmic diagrams, achieved by a solution of parquet equations. We analytically reproduce the (first-order) parquet formula by a truncation of the fRG flow, keeping four-point and higher one-particle-irreducible vertices constant, resulting in an exactly solvable system of differential equations. In the simplified case of immobile valence-band electrons (X-ray-edge singularity), corresponding to a two-level scattering impurity, the flow equations are solved numerically. We use different truncation schemes, one of which includes a fully dynamic, fermionic four-point vertex, and confront the data with the analytic result in terms of Matsubara frequencies. Examining low-order diagrams, we show that the fRG flow does not generate all parquet graphs, irrespective of performing a Hubbard-Stratonovich transformation or including photon fields to rephrase the particle-hole susceptibility as a flowing self-energy. Correspondingly, the full, analytic result originates from a fortuitous partial cancellation of diagrams, specific to the problem at hand.

Contents

1	Introduction	1
1.1	Polariton experiment	2
1.2	Qualitative understanding of Fermi-edge polaritons	3
1.3	Specification of the Fermi-edge problem	5
1.4	Theoretical background	7
2	Methods	11
2.1	Field-theoretical methods	11
2.1.1	Imaginary-time action	11
2.1.2	Superfield notation	13
2.1.3	Hubbard-Stratonovich transformation	14
2.1.4	One-particle-irreducible vertices	15
2.1.5	Schwinger-Dyson identities	16
2.2	Functional renormalization group	17
2.2.1	Regularizing procedure	19
2.2.2	Algebraic statement of the flow equations	20
2.2.3	Flow equations for the matter system	21
2.2.4	Flow equations for the light-matter system	22
2.2.5	Flow equations for the HS-transformed matter system	23
2.3	Computational considerations	24
3	Analysis	27
3.1	Perturbative calculation	28
3.2	Numerical data and diagrammatic validation	30
3.2.1	Four-point correlator in the matter system	30
3.2.2	Four-point correlator in the HS-transformed matter system	33
3.2.3	Self-energy in the light-matter system	35
3.3	Analytic results	40
3.3.1	Parquet formula from a static four-point vertex	40
3.3.2	Application for finite hole mass	42
3.4	Comparison to a related work	44
3.5	Limitations of the fRG treatment	46
4	Summary	49
A	Appendix	53
A.1	Derivation of the flow equation	53
A.2	Ladder diagrams and the crossed diagram	54
A.3	Calculations of the single-scale bubble	56

1 Introduction

The motivation for the study of Fermi-edge physics in this thesis is twofold. The advance in the experimental techniques of cavity quantum electrodynamics has renewed the need for a precise understanding of the response of degenerate Fermi systems to optical excitation. From a theoretical perspective, the study of the X-ray-edge singularity serves as “a prototype of a fermionic problem with a divergent perturbation theory” and is “instrumental in understanding more complicated problems such as the Kondo problem” [1]. Whereas a solution of the (interband) particle-hole susceptibility via so-called parquet equations amounts to extensive computational effort, only very recently, it has been suggested to perform this resummation via simple approximations in a functional-renormalization-group (fRG) scheme [2]. Before we, indeed, reproduce the (leading-order) parquet result, first obtained in 1969 [3], in a consistent way from a truncated fRG flow and critically review the underlying structure (section 3), we need to introduce a variety of theoretical techniques (section 2) and get familiar with the standard simplifications (section 1.3, 1.4). First, let us, however, go into more detail about the characteristics of the Fermi-edge problem.

Experimentally, X-ray absorption in metals has been a topic of interest for a long time. Similar measurements with infrared light can be performed using heavily doped semiconductors. Whereas photon absorption in metals typically excites a localized, deep core electron, effects due to the mobility of valence-band electrons in semiconductors can significantly alter the spectrum [4]. When a quasi-two-dimensional layer of such a semiconducting material is placed inside an optical cavity, the reversible light-matter coupling leads to the formation of half-light, half-matter excitations, attributed to the so-called polariton. We describe an experiment investigating cavity polaritons in the presence of a high-mobility sample [4] in section 1.1 and give qualitative explanations to the measurement outcomes in section 1.2.

The basic, theoretical formulation of the X-ray-edge singularity employs a localized scattering impurity, corresponding to a deep core level of a metal. In this form, the problem is exactly solvable in a one-body approach, as performed by Nozières and De Dominicis [5]. This is, however, limited to the particular situation where the scattering impurity is structureless. If the problem is tackled in a many-body treatment, the solution allows to be generalized to more complicated situations and has relevance for other problems involving logarithmic divergences. This includes not only the Kondo problem, but also the generalization to scattering processes involving a finite-mass valence-band hole, as necessary for the description of optical absorption in semiconductors.

In a diagrammatic treatment of the Fermi-edge problem, logarithmic divergences appear at all orders. Therefore, simple perturbation theory is meaningless and resummation procedures are essential. A suitable resummation can be phrased in terms of parquet equations, which consist of coupled Bethe-Salpeter equations corresponding to singular channels distinguished by parallel or antiparallel particle-hole lines. Parquet equations are used in a wide variety of theoretical applications, and it seems highly desirable to obtain equivalent resummation techniques. Whether, judging from the case study of the Fermi-edge singularity, such a technique is given by the functional renormalization group is the main concern of this work. Analytic, numeric, as well as diagrammatic arguments concerning the calculation of the particle-hole susceptibility are collected in section 3 to settle this conjecture raised by Lange et al. [2].

1.1 Polariton experiment

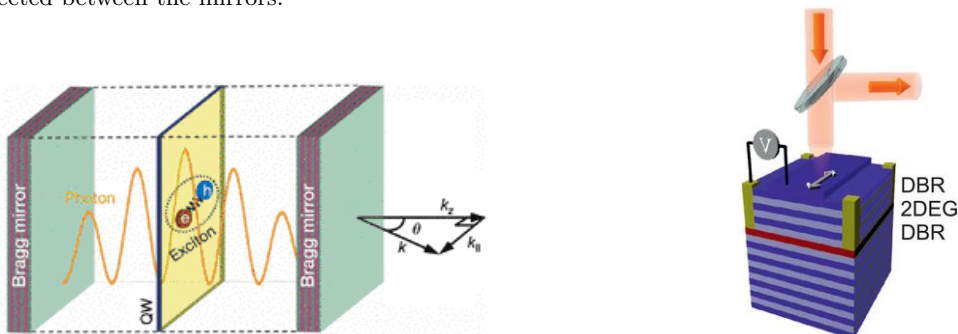
We describe a cavity-polariton experiment using the example of a publication of the Imamoğlu group in 2014 by Smolka et al. [4]. The setup employs a quantum well to confine electrons in a thin, semiconducting layer embedded in a barrier material. The surrounding microcavity, i.e., two mirrors separated by a few micrometers, is tuned to couple light primarily to the two-dimensional electron gas (2DEG) in the layer. The optical properties of this system are examined using differential reflection (dR) measurements at very low temperatures ($T = 0.2$ K).

More precisely, one considers two different 20 nm-wide GaAs samples positioned at the antinodes of the electromagnetic field in a distributed Bragg reflector (DBR) microcavity (cf. Fig. 1.1a). The electron density of each sample can be modified by applying a gate voltage between a doped top layer and the sample. White light or a tunable diode laser are used to shine on the cavity and generate reflected light, which is recorded after passing a beam splitter (cf. Fig. 1.1b). The dR spectrum is obtained by subtracting the reflection measurement, when the cavity is resonant with the optical transition in the material, from the bare cavity reflection, which is recorded when the cavity is far red-detuned. Variable tuning of the cavity is achieved by a wedged mirror geometry, providing different distances between the mirrors and, thus, varying resonance frequencies.

Differential-reflectivity spectra allow to make statements about the elementary excitations of the cavity system. Pure light excitations can be understood from a classical as well as from a quantum point of view. A cavity can be seen as a Fabry-Pérot interferometer, which sharply transmits resonant electromagnetic waves¹. Correspondingly, light at resonant frequencies excites the cavity by populating photonic eigenmodes, such that light at these frequencies is not reflected. By definition of dR, it will show up as a peak, and variable tuning of the cavity will directly shift this signal. By contrast, independent of cavity tuning, light at a frequency that induces an optical transition in the 2DEG, i.e., a matter excitation, will not be reflected.

Fig. 1.2 shows dR spectra for the two different samples in terms of energy and tuning of the cavity. Sample B exhibits a doubled electron density compared to sample A, but more importantly, an order-of-magnitude-higher mobility. For sample A, one can see clear signatures of a diagonal line, corresponding to the cavity's resonance, and a vertical

¹In a follow-up experiment by the Imamoğlu group [7] focusing on exciton-polaritons, the cavity finesse is specified to be 200, which can be interpreted as giving an estimate of how often a photon is reflected between the mirrors.



(a) Standing electromagnetic waves in the cavity induce exciton formation in the 2DEG. Figure taken from [6].

(b) Reflection measurement using a doped quantum well in a DBR cavity. Figure taken from [4].

Figure 1.1: Illustrations for a cavity-polariton experiment. Differential reflection measurements are performed on a distributed Bragg-reflector (DBR) microcavity surrounding a quasi-two-dimensional, semiconducting layer (2DEG).

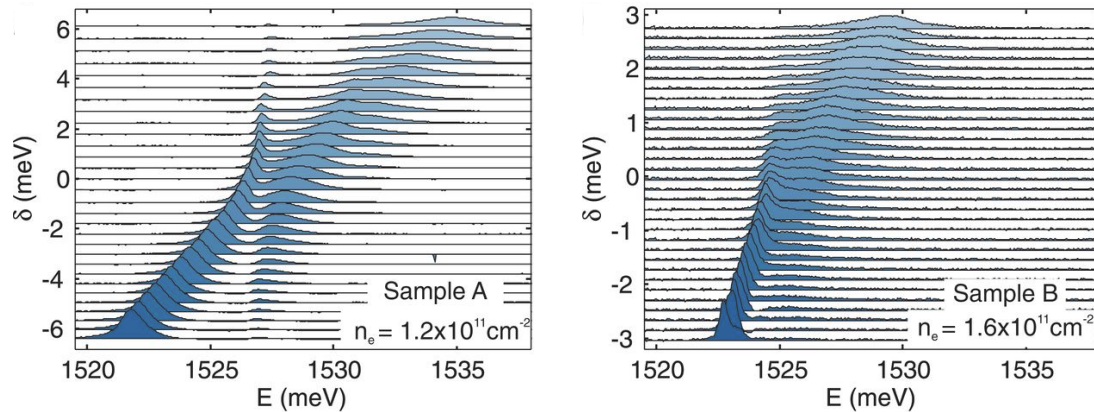


Figure 1.2: Differential reflectivity spectra for a low- (A) and high-mobility sample (B) in terms of energy E and tuning of the cavity. Detuning δ is measured as the difference of the resonance frequency of the cavity from the optical excitation energy of the semiconducting layer. Reduced mode splitting for sample B is attributed to the influence of the recoil energy of valence-band electrons. Figure taken from [4].

line for the optical transition in the material. Combined, one observes a typical avoided-crossing behavior. As light and matter excitations mix, new quasiparticles emerge, which are called polaritons². However, for sample B, there is hardly any structure on the vertical to be noted. The signal rather corresponds to a diagonal, photonic line, which is broadened for high energies. While the polariton identification in the spectrum of sample A is commonly known, the measurements for sample B provide a surprising outcome, which is attributed to the fact that the material has a high mobility. A qualitative explanation will be given next.

1.2 Qualitative understanding of Fermi-edge polaritons

The features of the measurements shown in Fig. 1.2 can be understood from a simple model of the semiconducting material. Absorption of a suitably tuned photon leads to creation of a conduction-band-electron and valence-band-hole pair. The mobility of a sample is incorporated by the effective mass of the valence band (hole mass). Low-mobility samples are approximated to have infinite hole mass, whereas mobile samples require a finite-mass description. The implications of the additional conservation of momentum for finite hole mass are already explained in the works of Mahan [8] and Gavoret et al. [9].

A heavily doped, direct-gap semiconductor at very low temperatures, such as used in the experiment explained in the previous section, is modeled by the bandstructure depicted in Fig. 1.3a, focusing on the conduction and heavy-hole valence band. The cavity is tuned close to the threshold frequency for creation of a conduction-band-electron and valence-band-hole pair. In this regime, the Fermi-liquid picture is valid and the final-state, attractive interaction between the hole and the conduction band is the dominant effect. It is the long time required for the Fermi sea to react to the new local environment, allowing conduction-band electrons to keep exchanging with the photo-excited electron, that enhances the low-frequency part of the spectrum and results in an infrared-divergent spectrum [3]. A similar effect is known from the phenomenon of Anderson orthogonality yielding a subleading contribution to the Fermi-edge singularity [10].

²The expression polariton for the quasiparticles of “hybrid light-matter nature” [6], due to Hopfield, is merged from the words polarization and photon.

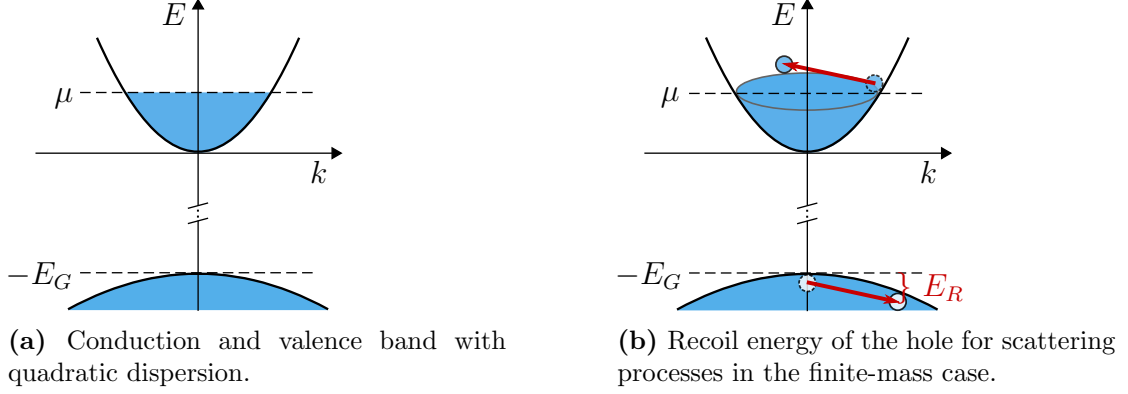


Figure 1.3: Bandstructure illustrations for a direct-gap, heavily doped semiconductor. Tuning of the cavity allows one to focus on the conduction and heavy-hole valence band in a Fermi-liquid picture. Physical parameters are the chemical potential μ , the gap energy E_G , and the recoil energy E_R of the valence-band hole.

Let us consider first an immobile sample with a single-level valence band without kinetic energy to account for. In the case of a previously empty Fermi sea (Fig. 1.4a), the photo-excited conduction electron and the valence-band hole form a hydrogenic bound state, the so-called exciton. This excitation energy is independent of the tuning of the cavity and responsible for the vertical signal, which is still visible in the middle of the energy window of the spectrum of sample A (Fig. 1.2). Excited bound states are not resolved in the spectrum; instead, for energies above the exciton line, the signal is significantly broadened. This is due to a continuum of matter excitations, which starts once the photon energy is large enough to lift an electron into the conduction band without binding to the hole. As a matter of fact, the setting for sample A is already part of the Fermi-edge regime; as a doped semiconductor, the 2DEG has a finite conduction-band filling prior to light absorption and is more comparable to the model of Fig. 1.4b. The presence of a whole Fermi sea interacting with and screening the hole results in a weaker effective interaction responsible for the bound state. Consequently, the excitonic signal in the discussed spectrum is less prominent.

Going over to sample B, we have to account for an even higher density. The increased number of conduction electrons will screen the hole even more and completely destabilize the exciton. Indeed, the vertical line is hardly to be found in the spectrum of the mobile sample in Fig. 1.2. In addition, bearing in mind the increased mobility of this sample, we have to include kinetic energy in the valence band as depicted in Fig. 1.4c. The important observation is that the transition energy in the non-interacting case (symbolized by the arrow in Fig. 1.4c), required for lifting an electron to the upper band at Fermi momentum, is not the actual threshold anymore. Interaction with conduction electrons, that scatter on top of the Fermi surface, allows the hole to decay into its zero-momentum ground state at infinitesimal energy cost. Compared to the static limit, as in the discussion of sample A, where after hole creation a conduction electron could scatter off the hole at finite momentum transfer and zero energy cost, the situation is drastically changed. In Fig. 1.3b, one can see that, at the actual absorption threshold, any interaction with the hole at finite momentum transfer costs at least the hole's kinetic energy, the so-called recoil energy. The reduced scattering phase space at low energies results in the effect that the light-absorption rate sets in slowly at this threshold. Thus, in addition to the destabilization of the exciton, sample B has a smoothly increasing absorption rate, such that the spectrum is less sharp and the mode splitting between the upper and lower polariton has vanished. We mainly see a photonic mode, which is broadened due to the continuum of matter excitations.

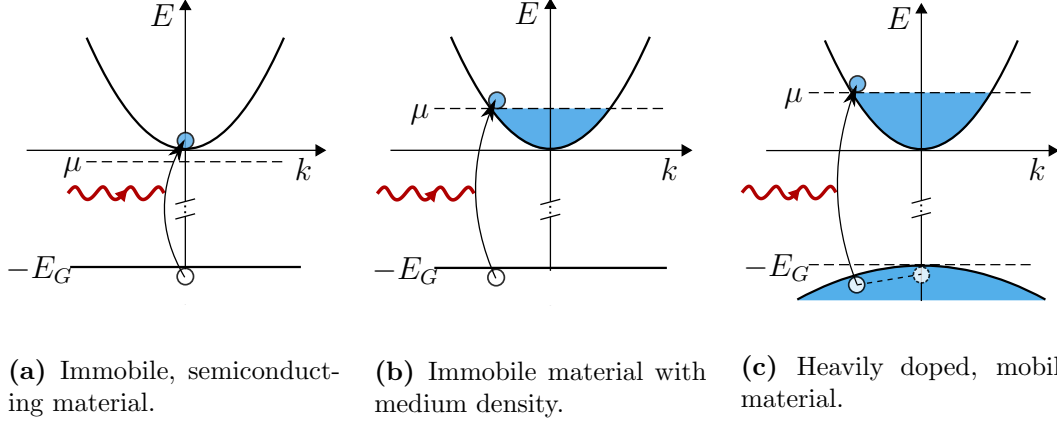


Figure 1.4: Photon absorption processes for different material settings. Without prior filling of the conduction band, the photo-excited electron and hole form a bound state. The presence of a Fermi sea in the upper band leads to screening of the interaction. Scattering of conduction electrons and the hole lower the threshold frequency by the hole recoil energy.

The above elaborated points can be very well supported by calculation of the cavity photon's self-energy in the presence of light-matter interactions, resulting in the formulae (1.8) and (1.10) for the infinite- and finite-mass case, respectively, as shown by Pimenov [11, 12]. A quantitative comparison to the experimental curves in Fig. 1.2 is, however, hardly meaningful, as a multitude of experimental parameters strike in. Even more so, the experimental situation in [4] does not correspond to a tractable theoretic regime. A 20 nm-wide sample cannot really be considered two-dimensional given an excitonic Bohr radius of similar magnitude [11]. Most importantly, the situation neither belongs to an excitonic nor Fermi-edge regime, since the excitonic binding energy is comparable to the chemical potential, both on the order of meV [11]. Nevertheless, a mathematical derivation of the physical effects, which are described above and give a qualitative understanding, is desirable, the basis for which is given in the following.

1.3 Specification of the Fermi-edge problem

The elementary excitations of the cavity system can be formally traced back to the underlying light-matter interaction. The effect of the 2DEG on the propagating photon is ultimately reduced to a property of the pure matter system [11–14]. Finding a good approximation of the relevant particle-hole susceptibility [Eq. (1.4)] is of great interest and (here) referred to as Fermi edge problem.

First, let us specify the underlying matter Hamiltonian³ for the semiconducting layer in correspondence with the standard literature on Fermi-edge singularities [3, 5, 8–10, 15]:

$$H_{\text{mat}} = \sum_{\mathbf{k}} \epsilon_{\mathbf{k}} c_{\mathbf{k}}^{\dagger} c_{\mathbf{k}} + \sum_{\mathbf{k}} E_{\mathbf{k}} d_{\mathbf{k}}^{\dagger} d_{\mathbf{k}} - \frac{1}{V} \sum_{\mathbf{k}, \mathbf{q}, \mathbf{Q}} U_{\mathbf{Q}} c_{\mathbf{k}+\mathbf{Q}}^{\dagger} c_{\mathbf{k}} d_{\mathbf{q}} d_{\mathbf{q}-\mathbf{Q}}^{\dagger}. \quad (1.1)$$

Here, conduction (valence) electrons with momentum \mathbf{k} are created by $c_{\mathbf{k}}^{\dagger}$ ($d_{\mathbf{k}}^{\dagger}$) and annihilated by $c_{\mathbf{k}}$ ($d_{\mathbf{k}}$). The Coulomb interaction, hereafter simplified to the contact type $U_{\mathbf{Q}} = U > 0$, is a final-state interaction, as it has no contribution given a full valence band. It can be understood as an attraction of all conduction electrons to a newly created hole in the valence band. The interaction excludes any Auger-type transitions, mixing three c operators with one d operator and vice versa, since interband

³The Fourier transform is defined by $f(\mathbf{x}) = \frac{1}{\sqrt{V}} \sum_{\mathbf{k}} e^{i\mathbf{k}\cdot\mathbf{x}} f_{\mathbf{k}}$, etc., where V is the volume of the material, i.e., the area of the 2D layer.

transitions are suppressed respecting the size of the band gap (E_G). Neither does it contain intraband Coulomb interaction. This, on the other hand, is contained in a Fermi-liquid picture of a renormalized band gap as well as renormalized quasiparticles. The quasiparticles are described by parabolic dispersions in an effective-mass (m , M) sense, where the bandwidth is respected by an intrinsic ultraviolet cutoff ξ_0 on the order of the Fermi energy μ :

$$\epsilon_{\mathbf{k}} = \frac{\mathbf{k}^2}{2m}, \quad E_{\mathbf{k}} = -E_G - \frac{\mathbf{k}^2}{2M}, \quad 0 \leq \epsilon_{\mathbf{k}} \leq \mu + \xi_0, \quad \xi_0 \sim \mu. \quad (1.2)$$

The Fermi-liquid picture is supposed to work well when electron energies close to the Fermi energy dominate. Furthermore, lattice effects can be neglected [5], and spin can be traced back to a few factors of 2 at the end of calculations; in fact, for a spin conserving interaction, the leading-order solution of the particle-hole susceptibility is merely affected by a doubled density of states [5]. Since our calculations will not treat any angular dependencies, the solutions are independent of space dimension. They are effectively one-dimensional, and we are allowed to consider V as a generalized volume. In two space dimensions, the (Fermi-liquid) single-spin density of states $\rho = m/(2\pi)$ is de facto constant; for three dimensions, one approximates ρ by its value at Fermi level.

Moving on to light in the cavity system, note that due to the enclosing mirrors, electromagnetic waves in the cavity can be separated into standing waves between the mirrors. The particular mode⁴ with an energy close to the optical transitions of the layer is further specified by its in-plane momentum \mathbf{q} . Next to its energy, determined by the dispersion $\omega_{\mathbf{q}}$, the light-matter interaction is of importance. It can be obtained from a minimal-coupling Hamiltonian with a few approximations [16]. First, in the rotating-wave approximation, photon processes beyond simple absorption and emission are omitted⁵. In the dipole approximation, the electromagnetic polarization vector is considered constant over the scale of the unit cell⁶. If the material has a dipole moment $-M_{\mathbf{q}}$, the Hamiltonian (with creation and annihilation operators a^\dagger , a of a photon) describing light in the cavity and its interaction to matter is given by

$$H_{\text{light-mat}} = \sum_{\mathbf{q}} \omega_{\mathbf{q}} a_{\mathbf{q}}^\dagger a_{\mathbf{q}} + \frac{1}{\sqrt{V}} \sum_{\mathbf{p}, \mathbf{q}} (iM_{\mathbf{q}} c_{\mathbf{p}+\mathbf{q}}^\dagger d_{\mathbf{p}} a_{\mathbf{q}} + \text{h.c.}). \quad (1.3)$$

As already mentioned, the combined quasiparticle responsible for the elementary excitations of the microcavity system is the polariton. The polariton, on the other hand, is nothing but the photon dressed by its interaction to matter [6]. As elementary excitations can then be deduced from the polariton spectral function, it is sufficient to calculate the photon self-energy. For simplifying reasons, the photon self-energy will only be calculated in leading order in the light-matter coupling. This can be motivated as in [12]: In a regime where $\rho|M_0|^2 \ll \mu$, photon absorption and emission happens on a much larger timescale than electronic processes. Thus, photo-excited electron-hole pairs are hardly altered by intermediate photon propagation, and the leading contribution to the photon self-energy is dominant. With standard perturbation methods, it is found⁷

⁴The eigenenergies are separated on a scale c/L ($\hbar = 1$), which is sufficiently large for a cavity size L of a few micrometers.

⁵This is supposed to be accurate, particularly for III-V based samples [6].

⁶Since the typical length scale of the electron dynamics is much shorter than the in-plane optical wavelength, the light-matter interaction is usually approximated with its zero-momentum behavior [6]. In fact, in an effective-mass description of the photon due to spatial confinement [6], the wavelength associated to the in-plane momentum is much larger than the resonant wavelength between the mirrors, which is already on the order of micrometers.

⁷The corresponding relation in frequency space will be explicitly derived within the Matsubara formalism in section 2.1.

that the leading-order self-energy is given by $|M_{\mathbf{q}}|^2 \Pi^\gamma(t, \mathbf{q})$, where⁸

$$i\Pi^\gamma(t, \mathbf{q}) = \frac{1}{V} \sum_{\mathbf{k}, \mathbf{p}} \langle \mathcal{T} d_{\mathbf{k}}^\dagger(t) c_{\mathbf{k}+\mathbf{q}}(t) c_{\mathbf{p}+\mathbf{q}}^\dagger(0) d_{\mathbf{p}}(0) \rangle . \quad (1.4)$$

The effect of light-matter interaction on the photon is reduced to a correlation function of the fermionic system. The correlation function describes a conduction-valence-band particle-hole pair in the interacting system; for positive times, a valence-band hole is initially created, and the final-state interaction of Eq. (1.1) has a crucial effect. The quantity Π^γ is the particle-hole susceptibility to be calculated in the Fermi-edge problem. By abuse of notation, we will also refer to it as photon self-energy (irrespective of its dimension). The form of the Hamiltonian [Eq. (1.1)] and the band structure (cf. Fig. 1.3a) have several a priori implications for the calculation of the particle-hole susceptibility, which will be elucidated next.

1.4 Theoretical background

In this section, we list typical simplifications made in a diagrammatic treatment of the Fermi-edge singularity. The first aspect already influenced the specification of the Hamiltonian in the previous section: The band gap dominates all other energy scales and is considered as an experimental parameter. This allowed us to restrict the interaction to be particle-number-conserving for two different fermion species. Whereas we are ignorant towards the precise position of the absorption threshold, we focus on the shape of the singularity in the response function at this particular threshold. Secondly, we confine ourselves to summing only those diagrams with the leading logarithmic divergence (leading log. diagrams). Depending on whether we consider a finite or infinite valence-band (hole) mass, this has different consequences. Let us give the arguments along the lines of the standard literature in more detail.

Large, renormalized gap energy: The interacting four-point correlator, upon expansion in the interaction and using Wick's theorem, is traced back to two-point Green's functions⁹. All correlation functions are expectation values of operators with respect to certain states. Irrespective of considering a ground-state expectation value or a thermal average, one only considers states with a full valence band, the reason being that the gap energy, separating both bands, is the largest energy scale and by far larger than the available thermal energy¹⁰. Various simplifications immediately follow: First, a valence-band Green's function is purely advanced. For a time difference t , using the Heaviside step function Θ and the time-ordered expectation value as before, it is given by

$$iG_{\mathbf{k}}^d(t) = \langle \mathcal{T} d_{\mathbf{k}}(t) d_{\mathbf{k}}^\dagger(0) \rangle \propto \Theta(-t) . \quad (1.5)$$

For positive times, the creation operator $d_{\mathbf{k}}^\dagger$ applied to a state with full valence band gives vanishing contribution. By the same argument, the particle-hole susceptibility, defined in Eq. (1.4), is automatically retarded.

Concerning fermionic self-energies, for both bands, there is always the constant Hartree contribution proportional to the electronic density of the other band. We consider such a contribution already contained in the renormalized gap. Moreover, since we only consider an attractive Coulomb interaction between conduction-band electrons and

⁸The following expression is a purely fermionic, time-ordered expectation value (with time-ordering operator \mathcal{T}) of operators in the Heisenberg picture, such that $d_{\mathbf{k}}(t) = e^{iH_{\text{mat}}t} d_{\mathbf{k}} e^{-iH_{\text{mat}}t}$, etc.

⁹This is done within the Matsubara formalism and up to second order in U in section 3.1.

¹⁰Typically, one has $E_G \sim \text{eV}$ ($E_G = 1.518 \text{ eV}$ for GaAs, table 8.2 in [17]), whereas $k_B T \sim 0.1 \text{ meV}$ for $T = 0.4 \text{ K}$ as in the experiment [4].

valence-band holes, any diagram with a closed d loop is proportional to the (valence-band) hole density in the averaging state, which is zero. Importantly, there are no further contributions to the conduction-band self-energy. Any higher-order diagram contains d propagators with positive and negative time arguments and consequently vanishes [cf. Eq. (1.5)]. Summarizing, in diagrammatic calculations, c propagators stay bare and the Hartree part of the valence-band self-energy is irrelevant. There are no closed valence-band loops and, therefore, no kind of closed loops at all in diagrams for the particle-hole susceptibility.

Leading log. summation: We have already mentioned that the particle-hole susceptibility of the Fermi-edge problem is logarithmically divergent. There repeatedly appear terms of the type ($n, p \in \mathbb{N}_0$)

$$u^n \left[\ln \left(\frac{\xi_0}{|\omega - \omega_0|} \right) \right]^{n-p}, \quad u = \rho U. \quad (1.6)$$

Here, u , the coupling constant, is much smaller than one¹¹. With ω_0 being the threshold frequency and ξ_0 the intrinsic UV cutoff [cf. Eq. (1.2)], the logarithm, on the other hand, constitutes a diverging quantity. Diagrammatic calculations in the Fermi-edge problem are usually done with logarithmic accuracy. This means that one takes into account terms with the largest power of the logarithm in Eq. (1.6) only; contributions with $p > 0$ are negligible. In particular, next to a logarithmically diverging term, contributions of order 1 are negligible, which includes factors in the argument of the logarithm. For different types of diagrams, the cutoff, which in Eq. (1.6) is given by ξ_0 , corresponds to the number of filled or empty states in the conduction band. In the simplified case of a half-filled band [cf. Eq. (1.2)], in both cases, the constant is $\xi_0 = \mu$. Modifications to that, still in the regime of a large Fermi energy and a large number of unoccupied states, have minor effects in the given accuracy.

The product of the small coupling constant and the logarithmically diverging factor still diverges for small enough frequencies $\tilde{\omega}$ (measured from the threshold frequency). Only in the intermediate regime $u \ln \xi_0 / \tilde{\omega} \lesssim 1$ can the subleading term be neglected a priori, viz., $u^2 \ln \xi_0 / \tilde{\omega} \ll 1$. Further comments are separately given for infinite and finite hole mass.

Ladder diagrams: In an early work, Mahan [8] used a summation of ladder diagrams to approximate the particle-hole susceptibility. In such a rigid-Fermi-sea approximation, no conduction-band holes are allowed. Higher-order diagrams factorize into a sequence of bare particle-hole bubbles carrying the external energy-momentum. A number of n consecutive interactions lead to a contribution to the particle-hole susceptibility (at zero external momentum) of¹² (cf. section A.2)

$$\Pi^{(n,L)}(\omega) = (-u)^n \left[\ln \left(\frac{-(\omega - \omega_0) - i0^+}{\xi_0} \right) \right]^{n+1}, \quad \xi_0 \gg \omega - \omega_0. \quad (1.7)$$

A geometric series, irrespective of the infinitesimal nature of 0^+ , directly leads to a bound state, the so-called Mahan exciton, at an energy $-E_B = \omega_B - \omega_0 = -\xi_0 \exp(-1/u)$. It is physically transparent that such a bound state in the middle of a filled band would immediately be broadened. In fact, in our regime of interest¹³, $\mu \gg E_B$, the Fermi-sea shakeup, manifested by diagrams containing conduction-band holes, reduces the weight

¹¹If the interaction parameter is deduced from screened Coulomb interaction, one typically has $u \sim 0.1 \dots 0.5$ for metals [3] and $u \sim 0.1 \dots 0.2$ for semiconductors [9].

¹²The following equation is the infinite-mass result. For finite mass (close to the direct threshold), the logarithm is divided by $1 + m/M$ and ξ_0 multiplied by the same expression [8,9].

¹³For a treatment of the opposite case, $\mu \ll E_B$, see [12].

of ladder diagrams and eliminates the δ peak. In a following publication, Mahan [15] hinted at this by explicitly calculating the lowest-order diagrams for infinite hole mass. The first diagram which contains a conduction-band hole is called the crossed diagram, since, with propagating interaction lines, it can be drawn to have two crossed ones of these. With logarithmic accuracy, it can be shown to give $-1/3$ of the contribution of the second-order ladder diagram (cf. section A.2), and, thus, forms the lowest-order graph to reduce the divergence of the ladder diagrams. Let us first consider the infinite-mass case in more detail.

Infinite hole mass: Roulet et al. [3] have achieved a summation of all leading log. diagrams for the particle-hole susceptibility via a solution of parquet equations. This parquet technique classifies diagrams according to whether they are reducible in the parallel or antiparallel channel, i.e., whether they can be separated into two valid diagrams upon cutting (anti)parallel c , d lines. Relating these contributions self-consistently via coupled Bethe-Salpeter equations, one has to insert the totally irreducible vertex (irreducible in both channels). The first-order parquet solution, corresponding to the leading log. summation, is obtained when the irreducible vertex is taken to be at lowest order and reads

$$\Pi^\gamma(\omega) = \frac{1}{2U} \left[1 - \left(\frac{-(\omega - \omega_0) - i0^+}{\xi_0} \right)^{-2u} \right], \quad \omega_0 = E_G + \mu. \quad (1.8)$$

Corrections to it are of lower logarithmic singularity. Similarly, it can easily be shown that the valence-band self-energy (reduced from its Hartree contribution) behaves at lowest order as $u^2 \tilde{\omega} \ln \xi_0 / \tilde{\omega}$ and is hence not needed for summing up the relevant diagrams. In a later work, Nozières et al. [10] showed that including these subleading divergences does not alter the first-order parquet result. The validity thus appears to hold for all frequencies and not just where $u \ln \xi_0 / \tilde{\omega} \lesssim 1$. The one-body solution of Nozières and De Dominicis [5] gives an exact result, adding u^2 with respect to u corrections.

In total, the initial parquet calculation gives a very good understanding of the shape of the singularity following a power law. The contributing parquet graphs, being the appropriate extension to two channels compared to the ladder summation in a single channel, can be obtained by successively inserting parallel and antiparallel bubbles for the bare vertex [3]. The logarithmic divergence of these bubbles with opposite sign underlies the first-order parquet solution.

Finite hole mass: For finite hole mass, the situation is more complicated. We have already explained that different thresholds appear. A photon can already be absorbed at the indirect threshold, coinciding with the infinite-mass threshold, $\omega_I = E_G + \mu$, where the problem is totally perturbative and easily described [9, 11]. At the direct threshold $\omega_D = \omega_I + b\mu$, b being the mass ratio m/M , logarithmic divergences appear as for infinite hole mass and a resummation is needed. The crucial difference is that, at this direct threshold, the valence-band hole is not in its ground state and underlies significant influence of its self-energy. In fact, it can be shown [11] that the value of the self-energy at Fermi momentum and on-shell is of the form $\Sigma^d \sim u^2 b \mu$. Including this self-energy in, e.g., the ladder diagrams cuts the coupling-times-logarithm product at a maximal value $u \ln(u^2 b)$. A necessity for resummation is only given when $u |\ln b| \sim 1$, i.e., when b is exponentially small in the coupling, $b \sim \exp(-1/u)$. Otherwise, higher-order diagrams are totally negligible. For exponentially small coupling, logarithmic terms in the calculation of non-ladder diagrams can be simplified according to $\ln(u^2 b) \sim \ln b$ —as $|\ln u| \ll |\ln b|$ —and the contribution of the crossed diagram (at zero external momentum) is shown [11] to be analogous to the infinite-mass case:

$$\Pi^{(2,C)}(\omega, 0) = -\frac{1}{3} \Pi^{(2,L)}(\omega, 0), \quad \text{when } \ln(u^2 b) \sim \ln b. \quad (1.9)$$

Setting up a Bethe-Salpeter equation similar to the infinite-mass scenario, an approximate solution yields [9,11]

$$\text{Re } \Pi^\gamma(\omega, 0) = \frac{1}{2U} \left[1 - \left(\frac{\max\{|\omega - \omega_D|, b\mu\}}{\xi_0} \right)^{-2u} \right]. \quad (1.10)$$

The power-law behavior for $|\omega - \omega_D| \gg b\mu$ is unchanged. However, the singularity is cut off by the recoil energy of the valence-band hole.

Having collected numerous background information, it is time to develop the theoretical tools distinct to our analysis of the Fermi-edge singularity. It is not until section 3 that we gain results from the functional-renormalization-group formalism—to be established in section 2.2—and come back to the parquet formulae (1.8) and (1.10).

2 Methods

Our treatment of the Fermi-edge singularity is based on the functional renormalization group, which itself is most easily devised in an imaginary-time action formalism. The fRG framework has proven to work very well for problems with infrared divergences and will be our means to approximately compute correlation functions, viz., the particle-hole susceptibility or photon self-energy [Eq. (1.4)]. Before we state the flow equations central to fRG in section 2.2, we will briefly recapitulate the standard field-theoretical methods which we make use of in order to familiarize the reader with the notation and conventions.

2.1 Field-theoretical methods

In condensed-matter physics, it is common to work with second-quantized Hamiltonians as well as imaginary-time actions. The action formalism allows to derive identities and perform transformations very naturally, one of the latter being the Hubbard-Stratonovich transformation, which introduces auxiliary fields into the theory. Such a theory with different types of particles can be compactly phrased using a superfield notation. Next to these aspects, we shall define a generating functional for one-particle-irreducible vertices, as this is a central quantity in the chosen implementation of an exact renormalization group treatment.

2.1.1 Imaginary-time action

Given a normal-ordered¹⁴ Hamiltonian of a system of indistinguishable particles in terms of creation and annihilation operators with quantum numbers i , $H(\{\psi_i^\dagger\}, \{\psi_i\})$, it is well known that the grand-canonical partition function has a functional-integral representation of the form

$$Z = \text{Tr} e^{-\beta(H - \mu N)} = \int \mathcal{D}[\{\bar{\psi}_i\}, \{\psi_i\}] e^{-S[\{\bar{\psi}_i\}, \{\psi_i\}]} . \quad (2.1)$$

Here, $\beta = 1/(k_B T)$ is the inverse of temperature multiplied by the Boltzmann constant, μ the chemical potential, N the number operator, and S the imaginary-time action given by

$$S[\{\bar{\psi}_i\}, \{\psi_i\}] = \int_0^\beta d\tau \sum_i \bar{\psi}_i(\tau) \partial_\tau \psi_i(\tau) + (H - \mu N)[\{\bar{\psi}_i(\tau)\}, \{\psi_i(\tau)\}] . \quad (2.2)$$

In this representation, $\bar{\psi}_i(\tau)$ and $\psi_i(\tau)$ are complex (bosons) or Grassmann (fermions) fields, corresponding to the operators ψ_i^\dagger, ψ_i and depending on imaginary time τ in the interval $[0, \beta)$. Furthermore, bosonic fields are periodic and fermionic fields antiperiodic, such that we can define a frequency representation

$$\psi_i(\tau) = \frac{1}{\sqrt{\beta}} \sum_\omega \psi_{i,\omega} e^{-i\omega\tau} =: \frac{1}{\sqrt{\beta}} \int_\omega \psi_{i,\omega} e^{-i\omega\tau} , \quad \bar{\psi}_i(\tau) = \frac{1}{\sqrt{\beta}} \int_\omega \bar{\psi}_{i,\omega} e^{i\omega\tau} . \quad (2.3)$$

¹⁴Here, normal ordering means to bring all creation operators to the left of any annihilation operator.

The so-called Matsubara frequencies ω run over $\pi/\beta \cdot 2\mathbb{Z}$ for bosons and $\pi/\beta \cdot (2\mathbb{Z} + 1)$ for fermions. Consequently, a Matsubara sum with prefactor $1/\beta$ (henceforth encoded in a primed integral sign) translates in the limit of zero temperature (given an integrable function) into

$$\frac{1}{\beta} \int_{\omega} \psi_{\omega} =: \int'_{\omega} \psi_{\omega}, \quad \lim_{\beta \rightarrow \infty} \int'_{\omega} \psi_{\omega} = \int_{-\infty}^{\infty} \frac{d\omega}{2\pi} \psi(\omega). \quad (2.4)$$

The crucial point is that expectation values of fields in terms of Matsubara frequencies relate to real-frequency correlation functions via an analytic continuation. A general (field) correlator (corresponding to a time-ordered expectation value of operators) is defined via

$$\langle \psi_i \cdots \psi_j \rangle := \frac{1}{Z} \int \mathcal{D}[\{\bar{\psi}_i\}, \{\psi_i\}] \psi_i \cdots \psi_j e^{-S[\{\bar{\psi}_i\}, \{\psi_i\}]}. \quad (2.5)$$

Now, consider, e.g., the four-point correlator relevant for the photon self-energy. Using the fields \bar{c}, c for the conduction and \bar{d}, d for the valence band, one transforms from Matsubara to real frequencies according to

$$\int'_{\omega, \nu} \langle \bar{d}_{\omega} d_{\nu} \bar{c}_{\bar{\omega} + \nu} c_{\bar{\omega} + \omega} \rangle = \Pi^{\gamma}(\bar{\omega}, \mathbf{q}) \xrightarrow{i\bar{\omega} \rightarrow \omega + i0^+} \Pi^{\gamma}(\omega, \mathbf{q}) = \int dt e^{i\omega t} \Pi^{\gamma}(t, \mathbf{q}), \quad (2.6)$$

where the (automatically retarded) particle-hole susceptibility $\Pi^{\gamma}(t, \mathbf{q})$ was defined in Eq. (1.4). Note that we use arguments to distinguish different functions and have further adopted a condensed notation, in which field indices label both Matsubara frequency and momentum¹⁵.

For the problem at hand, the matter Hamiltonian from Eq. (1.1) is not normal-ordered yet. With the standard anticommutation relation, changing the order of d and d^{\dagger} yields an opposite sign in the interaction and a shifted dispersion $\epsilon_{\mathbf{k}} - U_{\mathbf{Q}=0}$ in the quadratic part of the conduction electrons. Now that one has a repulsion between electrons instead of an attraction between electrons and holes, the shift accounts for the interaction between the conduction electrons and the whole valence band. In our treatment, such a shift is already contained in the renormalized band gap, and we can readily move on to the appropriate action

$$S_{\text{mat}} + S_{\text{int}} = \int_{\omega} (\xi_k^c - i\omega) \bar{c}_{\omega} c_{\omega} + \int_{\omega} (\xi_k^d - i\omega) \bar{d}_{\omega} d_{\omega} + \frac{U}{\beta V} \int_{\omega, \nu, \bar{\omega}} \bar{c}_{\omega + \bar{\omega}} c_{\omega} \bar{d}_{\nu - \bar{\omega}} d_{\nu}, \quad (2.7)$$

where the quartic part has been assigned to S_{int} for future purposes. Note that, again, single indices label frequencies and momenta. The bare propagators can be read off to be $G_{0, \omega}^{c/d} = 1/(i\omega - \xi_k^{c/d})$, with $\xi_k^c = \epsilon_k - \mu$ and $\xi_k^d = E_k - \mu$, $k = |\mathbf{k}|$.

The photonic Hamiltonian from Eq. (1.3) leads to an additional action

$$S_{\text{light}} + S_{\text{light-mat}} = \int_{\bar{\omega}} (\omega_{\mathbf{q}} - i\bar{\omega}) \bar{a}_{\bar{\omega}} a_{\bar{\omega}} + \frac{i}{\sqrt{\beta V}} \int_{\bar{\omega}} (M_{\bar{\omega}} \bar{A}_{\bar{\omega}} a_{\bar{\omega}} - M_{\bar{\omega}}^* A_{\bar{\omega}} \bar{a}_{\bar{\omega}}), \quad (2.8)$$

with

$$M_{\bar{\omega}} = M(\mathbf{q}), \quad A_{\bar{\omega}} = \int_{\omega} \bar{d}_{\omega} c_{\bar{\omega} + \omega}. \quad (2.9)$$

For dimensional reasons, let us transform the complex photon fields \bar{a}, a . Propagators and self-energy, for symmetry reasons diagonal in the energy-momentum coordinate, transform accordingly:

$$\gamma_{\bar{\omega}} = M_{\bar{\omega}} a_{\bar{\omega}}, \quad \bar{\gamma}_{\bar{\omega}} = M_{\bar{\omega}}^* \bar{a}_{\bar{\omega}} \Rightarrow G_{(0, \bar{\omega})}^{\gamma} = |M_{\bar{\omega}}|^2 G_{(0, \bar{\omega})}^a, \quad \Pi_{\bar{\omega}}^{\gamma} = |M_{\bar{\omega}}|^{-2} \Pi_{\bar{\omega}}^a. \quad (2.10)$$

¹⁵In such cases, the index $\bar{\omega}$ actually stands for $(\bar{\omega}, \mathbf{q})$, and $\int_{\bar{\omega}}$ for $\int_{\bar{\omega}, \mathbf{k}}$. Each prime represents one factor of $1/(\beta V)$ in analogy to Eq. (2.4). Bosonic Matsubara frequencies are denoted by a bar.

The effect on the functional-integral measure will be canceled in any correlation function. In most cases, one is interested in the ($\mathbf{q} = 0$) case anyway, and considers a constant matrix element. The desired effect is that we have the simplified action

$$S_{\text{light}} + S_{\text{light-mat}} = - \int_{\bar{\omega}} G_{0,\bar{\omega}}^{\gamma,-1} \bar{\gamma}_{\bar{\omega}} \gamma_{\bar{\omega}} + \frac{i}{\sqrt{\beta V}} \int_{\bar{\omega}} (\bar{A}_{\bar{\omega}} \gamma_{\bar{\omega}} - A_{\bar{\omega}} \bar{\gamma}_{\bar{\omega}}). \quad (2.11)$$

Due to the factor $|M|^2$ the propagator G_0^γ is very small; intermediate photon propagation is suppressed. In fact, the leading-order photon self-energy is recovered in the transformed quantities when the limit $|M|^2 \rightarrow 0$ is considered:

$$\begin{aligned} \Pi_{\bar{\omega}}^\gamma &= \lim_{G_{0,\bar{\omega}}^\gamma \rightarrow 0} (G_{0,\bar{\omega}}^\gamma)^{-2} (G_{\bar{\omega}}^\gamma - G_{0,\bar{\omega}}^\gamma) = - \lim_{G_{0,\bar{\omega}}^\gamma \rightarrow 0} (G_{0,\bar{\omega}}^\gamma)^{-2} (\langle \gamma_{\bar{\omega}} \bar{\gamma}_{\bar{\omega}} \rangle_\gamma - G_{0,\bar{\omega}}^\gamma) \\ &= - \lim_{G_{0,\bar{\omega}}^\gamma \rightarrow 0} (G_{0,\bar{\omega}}^\gamma)^{-2} \int_{\bar{\nu}, \bar{\eta}} \langle \gamma_{\bar{\omega}} \bar{\gamma}_{\bar{\omega}} \left(\frac{-i}{\sqrt{\beta V}} \bar{A}_{\bar{\nu}} \gamma_{\bar{\nu}} \right) \left(\frac{i}{\sqrt{\beta V}} A_{\bar{\eta}} \bar{\gamma}_{\bar{\eta}} \right) \rangle \\ &= - \frac{1}{\beta V} \langle A_{\bar{\omega}} \bar{A}_{\bar{\omega}} \rangle = \int'_{\omega, \nu} \langle \bar{d}_\omega d_\nu \bar{c}_{\bar{\omega}+\nu} c_{\bar{\omega}+\omega} \rangle. \end{aligned} \quad (2.12)$$

Here, we made use of Wick's theorem and the fact that higher orders in the expansion of $\exp(-S_{\text{light-mat}})$ vanish after taking $G_0^\gamma \rightarrow 0$. Whereas the first expectation value was a correlation function in presence of the interacting photon field, the following averages are to be taken without $S_{\text{light-mat}}$. In the final form, similarly as in Eq. (1.4), the photon—decoupled and immediately integrated out—is of no more relevance.

2.1.2 Superfield notation

In a theory with both fermionic and bosonic fields, it is useful to introduce the notation of so-called superfields Φ . A superfield carries a multi-index α , which specifies the field type, conjugation, and all further quantum numbers. The partition function Z is compactly stated as

$$Z = \int \mathcal{D}[\Phi] e^{-S[\Phi]}, \quad S[\Phi] = S_0[\Phi] + S_1[\Phi]. \quad (2.13)$$

Here, the action S is written in a way to single out the quadratic part S_0 . Nevertheless, as there is no restriction on S_1 , we maintain full generality by specifying

$$S_0[\Phi] = -\frac{1}{2} (\Phi, G_0^{-1} \Phi) := -\frac{1}{2} \int_\alpha \int_{\alpha'} \Phi_\alpha [G_0^{-1}]_{\alpha\alpha'} \Phi_{\alpha'}. \quad (2.14)$$

In the case of two species of electrons (c and d) and full detail, this unfolds to

$$\begin{aligned} S_0[\Phi] &= -\frac{1}{2} \int_{\omega, \mathbf{k}} (c_{\omega, \mathbf{k}}, \quad \bar{c}_{\omega, \mathbf{k}}, \quad d_{\omega, \mathbf{k}}, \quad \bar{d}_{\omega, \mathbf{k}}) \\ &\quad \text{diag} \left(\left[\begin{array}{cc} 0 & -G_{0, \omega, \mathbf{k}}^{c, -1} \\ G_{0, \omega, \mathbf{k}}^{c, -1} & 0 \end{array} \right], \left[\begin{array}{cc} 0 & -G_{0, \omega, \mathbf{k}}^{d, -1} \\ G_{0, \omega, \mathbf{k}}^{d, -1} & 0 \end{array} \right] \right) \begin{pmatrix} c_{\omega, \mathbf{k}} \\ \bar{c}_{\omega, \mathbf{k}} \\ d_{\omega, \mathbf{k}} \\ \bar{d}_{\omega, \mathbf{k}} \end{pmatrix}. \end{aligned} \quad (2.15)$$

When the superfield index specifies a fermionic field, two superfields anticommute; for bosons they commute. Regarding the quadratic action, we have to demand $G_{0, \alpha\beta} = \zeta_\alpha G_{0, \beta\alpha}$, where ζ_α is -1 for fermions and 1 for bosons. A single-particle propagator is given by

$$G_{\alpha_1 \alpha_2} = -\langle \Phi_{\alpha_1} \Phi_{\alpha_2} \rangle = -\frac{1}{Z} \int \mathcal{D}[\Phi] \Phi_{\alpha_1} \Phi_{\alpha_2} e^{-S[\Phi]}, \quad (2.16)$$

which can read, e.g.,

$$G_{\omega, \mathbf{k}}^c = G_{(c, \omega, \mathbf{k})(\bar{c}, \omega, \mathbf{k})} = -\langle c_{\omega, \mathbf{k}} \bar{c}_{\omega, \mathbf{k}} \rangle. \quad (2.17)$$

2.1.3 Hubbard-Stratonovich transformation

Under certain circumstances, it can be helpful to introduce auxiliary fields into the theory. In particular, quartic terms in the action can be converted to quadratic terms multiplied by an auxiliary field, with the help of the so-called Hubbard-Stratonovich (HS) transformation. The underlying property is

$$\int_{\mathbb{R}} dx e^{-x^2} = \int_{\mathbb{R}} dx e^{-(x+c)^2} \quad \forall c \in \mathbb{C} , \quad (2.18)$$

and, consequently,

$$\int_{\mathbb{C}} dz d\bar{z} e^{-\bar{z}z} = \int_{\mathbb{C}} dz d\bar{z} e^{-(\bar{z}+a)(z+b)} \quad \forall a, b \in \mathbb{C} . \quad (2.19)$$

From now on, we use the freedom in the definition of the functional-integral measure $\mathcal{D}[\Phi]$ by setting a constant such that the functional integral with only the quadratic part $S_0[\Phi]$ of the action gives unity. A HS transformation then looks as follows ($U_x > 0$, $\gamma_x \in \mathbb{R}$),

$$\begin{aligned} e^{\int_{\bar{\omega}} U_x \gamma_x^2 \bar{A}_{\bar{\omega}} A_{\bar{\omega}}} &= \int \mathcal{D}[\bar{\chi}, \chi] e^{-\int_{\bar{\omega}} \bar{\chi}_{\bar{\omega}} U_x^{-1} \chi_{\bar{\omega}}} e^{\int_{\bar{\omega}} U_x \gamma_x^2 \bar{A}_{\bar{\omega}} A_{\bar{\omega}}} \\ &= \int \mathcal{D}[\bar{\chi}, \chi] e^{-\int_{\bar{\omega}} (\bar{\chi}_{\bar{\omega}} + \gamma_x U_x \bar{A}_{\bar{\omega}}) U_x^{-1} (\chi_{\bar{\omega}} + \gamma_x U_x A_{\bar{\omega}})} e^{\int_{\bar{\omega}} U_x \gamma_x^2 \bar{A}_{\bar{\omega}} A_{\bar{\omega}}} \\ &= \int \mathcal{D}[\bar{\chi}, \chi] e^{-\int_{\bar{\omega}} U_x^{-1} \bar{\chi}_{\bar{\omega}} \chi_{\bar{\omega}} + \gamma_x (A_{\bar{\omega}} \bar{\chi}_{\bar{\omega}} + \bar{A}_{\bar{\omega}} \chi_{\bar{\omega}})} , \end{aligned} \quad (2.20)$$

for a repulsive interaction between \bar{A} and A . An attractive interaction can be transformed via ($U_p > 0$, $\gamma_p \in \mathbb{R}$)

$$\begin{aligned} e^{-\int_{\bar{\omega}} U_p \gamma_p^2 \bar{B}_{\bar{\omega}} B_{\bar{\omega}}} &= \int \mathcal{D}[\bar{\psi}, \psi] e^{-\int_{\bar{\omega}} \bar{\psi}_{\bar{\omega}} U_p^{-1} \psi_{\bar{\omega}}} e^{-\int_{\bar{\omega}} U_p \gamma_p^2 \bar{B}_{\bar{\omega}} B_{\bar{\omega}}} \\ &= \int \mathcal{D}[\bar{\psi}, \psi] e^{-\int_{\bar{\omega}} (\bar{\psi}_{\bar{\omega}} + i\gamma_p U_p \bar{B}_{\bar{\omega}}) U_p^{-1} (\psi_{\bar{\omega}} + i\gamma_p U_p B_{\bar{\omega}})} e^{-\int_{\bar{\omega}} U_p \gamma_p^2 \bar{B}_{\bar{\omega}} B_{\bar{\omega}}} \\ &= \int \mathcal{D}[\bar{\psi}, \psi] e^{-\int_{\bar{\omega}} U_p^{-1} \bar{\psi}_{\bar{\omega}} \psi_{\bar{\omega}} + i\gamma_p (B_{\bar{\omega}} \bar{\psi}_{\bar{\omega}} + \bar{B}_{\bar{\omega}} \psi_{\bar{\omega}})} . \end{aligned} \quad (2.21)$$

Here, $\bar{\chi}$, χ and $\bar{\psi}$, ψ are complex fields, which describe bosonic degrees of freedom. With the simplifying choice of a constant interaction (U_x , U_p), as opposed to physical fields, χ and ψ have a constant bare propagator. In order to eliminate an interaction term comprising four fermionic fields, A and B might be chosen to contain two of them. In our case, we wish to eliminate the interaction

$$S_{\text{int}} = \frac{U}{\beta V} \int_{\omega, \nu, \bar{\omega}} \bar{c}_{\omega+\bar{\omega}} c_{\omega} \bar{d}_{\nu-\bar{\omega}} d_{\nu} = -\frac{U_x}{\beta V} \int_{\bar{\omega}} \bar{A}_{\bar{\omega}} A_{\bar{\omega}} + \frac{U_p}{\beta V} \int_{\bar{\omega}} \bar{B}_{\bar{\omega}} B_{\bar{\omega}} . \quad (2.22)$$

The indices x and p refer to the exchange and pairing channel, respectively. The second equality is apparent after shifting summation indices and requiring

$$U_x + U_p = U , \quad A_{\bar{\omega}} = \int_{\omega} \bar{d}_{\omega} c_{\bar{\omega}+\omega} , \quad B_{\bar{\omega}} = \int_{\omega} d_{-\omega} c_{\bar{\omega}+\omega} . \quad (2.23)$$

Making use of the formulae (2.20) and (2.21) and including the auxiliary fields in the theory, the additional action is given by

$$S_{\text{HS}} = \int_{\bar{\omega}} \left[U_x^{-1} \bar{\chi}_{\bar{\omega}} \chi_{\bar{\omega}} + \frac{1}{\sqrt{\beta V}} (A_{\bar{\omega}} \bar{\chi}_{\bar{\omega}} + \bar{A}_{\bar{\omega}} \chi_{\bar{\omega}}) \right] + \int_{\bar{\omega}} \left[U_p^{-1} \bar{\psi}_{\bar{\omega}} \psi_{\bar{\omega}} + \frac{i}{\sqrt{\beta V}} (B_{\bar{\omega}} \bar{\psi}_{\bar{\omega}} + \bar{B}_{\bar{\omega}} \psi_{\bar{\omega}}) \right] \quad (2.24)$$

with the identification

$$S_{\text{mat}} + S_{\text{int}} \rightarrow S_{\text{mat}} + S_{\text{HS}} . \quad (2.25)$$

We see that the χ field couples similarly to the fermionic fields as the photon in Eq. (2.11). To make that precise, let us give an expression for the χ self-energy without internal χ propagation, completely analogous to Eq. (2.12):

$$\begin{aligned} \lim_{U_x \rightarrow 0} \Pi_{\bar{\omega}}^{\chi} &= \lim_{G_{0,\bar{\omega}}^{\chi} \rightarrow 0} (G_{0,\bar{\omega}}^{\chi})^{-2} (G_{\bar{\omega}}^{\chi} - G_{0,\bar{\omega}}^{\chi}) = - \lim_{G_{0,\bar{\omega}}^{\chi} \rightarrow 0} (G_{0,\bar{\omega}}^{\chi})^{-2} (\langle \chi_{\bar{\omega}} \bar{\chi}_{\bar{\omega}} \rangle - G_{0,\bar{\omega}}^{\chi}) \\ &= - \lim_{G_{0,\bar{\omega}}^{\chi} \rightarrow 0} (G_{0,\bar{\omega}}^{\chi})^{-2} \int_{\bar{\nu}, \bar{\eta}} \langle \chi_{\bar{\omega}} \bar{\chi}_{\bar{\omega}} \left(\frac{-1}{\sqrt{\beta V}} A_{\bar{\nu}} \bar{\chi}_{\bar{\nu}} \right) \left(\frac{-1}{\sqrt{\beta V}} \bar{A}_{\bar{\eta}} \chi_{\bar{\eta}} \right) \rangle_{0_{\chi}} \\ &= - \frac{1}{\beta V} \langle A_{\bar{\omega}} \bar{A}_{\bar{\omega}} \rangle_{0_{\chi}} = \int'_{\omega, \nu} \langle \bar{d}_{-\omega} d_{-\nu} \bar{c}_{\bar{\omega}+\omega} c_{\bar{\omega}+\nu} \rangle_{0_{\chi}} . \end{aligned} \quad (2.26)$$

Again, we made use of Wick's theorem, but now, the latter averages are to be computed without the interaction terms containing χ . The same calculation for the other channel yields

$$\lim_{U_p \rightarrow 0} \Pi_{\bar{\omega}}^{\psi} = \int'_{\omega, \nu} \langle \bar{d}_{-\omega} d_{-\nu} \bar{c}_{\bar{\omega}+\omega} c_{\bar{\omega}+\nu} \rangle_{0_{\psi}} . \quad (2.27)$$

2.1.4 One-particle-irreducible vertices

In the fRG flow, one usually considers one-particle-irreducible vertices. The definition of these proceeds via connected correlation functions (index c); in the next section, it is more practical to deal with plain correlation functions. The corresponding generating functionals can be defined as¹⁶

$$\mathcal{G}[J] = \frac{\int \mathcal{D}[\Phi] e^{-S[\Phi] + (J, \Phi)}}{\int \mathcal{D}[\Phi] e^{-S[\Phi]}} , \quad \mathcal{G}_c[J] = \ln \frac{\int \mathcal{D}[\Phi] e^{-S[\Phi] + (J, \Phi)}}{\int \mathcal{D}[\Phi] e^{-S_0[\Phi]}} , \quad (J, \Phi) = \int_{\alpha} J_{\alpha} \Phi_{\alpha} , \quad (2.28)$$

such that correlators are given by

$$\langle \Phi_{\alpha_n} \cdots \Phi_{\alpha_1} \rangle = \frac{\delta^n \mathcal{G}[J]}{\delta J_{\alpha_n} \cdots \delta J_{\alpha_1}} \Big|_{J=0} , \quad \langle \Phi_{\alpha_n} \cdots \Phi_{\alpha_1} \rangle_c = \frac{\delta^n \mathcal{G}_c[J]}{\delta J_{\alpha_n} \cdots \delta J_{\alpha_1}} \Big|_{J=0} . \quad (2.29)$$

Define further the expectation value at non-zero sources

$$\bar{\Phi}_{\alpha} := \frac{\delta \mathcal{G}_c[J]}{\delta J_{\alpha}} . \quad (2.30)$$

We will restrict ourselves to cases without spontaneous symmetry breaking and use $J = 0 \Leftrightarrow \bar{\Phi} = 0$. Here, we only need sources with values in an arbitrarily small neighborhood of 0. Using the convexity of the generating functional $\mathcal{G}_c[J]$, we can define a Legendre transform

$$\mathcal{L}[\bar{\Phi}] = (J[\bar{\Phi}], \bar{\Phi}) - \mathcal{G}_c[J[\bar{\Phi}]] , \quad \bar{\Phi}_{\alpha} = \frac{\delta \mathcal{G}_c[J]}{\delta J_{\alpha}} \rightarrow J[\bar{\Phi}] . \quad (2.31)$$

Finally, the generating functional for the one-particle-irreducible vertices $\Gamma^{(n)}$ is given by

$$\Gamma[\bar{\Phi}] = \mathcal{L}[\bar{\Phi}] + \frac{1}{2} (\bar{\Phi}, G_0^{-1} \bar{\Phi}) , \quad \Gamma_{\alpha_1 \dots \alpha_n}^{(n)} = \frac{\delta^n \Gamma}{\delta \bar{\Phi}_{\alpha_n} \cdots \delta \bar{\Phi}_{\alpha_1}} \Big|_{\bar{\Phi}=0} . \quad (2.32)$$

¹⁶Note that using S_0 in the denominator for $\mathcal{G}_c[J]$ does not affect any derivatives and is chosen for convenience.

$\Gamma^{(n)}$ will be called n -point one-particle-irreducible (1PI) vertex, and in reference 18, chapter 6, it is shown that, indeed, the following relations are fulfilled:

$$\begin{aligned}
\Gamma_{\alpha_1\alpha_2}^{(2)} &= \Sigma_{\alpha_1\alpha_2} , \\
\langle \Phi_{\alpha_1} \Phi_{\alpha_2} \Phi_{\alpha_3} \rangle_c &= - \int_{\beta_1} \dots \int_{\beta_3} G_{\alpha_1\beta_1} G_{\alpha_2\beta_2} G_{\alpha_3\beta_3} \Gamma_{\beta_1\beta_2\beta_3}^{(3)} , \\
\langle \Phi_{\alpha_1} \Phi_{\alpha_2} \Phi_{\alpha_3} \Phi_{\alpha_4} \rangle_c &= - \int_{\beta_1} \dots \int_{\beta_4} G_{\alpha_1\beta_1} G_{\alpha_2\beta_2} G_{\alpha_3\beta_3} G_{\alpha_4\beta_4} \Gamma_{\beta_1\beta_2\beta_3\beta_4}^{(4)} , \\
&- \int_{\beta_1} \dots \int_{\beta_6} G_{\alpha_1\beta_1} G_{\alpha_2\beta_2} G_{\alpha_3\beta_3} G_{\alpha_4\beta_4} \Gamma_{\beta_1\beta_2\beta_5}^{(3)} G_{\beta_5\beta_6} \Gamma_{\beta_6\beta_3\beta_4}^{(3)} \\
&- \int_{\beta_1} \dots \int_{\beta_6} G_{\alpha_1\beta_1} G_{\alpha_2\beta_2} G_{\alpha_3\beta_3} G_{\alpha_4\beta_4} \Gamma_{\beta_1\beta_5\beta_4}^{(3)} G_{\beta_5\beta_6} \Gamma_{\beta_6\beta_2\beta_3}^{(3)} \\
&- \zeta(\alpha_1 \leftrightarrow \alpha_2) .
\end{aligned} \tag{2.33}$$

Σ is the self-energy, and in the last line, the next-to-last line (without the minus sign) is repeated with indices α_1 and α_2 exchanged and an additional minus sign if at least one of α_1 and α_2 is a fermionic index.

Let us see how symmetries in the action translate into properties of the 1PI vertices. Given a symmetry, i.e., an isomorphism \mathbf{F} acting on Φ which leaves the action invariant, Γ is left invariant, too (cf. [18], section 6.3):

$$S[\mathbf{F}\Phi] = S[\Phi] \quad \Rightarrow \quad \Gamma[\mathbf{F}\Phi] = \Gamma[\Phi] . \tag{2.34}$$

In particular, translational invariance in space and time of the action leads to vertices which conserve energy and momentum. For the symmetry upon conjugation of the arguments, let us show the relevant cases explicitly. First, note that the behavior of $\Gamma^{(n)}$ under reordering of indices is already set by the definition of $\Gamma^{(n)}$ in Eq. (2.32) via functional derivatives. Depending on the sign of the permutation, a minus sign is required when a fermionic index is involved. The action including light-matter coupling is symmetric under the following operation with corresponding properties for the three-point vertex (suppressing frequency and momentum labels):

$$\begin{aligned}
S_{\text{light-mat}} &= \frac{i}{\sqrt{\beta V}} \int_{\bar{\omega}} (\bar{A}_{\bar{\omega}} \gamma_{\bar{\omega}} - A_{\bar{\omega}} \bar{\gamma}_{\bar{\omega}}) , \\
\mathbf{F}(\bar{c}, c, \bar{d}, d, \bar{\gamma}, \gamma) &= (-c, -\bar{c}, d, \bar{d}, -\gamma, -\bar{\gamma}) \quad \Rightarrow \quad \Gamma_{\bar{c}d\gamma}^{(3)} = -\Gamma_{d\bar{c}\bar{\gamma}}^{(3)} .
\end{aligned} \tag{2.35}$$

In contrast, the coupling to the HS-fields and its symmetry result in

$$\begin{aligned}
S_{\text{HS-coupling}} &= \frac{1}{\sqrt{\beta V}} \int_{\bar{\omega}} (\bar{A}_{\bar{\omega}} \chi_{\bar{\omega}} + A_{\bar{\omega}} \bar{\chi}_{\bar{\omega}}) + \frac{i}{\sqrt{\beta V}} \int_{\bar{\omega}} (\bar{B}_{\bar{\omega}} \psi_{\bar{\omega}} + B_{\bar{\omega}} \bar{\psi}_{\bar{\omega}}) , \\
\mathbf{F}(\bar{c}, c, \bar{d}, d, \bar{\chi}, \chi, \bar{\psi}, \psi) &= (-c, -\bar{c}, d, \bar{d}, \chi, \bar{\chi}, \psi, \bar{\psi}) \\
&\Rightarrow \quad \Gamma_{\bar{c}d\chi}^{(3)} = \Gamma_{d\bar{c}\bar{\chi}}^{(3)} , \quad \Gamma_{\bar{c}d\psi}^{(3)} = \Gamma_{d\bar{c}\bar{\psi}}^{(3)} .
\end{aligned} \tag{2.36}$$

2.1.5 Schwinger-Dyson identities

Studying the behavior of generating functionals under transformation of the integration variable, one can derive identities between correlation functions and, using Eq. (2.33), one-particle-irreducible vertices. For the problem at hand, we want to calculate the particle-hole susceptibility, i.e., the photon self-energy in the limit $|M|^2 \rightarrow 0$, and ignore, e.g., fermionic self-energies (cf. section 1.4). Useful identities, in the form of Schwinger-Dyson equations, are obtained when using the invariance of the generating functional

$\mathcal{G}[J]$ under shifting the integration variable $\Phi \rightarrow \Phi + \Delta$. Clearly, the measure is not affected, and for infinitesimal Δ , one easily derives

$$\left(\zeta_\alpha J_\alpha - \frac{\delta S}{\delta \Phi_\alpha} \left[\frac{\delta}{\delta J} \right] \right) \mathcal{G}[J] = 0 . \quad (2.37)$$

If we choose $\alpha = (\gamma, \bar{\omega})$ and further take a derivative with respect to $J_{\gamma, \bar{\omega}}$, we arrive at

$$\begin{aligned} 0 &= \frac{\delta}{\delta J_{(\gamma, \bar{\omega})}} \left(J_{\gamma, \bar{\omega}} + G_{0, \bar{\omega}}^{\gamma, -1} \frac{\delta}{\delta J_{(\bar{\gamma}, \bar{\omega})}} - \frac{i}{\sqrt{\beta V}} \int_\omega \frac{\delta^2}{\delta J_{(\bar{c}, \omega + \bar{\omega})} \delta J_{(d, \omega)}} \right) \mathcal{G}[J] \\ &= \left(1 + G_{0, \bar{\omega}}^{\gamma, -1} \frac{\delta^2}{\delta J_{(\gamma, \bar{\omega})} \delta J_{(\bar{\gamma}, \bar{\omega})}} - \frac{i}{\sqrt{\beta V}} \int_\omega \frac{\delta^3}{\delta J_{(\bar{c}, \omega + \bar{\omega})} \delta J_{(d, \omega)} \delta J_{(\gamma, \bar{\omega})}} \right) \mathcal{G}[J] . \end{aligned} \quad (2.38)$$

Expectation values of interest for us are obtained for vanishing sources and in the limit $|M|^2 \rightarrow 0$, such that the photonic action does not contribute. Due to symmetry, expectation values of one field alone vanish, and we can directly revert to connected correlators. Using previous relations such as Eq. (2.33) and Eq. (2.35), we find that the self-energy is completely determined by the 1PI three-point vertex:

$$\Pi_\omega^\gamma = G_{0, \bar{\omega}}^{\gamma, -1} - G_\omega^{\gamma, -1} = \int_\omega' G_{\omega + \bar{\omega}}^c G_\omega^d \tilde{\Gamma}_{\omega + \bar{\omega}, \omega, \bar{\omega}}^{\bar{c}d\gamma} , \quad \tilde{\Gamma}^{\bar{c}d\gamma} = \frac{\sqrt{\beta V}}{i} \Gamma^{\bar{c}d\gamma} . \quad (2.39)$$

If, in Eq. (2.39), we derive with respect to sources of c and \bar{d} instead of γ , we get

$$0 = \left(G_{0, \bar{\omega}}^{\gamma, -1} \frac{\delta^3}{\delta J_{(\bar{d}, \bar{\omega})} \delta J_{(c, \omega + \bar{\omega})} \delta J_{(\bar{\gamma}, \bar{\omega})}} + \frac{i}{\sqrt{\beta V}} \int_\omega \frac{\delta^4}{\delta J_{(\bar{d}, \omega)} \delta J_{(d, \nu)} \delta J_{(\bar{c}, \nu + \bar{\omega})} \delta J_{(c, \omega + \bar{\omega})}} \right) \mathcal{G}[J] . \quad (2.40)$$

By expressing $\mathcal{G}[J]$ in terms of $\mathcal{G}_c[J]$, one reverts the four-point correlator coming from the second summand to connected expectation values. Further using $G_{0, \bar{\omega}}^{\gamma, -1} G_\omega^\gamma \rightarrow 1$ in the limit $|M|^2 \rightarrow 0$, we express the three-point vertex and, using Eq. (2.39), the self-energy as

$$\begin{aligned} \tilde{\Gamma}_{\omega + \bar{\omega}, \omega, \bar{\omega}}^{\bar{c}d\gamma} &= G_\omega^{d, -1} G_{\omega + \bar{\omega}}^{c, -1} \int_\nu \langle \bar{d}_\omega d_\nu \bar{c}_{\nu + \bar{\omega}} c_{\omega + \bar{\omega}} \rangle = 1 + \int_\nu G_\nu^d G_{\nu + \bar{\omega}}^c \tilde{\Gamma}_{\omega, \nu, \nu + \bar{\omega}, \omega + \bar{\omega}}^{\bar{d}d\bar{c}c} , \\ \Pi_\omega^\gamma &= \int_\omega G_\omega^d G_{\omega + \bar{\omega}}^c + \int_{\omega, \nu}'' G_\omega^d G_\nu^d G_{\omega + \bar{\omega}}^c G_{\nu + \bar{\omega}}^c \tilde{\Gamma}_{\omega, \nu, \nu + \bar{\omega}, \omega + \bar{\omega}}^{\bar{d}d\bar{c}c} , \quad \tilde{\Gamma}^{\bar{d}d\bar{c}c} = -\beta V \Gamma^{\bar{d}d\bar{c}c} . \end{aligned} \quad (2.41)$$

Eq. (2.39) and (2.41) state identities between the particle-hole susceptibility (in the form of the leading-order photon self-energy), the photonic three-point vertex, and the fermionic four-point vertex, which will prove useful in the analysis in section 3.

2.2 Functional renormalization group

The functional renormalization group (fRG) merges quantum-field-theoretical techniques with the renormalization-group idea. It enables a controlled unfolding of complex macroscopic phenomena from microscopic laws. In a certain procedure, one can let the system flow from a theory of pure microphysical interactions to a coarse-grained picture of an interacting many-body system. This evolution is described exactly in terms of a functional differential equation for the scale-dependent effective action.

Technically, the formalism mainly consists of the study of the effective action upon variation of an artificially introduced parameter Λ from an initial value, say, $\Lambda = \infty$, to a final value, say, $\Lambda = 0$. This flow parameter is usually introduced such that it can be interpreted as an effective infrared cutoff, where modes with energy less than Λ are

suppressed. If initially all modes are suppressed, the system is trivially described by the bare microscopic physical laws, say, a two-body Coulomb interaction in a fermionic system. Decreasing the flow parameter means zooming out, allowing high-energy, i.e., small-length-scale modes to propagate and renormalize the initial, bare interactions. Finally, no mode is suppressed anymore, and one arrives at the original, full theory.

As already seen, we describe physical degrees of freedom by fields in a theory governed by a certain action. The suppression of modes can be achieved by modification of the bare propagator of a field, being the main part of the one-particle, quadratic part of the action. The procedure sketched above sets the propagator of all degrees of freedom to be zero at the initial scale $\Lambda = \infty$. At the end of the flow, $\Lambda = 0$, they have to regain their original value. A useful quantity to study when propagators vary from zero to their original value is the already mentioned effective action, which is nothing but the generating functional for one-particle-irreducible vertices. It describes not only some flowing, low-energy coupling constants but is a functional containing all coupling constants with their full dependencies. It is physically transparent (and can be proven as, e.g., in reference 18, section 7) that without internal propagation, an irreducible vertex is simply the vertex given in the defining action. For the example of a pure two-body Coulomb interaction, only the four-point vertex contributes, with weight set by the interaction parameter. At the end of the flow, with original propagators G_0 , the effective interaction has evolved from the microscopic action S_{int} to the full functional Γ . This is illustrated in Fig. 2.1.

In any concrete procedure, one starts with an initial theory (with a quadratic action described by $G_{0,\Lambda=\infty}$) which is simple enough to be tractable. This is obviously the case for $G_{0,\Lambda=\infty} = 0$, resulting in $\Gamma_{\Lambda=\infty} = S_{\text{int}}$, but certainly other initial conditions are possible. In fact, we will employ a different one as described in the next section. When the initial condition has been specified and the final form of Γ_Λ is looked for, one has to solve the intermediate evolution, described by $\partial_\Lambda \Gamma_\Lambda$. In the appendix, section A.1, we explicitly derive this functional differential equation, often called Wetterich equation [19]. If the evolution could be solved exactly, the exact solution of the problem would be obtained. In particular, this would be independent of the specific dependence of $G_{0,\Lambda}$ on the flow parameter. In a renormalization group sense, different initial theories flow to the same final theory. However, the functional differential equation is in general impossible to solve. Truncations and approximations in the flowing scheme and all internal calculations are needed and influence the quality of the final solution.

An approach which has proven to be useful for problems in condensed-matter physics is the so-called vertex expansion. The generating functional for the 1PI vertices is

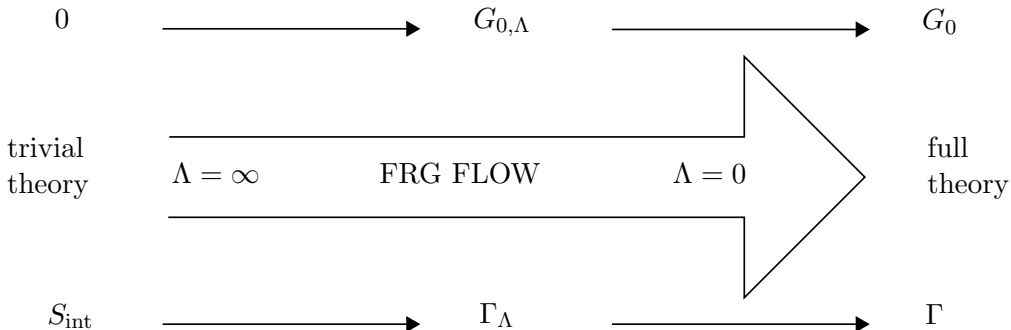


Figure 2.1: FRG flow: The flow parameter Λ , introduced in the quadratic part of the action, makes the theory evolve from a trivial to the original, full one. At the initial scale, the effective action Γ can directly be read off from the interacting part of the action S_{int} . Finally, the desired generating functional for 1PI vertices Γ is obtained.

expanded in terms of powers of its arguments, the 1PI vertices, which are functions of an increasing number of internal quantum numbers. The functional differential equation is transformed to a system of infinitely many coupled differential equations for all the vertices. This hierarchy of differential equations exhibits interesting properties. In particular, the derivative of a vertex $\Gamma^{(n)}$ is determined by other vertices only up to order $n + 2$. Typically, higher-order vertices are zero at the initial scale and, in a weak-coupling expansion, are of increasing orders in the coupling constant. So, it is often a good approximation to truncate the hierarchy by setting vertices starting from some n_0 to their initial value, typically zero. Consequently, the system reduces to a finite number of differential equations and can be solved with standard methods.

2.2.1 Regularizing procedure

As argued in section 1.4, the propagation of conduction-band electrons is not renormalized by the final-state interaction, whereas the valence-band propagator exhibits a power law similar to the particle-hole susceptibility [5]. We are mainly concerned with diagrams for the photon self-energy, which always consists of conduction and valence electrons. Hence, it is sufficient to set only the bare d propagator to be zero initially in order to extinguish all diagrams for this correlator. Thereby, we also reduce the number of terms in the flow equations: We have $\partial_\Lambda G_{0,\alpha\beta} \neq 0$ only if α and β specify a d or \bar{d} field.

In order to achieve the boundary conditions

$$G_{0,\Lambda=\infty}^d = 0, \quad G_{0,\Lambda=0}^d = G_0^d, \quad (2.42)$$

there are endless possibilities for the specific Λ dependence of G_0^d . We will use two particularly useful types of regulators. On the one hand, the simplest curve between two values seems to be a step function, yielding a δ distribution in the derivative. On the other hand, Litim has suggested a functional form, in which the frequency dependence of infrared modes is subtracted from the inverse propagator [20].

$$\begin{aligned} \delta\text{-regulator: } G_{0,\Lambda,\omega,\mathbf{k}}^d &= \Theta(|\omega| - \Lambda) G_{0,\omega,\mathbf{k}}^d = \frac{\Theta(|\omega| - \Lambda)}{i\omega - \xi_k^d}, \\ \partial_\Lambda G_{0,\Lambda,\omega,\mathbf{k}}^d &= -\delta(|\omega| - \Lambda) G_{0,\omega,\mathbf{k}}^d = \frac{-\delta(|\omega| - \Lambda)}{i\omega - \xi_k^d}, \\ \text{Litim regulator: } G_{0,\Lambda,\omega,\mathbf{k}}^d &= \frac{1}{i\omega - \xi_k^d + i\text{sgn}(\omega)(\Lambda - |\omega|)\Theta(\Lambda - |\omega|)}, \\ \partial_\Lambda G_{0,\Lambda,\omega,\mathbf{k}}^d &= \frac{-i\text{sgn}(\omega)\Theta(\Lambda - |\omega|)}{[i\text{sgn}(\omega)\Lambda - \xi_k^d]^2}. \end{aligned} \quad (2.43)$$

As we will see soon, in the flow equations for the 1PI vertices, a typical combination of propagators appear and are summarized under the so-called single-scale propagator,

$$\begin{aligned} S_\Lambda &= -G_\Lambda(\partial_\Lambda G_{0,\Lambda}^{-1})G_\Lambda = (1 + G_{0,\Lambda}\Sigma_\Lambda + G_{0,\Lambda}\Sigma_\Lambda G_{0,\Lambda}\Sigma_\Lambda + \dots) \\ &\quad \times (\partial_\Lambda G_{0,\Lambda})(1 + \Sigma_\Lambda G_{0,\Lambda} + \Sigma_\Lambda G_{0,\Lambda}\Sigma_\Lambda G_{0,\Lambda} + \dots). \end{aligned} \quad (2.44)$$

Diagrammatically, this is sensible as various diagrams are resummed by allowing all combinations of self-energy insertions in a differentiated line [21]. Only if self-energy corrections are omitted, one has the simple relation $S_\Lambda = \partial_\Lambda G_{0,\Lambda}$.

In a Litim-regulated scheme, the single-scale propagator is easily calculated to be

$$\text{Litim regulator: } S_{\Lambda,\omega,\mathbf{k}}^d = \frac{-i\text{sgn}(\omega)\Theta(\Lambda - |\omega|)}{[i\text{sgn}(\omega)\Lambda - \xi_k^d - \Sigma_\Lambda^d(\omega, \mathbf{k})]^2}. \quad (2.45)$$

Using the δ regulator, one simultaneously encounters a δ distribution and discontinuous Θ functions¹⁷. This can be shown to be well-defined by virtue of a Lemma due to Morris, and if the integrand contains no more discontinuities except for the single-scale propagator, one finds [22]

$$\delta \text{ regulator: } S_{\Lambda, \omega, \mathbf{k}}^d = \frac{-\delta(|\omega| - \Lambda)}{i\omega - \xi_k^d - \Sigma_{\Lambda}^d(\omega, \mathbf{k})} . \quad (2.46)$$

2.2.2 Algebraic statement of the flow equations

In the appendix, section A.1, we show a condensed version of the derivation of the functional differential equation for Γ along the lines of reference 18. Here, let us merely state the important steps and results.

As already explained, the flow parameter is used to modify the bare propagator. In a general description, the quadratic part of the action is changed to

$$S_{0, \Lambda}[\Phi] = -\frac{1}{2}(\Phi, G_{0, \Lambda}^{-1} \Phi) . \quad (2.47)$$

Clearly, the generating functional for connected correlation functions with a general argument J is affected:

$$\mathcal{G}_{c, \Lambda}[J] = \ln \frac{\int \mathcal{D}[\Phi] e^{-S_{0, \Lambda}[\Phi] - S_1[\Phi] + (J, \Phi)}}{\int \mathcal{D}[\Phi] e^{-S_{0, \Lambda}}} . \quad (2.48)$$

Furthermore, Γ has as its argument $\bar{\Phi}$, now specified by

$$\bar{\Phi}_{\alpha} = \frac{\delta \mathcal{G}_{c, \Lambda}[J]}{\delta J_{\alpha}} \rightarrow J = J_{\Lambda}[\bar{\Phi}] . \quad (2.49)$$

So, for the generating functional of the 1PI vertices, we have the relation

$$\Gamma_{\Lambda}[\Phi] = (J_{\Lambda}[\bar{\Phi}], \bar{\Phi}) - \mathcal{G}_{c, \Lambda}[J_{\Lambda}[\bar{\Phi}]] + \frac{1}{2}(\bar{\Phi}, G_{0, \Lambda}^{-1} \bar{\Phi}) . \quad (2.50)$$

Differentiating with respect to the flow parameter gives, after a few intermediate steps, the fundamental flow equation for the effective action:

$$\partial_{\Lambda} \Gamma_{\Lambda}[\bar{\Phi}] = -\frac{1}{2} \text{STr} \left\{ \left(\partial_{\Lambda} G_{0, \Lambda}^{-1} \right) \left(\left[\left(\frac{\delta^2 \Gamma_{\Lambda}[\bar{\Phi}]}{\delta \bar{\Phi} \delta \bar{\Phi}} \right)^{\text{T}} - G_{0, \Lambda}^{-1} \right]^{-1} + G_{0, \Lambda} \right) \right\} . \quad (2.51)$$

The supertrace STr runs over multi-indices and additionally contains a minus sign if the first index is fermionic.

As argued before, an expansion in terms of the physically transparent 1PI vertices on both sides of Eq. (2.51) is desirable. In this expansion, permutations of fields play a large role. According to reference 18 (sections 6 and 7), these kind of permutations can be encoded in a symmetrization operator, defined by

$$\mathcal{S}_{\alpha_1 \dots \alpha_{n_1}; \dots; \alpha_{n-n_{\nu}+1} \dots \alpha_n} F_{\alpha_1 \dots \alpha_n} = \frac{1}{(n_1! \dots n_{\nu}!)} \sum_P \text{sgn}_{\zeta}(P) F_{\alpha_{P(1)} \dots \alpha_{P(n)}} . \quad (2.52)$$

Let us mention that, in particular, \mathcal{S} (anti)symmetrizes groups of indices separated by semicolons. If the indices in the groups are already (anti)symmetric, one ends up with

¹⁷Another subtlety is that scale-dependent quantities might be discontinuous at $\Lambda = \infty$ due to the sharp cutoff [22]. In the flow equations we consider, there always appear more than one propagator (resulting in a high-energy decay faster than $1/\omega$) or vertices which vanish at the initial scale, such that this phenomenon does not appear.

$n!/(n_1! \dots n_\nu!)$ summands, a prefactor of unity and a sign corresponding to the exchange of bosonic (+) or fermionic (-) indices. Furthermore, note that in the trace formulation of the flow equations to follow, we use matrix indices (say, β and γ) for the 1PI vertices with the identification $[\Gamma_{\Lambda, \alpha_1 \dots \alpha_{n-2}}^{(n)}]_{\beta\gamma} = \Gamma_{\Lambda, \beta\gamma\alpha_1 \dots \alpha_{n-2}}^{(n)}$.

The flow equation for the two-point vertex, i.e., the self-energy is

$$\partial_\Lambda \Gamma_{\Lambda, \alpha_1 \alpha_2}^{(2)} = -\frac{1}{2} \text{STr} \left\{ S_\Lambda \Gamma_{\Lambda, \alpha_1 \alpha_2}^{(4)} + \mathcal{S}_{\alpha_1; \alpha_2} S_\Lambda \Gamma_{\Lambda, \alpha_2}^{(3)} G_\Lambda \Gamma_{\Lambda, \alpha_1}^{(3)} \right\}. \quad (2.53)$$

Three-point vertices behave as follows, where the two-point vertex is hidden in the self-energy for S_Λ and G_Λ :

$$\begin{aligned} \partial_\Lambda \Gamma_{\Lambda, \alpha_1 \alpha_2 \alpha_3}^{(3)} = & -\frac{1}{2} \text{STr} \left\{ S_\Lambda \Gamma_{\Lambda, \alpha_1 \alpha_2 \alpha_3}^{(5)} + \mathcal{S}_{\alpha_1 \alpha_2; \alpha_3} S_\Lambda \Gamma_{\Lambda, \alpha_2 \alpha_3}^{(4)} G_\Lambda \Gamma_{\Lambda, \alpha_1}^{(3)} \right. \\ & \left. + \mathcal{S}_{\alpha_1; \alpha_2 \alpha_3} S_\Lambda \Gamma_{\Lambda, \alpha_3}^{(3)} G_\Lambda \Gamma_{\Lambda, \alpha_1 \alpha_2}^{(4)} + \mathcal{S}_{\alpha_1; \alpha_2; \alpha_3} S_\Lambda \Gamma_{\Lambda, \alpha_3}^{(3)} G_\Lambda \Gamma_{\Lambda, \alpha_2}^{(3)} G_\Lambda \Gamma_{\Lambda, \alpha_1}^{(3)} \right\}. \end{aligned} \quad (2.54)$$

Neglecting odd vertices, we further note for the four-point vertex

$$\partial_\Lambda \Gamma_{\Lambda, \alpha_1 \alpha_2 \alpha_3 \alpha_4}^{(4)} = -\frac{1}{2} \text{STr} \left\{ S_\Lambda \Gamma_{\Lambda, \alpha_1 \alpha_2 \alpha_3 \alpha_4}^{(6)} + \mathcal{S}_{\alpha_1 \alpha_2; \alpha_3 \alpha_4} S_\Lambda \Gamma_{\Lambda, \alpha_3 \alpha_4}^{(4)} G_\Lambda \Gamma_{\Lambda, \alpha_1 \alpha_2}^{(4)} \right\}. \quad (2.55)$$

In the following, we will explicitly state the flow equations for the various actions derived in the beginning of this chapter. In intermediate steps, we will leave out arguments and detailed indices for notation's sake; external labels will be underlined for clarity. Once again, labels signify both frequencies and momenta, and we will raise the particle index for propagators [in accordance with the definition in Eq. (2.17)] and vertices when all arguments are written and traces dissolved, such that the number superscript becomes redundant. Hence, we write $G_\omega^c = G_{(c, \omega)(\bar{c}, \omega)}$, $S_\omega^d = S_{(d, \omega)(\bar{d}, \omega)}$, $\Gamma_{(c, \omega_1) \dots (\bar{d}, \omega_n)}^{(n)} = \Gamma_{\omega_1, \dots, \omega_n}^{c \dots \bar{d}}$, etc.

In solving flow equations, truncations are essential. Numerically, one can hardly go beyond the treatment of a four-point vertex since the number of arguments drastically increases the computational effort. Therefore, we will leave out several terms in each differential equations. Nevertheless, these approximations will be noted and their significance illuminated in the diagrammatic validation of the flow equations in section 3.2.

2.2.3 Flow equations for the matter system

In the purely fermionic system described by the action in Eq. (2.7), only 1PI vertices with an even number of fields remain. As fermionic self-energies do not contribute to the first-order parquet result (cf. section 1.4), we immediately go over to the flow of the four-point vertex $\Gamma^{\bar{d}\bar{d}\bar{c}c}$, relevant for the particle-hole susceptibility according to Eq. (2.33). Hence, we apply Eq. (2.55) for our scenario, where S_Λ requires d indices for a non-vanishing contribution.

The first summand in Eq. (2.55) contains a six-point vertex. By truncation of the flow, we set it to its initial value, meaning

$$\text{Tr} \left\{ S_{\Lambda, d\bar{d}} \Gamma_{\Lambda, \bar{d}\bar{d}\bar{d}\bar{c}c} \right\} \approx 0 \quad \text{since} \quad \Gamma_{\Lambda_0}^{\bar{d}\bar{d}\bar{d}\bar{c}c} = 0. \quad (2.56)$$

In the second summand of Eq. (2.55), we will find terms with external indices distributed separately in the field indices, e.g., according to $\bar{c}c$ and $\bar{d}d$. By the further determination

of indices via S_Λ , the resulting expression looks as follows. With the graphic representation introduced in section 3, such a term is easily seen to demand forward propagation of a valence-band electron, which is excluded from the choice of states according to section 1.4, whence

$$\text{Tr} \left\{ S_{\Lambda, d\bar{d}} \Gamma_{\Lambda, \bar{d}\bar{d}\bar{c}\bar{c}} G_{\Lambda, d\bar{d}} \Gamma_{\Lambda, \bar{d}\bar{d}\bar{d}\bar{d}} \right\} = 0 . \quad (2.57)$$

Within this level of accuracy, the flow equation of the four-point vertex becomes

$$\begin{aligned} \partial_\Lambda \tilde{\Gamma}_{\Lambda, \omega, \nu, \bar{\omega} + \nu, \bar{\omega} + \omega}^{\bar{d}\bar{d}\bar{c}\bar{c}} &= \frac{\beta V}{2} \text{STr} \left\{ S \Gamma_{(\bar{c}, \bar{\omega} + \nu)(d, \nu)}^{(4)} G \Gamma_{(c, \bar{\omega} + \omega)(\bar{d}, \omega)}^{(4)} + S \Gamma_{(c, \bar{\omega} + \omega)(\bar{d}, \omega)}^{(4)} G \Gamma_{(\bar{c}, \bar{\omega} + \nu)(d, \nu)}^{(4)} \right. \\ &\quad \left. + S \Gamma_{(\bar{c}, \bar{\omega} + \nu)(\bar{d}, \omega)}^{(4)} G \Gamma_{(d, \nu)(c, \bar{\omega} + \omega)}^{(4)} + S \Gamma_{(d, \nu)(c, \bar{\omega} + \omega)}^{(4)} G \Gamma_{(\bar{c}, \bar{\omega} + \nu)(\bar{d}, \omega)}^{(4)} \right\} \\ &= -\frac{\beta V}{2} \text{Tr} \left\{ S_{d\bar{d}} \Gamma_{\bar{d}\bar{c}\bar{c}\bar{d}}^{(4)} G_{c\bar{c}} \Gamma_{\bar{c}\bar{d}\bar{c}\bar{d}}^{(4)} + S_{\bar{d}\bar{d}} \Gamma_{\bar{d}\bar{c}\bar{c}\bar{d}}^{(4)} G_{\bar{c}\bar{c}} \Gamma_{\bar{c}\bar{d}\bar{c}\bar{d}}^{(4)} \right. \\ &\quad \left. + S_{\bar{d}\bar{d}} \Gamma_{\bar{d}\bar{c}\bar{c}\bar{d}}^{(4)} G_{c\bar{c}} \Gamma_{\bar{c}\bar{d}\bar{c}\bar{d}}^{(4)} + S_{d\bar{d}} \Gamma_{\bar{d}\bar{c}\bar{c}\bar{d}}^{(4)} G_{\bar{c}\bar{c}} \Gamma_{\bar{c}\bar{d}\bar{c}\bar{d}}^{(4)} \right\} \\ &= \int_{\omega'}^d S_{\Lambda, \omega'}^d \left(\tilde{\Gamma}_{\Lambda, \omega, \omega', \bar{\omega} + \omega', \bar{\omega} + \omega}^{\bar{d}\bar{d}\bar{c}\bar{c}} G_{\bar{\omega} + \omega'}^c \tilde{\Gamma}_{\Lambda, \omega', \nu, \bar{\omega} + \nu, \bar{\omega} + \omega'}^{\bar{d}\bar{d}\bar{c}\bar{c}} \right. \\ &\quad \left. + \tilde{\Gamma}_{\Lambda, \omega, \omega', \bar{\omega} + \nu, \bar{\omega} + \omega + \nu - \omega'}^{\bar{d}\bar{d}\bar{c}\bar{c}} G_{\bar{\omega} + \omega + \nu - \omega'}^c \tilde{\Gamma}_{\Lambda, \omega', \nu, \bar{\omega} + \omega + \nu - \omega', \bar{\omega} + \omega}^{\bar{d}\bar{d}\bar{c}\bar{c}} \right) . \quad (2.58) \end{aligned}$$

From it, we can directly deduce that the solution to the differential equation will be symmetric in $\omega \leftrightarrow \nu$ at all scales. Given this property at the initial scale, since the propagators only depend on $\bar{\omega}$ and $\omega + \nu$, it applies to the first-order derivative and by iteration to all higher-order derivatives as well.

2.2.4 Flow equations for the light-matter system

A complete description of our problem also contains the photonic degrees of freedom. We have already shown how to extract the photon self-energy in leading order after a transformation and the limiting case of its propagator going to zero. In the interacting part of the action, there additionally appear three-point vertices between a photon and two fermions

$$S_{\text{light-mat}} = \frac{i}{\sqrt{\beta V}} \int_{\bar{\omega}} (\bar{A}_{\bar{\omega}} \gamma_{\bar{\omega}} - A_{\bar{\omega}} \bar{\gamma}_{\bar{\omega}}) , \quad A_{\bar{\omega}} = \int_{\omega} \bar{d}_{\omega} c_{\bar{\omega} + \omega} . \quad (2.59)$$

Contrary to the fermionic four-point vertex $\Gamma^{\bar{d}\bar{d}\bar{c}\bar{c}}$, in S_{int} , a four-point vertex connecting photons and fermions does not occur. Yet, the first summand in Eq. (2.53), where external labels are photonic and S_Λ sets the trace indices to label d fields, requires $\Gamma^{\bar{d}\bar{d}\bar{\gamma}\bar{\gamma}}$. The flow of such a four-point vertex in the presence of vertices with an odd number of fields has not been given in section 2.2.2, the rather long equation is graphically illustrated in reference 18 (Fig. 7.4). As we neither allow intermediate photon propagation nor forward propagation of valence electrons, one can show that the flow of $\Gamma^{\bar{d}\bar{d}\bar{\gamma}\bar{\gamma}}$ is determined by five- and six-point vertices only. Thus, in our level of truncation, we might consider $\Gamma^{\bar{d}\bar{d}\bar{\gamma}\bar{\gamma}}$ constant, meaning

$$\text{Tr} \left\{ S_{\Lambda, d\bar{d}} \Gamma_{\Lambda, \bar{d}\bar{d}\bar{\gamma}\bar{\gamma}} \right\} \approx 0 \quad \text{since} \quad \Gamma_{\Lambda_0}^{\bar{d}\bar{d}\bar{\gamma}\bar{\gamma}} = 0 . \quad (2.60)$$

The resulting flow of the photon self-energy extracted from Eq. (2.53) is of the form

$$\begin{aligned} \partial_\Lambda \Pi_{\Lambda, \bar{\omega}}^\gamma &= \partial_\Lambda \Gamma_{\Lambda, (\gamma, \bar{\omega})(\bar{\gamma}, \bar{\omega})}^{(2)} = -\frac{1}{2} \text{STr} \left\{ S \Gamma_{(\bar{\gamma}, \bar{\omega})}^{(3)} G \Gamma_{(\gamma, \bar{\omega})}^{(3)} + S \Gamma_{(\gamma, \bar{\omega})}^{(3)} G \Gamma_{(\bar{\gamma}, \bar{\omega})}^{(3)} \right\} \\ &= \frac{1}{2} \text{Tr} \left\{ S_{d\bar{d}} \Gamma_{\bar{d}\bar{c}\bar{\gamma}}^{(3)} G_{c\bar{c}} \Gamma_{\bar{c}\bar{d}\bar{\gamma}}^{(3)} + S_{\bar{d}\bar{d}} \Gamma_{\bar{d}\bar{c}\bar{\gamma}}^{(3)} G_{\bar{c}\bar{c}} \Gamma_{\bar{c}\bar{d}\bar{\gamma}}^{(3)} \right\} \\ &= \int_{\omega} S_{\Lambda, \omega}^d \Gamma_{\Lambda, \omega, \bar{\omega} + \omega, \bar{\omega}}^{\bar{d}\bar{c}\bar{\gamma}} G_{\bar{\omega} + \omega}^c \Gamma_{\Lambda, \bar{\omega} + \omega, \omega, \bar{\omega}}^{\bar{c}\bar{d}\bar{\gamma}} = \int_{\omega} S_{\Lambda, \omega}^d G_{\bar{\omega} + \omega}^c \left(\tilde{\Gamma}_{\Lambda, \bar{\omega} + \omega, \omega, \bar{\omega}}^{\bar{c}\bar{d}\bar{\gamma}} \right)^2 . \quad (2.61) \end{aligned}$$

Here, the three-point vertex plays a crucial role. With the prefactors set in Eq. (2.39), one has the initial condition $\tilde{\Gamma}_{\Lambda_0, \bar{\omega}+\omega, \omega, \bar{\omega}}^{\tilde{c}d\gamma} = 1$. In the flow of $\Gamma^{\tilde{c}d\gamma}$ according to Eq. (2.55), we neglect the five-point vertex contribution as a form of truncation,

$$\text{Tr}\left\{S_{\Lambda, dd}\Gamma_{\Lambda, \bar{d}\bar{c}d\gamma}\right\} \approx 0 \quad \text{since} \quad \Gamma_{\Lambda_0, \bar{d}\bar{c}d\gamma} = 0, \quad (2.62)$$

and obtain the flow equation

$$\begin{aligned} \partial_{\Lambda}\tilde{\Gamma}_{\Lambda, \omega_c, \omega_c-\bar{\omega}, \bar{\omega}}^{\tilde{c}d\gamma} &= \frac{\sqrt{\beta V}}{i}\partial_{\Lambda}\Gamma_{\Lambda, (\bar{c}, \omega_c)(d, \omega_c-\bar{\omega})(\bar{\gamma}, \bar{\omega})}^{(3)} \\ &= -\frac{\sqrt{\beta V}}{2i}\text{STr}\left\{S\Gamma_{(\bar{c}, \omega_c)(d, \omega_c-\bar{\omega})}^{(4)}G\Gamma_{(\gamma, \bar{\omega})}^{(3)} + S\Gamma_{(\gamma, \bar{\omega})}^{(3)}G\Gamma_{(\bar{c}, \omega_c)(d, \omega_c-\bar{\omega})}^{(4)}\right\} \\ &= \frac{\sqrt{\beta V}}{2i}\text{Tr}\left\{S_{dd}\Gamma_{\bar{d}\bar{c}\bar{c}d}^{(4)}G_{c\bar{c}}\Gamma_{\bar{c}d\gamma}^{(3)} + S_{\bar{d}d}\Gamma_{\bar{d}\bar{c}\gamma}^{(3)}G_{\bar{c}c}\Gamma_{\bar{c}\bar{d}\bar{d}}^{(4)}\right\} \\ &= \int'_{\omega} S_{\Lambda, \omega}^d \tilde{\Gamma}_{\Lambda, \bar{\omega}+\omega, \omega, \bar{\omega}}^{\tilde{c}d\gamma} G_{\bar{\omega}+\omega}^c \tilde{\Gamma}_{\Lambda, \omega, \omega_c-\bar{\omega}, \omega_c, \bar{\omega}+\omega}^{\bar{d}\bar{c}c}. \end{aligned} \quad (2.63)$$

Note that in general, three-point vertices, as the one above, would modify the flow of the four-point vertex $\Gamma^{\bar{d}\bar{d}c\bar{c}}$. Nevertheless, we can omit these contributions as they come with intermediate photon lines, and these vanish in the limit $|M|^2 \rightarrow 0$, appropriate for getting the leading part of the photon self-energy.

2.2.5 Flow equations for the HS-transformed matter system

The explicit flow equations for the transformed matter system are deduced analogously to the previous ones starting from Eq. (2.53) and Eq. (2.54). The truncation arguments are different, though, as there is no restriction on internal bosonic propagation. Here, we argue that the HS transformation transfers the role of the fermionic four-point vertex in the original action to the bosonic three-point vertices $\Gamma^{\tilde{c}d\chi}$, $\Gamma^{\tilde{c}d\psi}$. Having one argument less compared to $\Gamma^{(4)}$, they are favorable in terms of computational effort. Although n -point vertices with $n \geq 4$, which do no longer appear in the action, are generated by the flow, we neglect these contributions and explore the resummation intrinsic in bosonic self-energies and three-point vertices.

Without the term first summand in Eq. (2.53), coupling external bosonic lines to two valence electrons, the flow of the χ and ψ self-energies is given by

$$\begin{aligned} \partial_{\Lambda}\Pi_{\Lambda, \bar{\omega}}^{\chi} &= \partial_{\Lambda}\Gamma_{\Lambda, (\bar{\chi}, \bar{\omega})(\bar{\chi}, \bar{\omega})}^{(2)} = -\frac{1}{2}\text{STr}\left\{S\Gamma_{(\bar{\chi}, \bar{\omega})}^{(3)}G\Gamma_{(\chi, \bar{\omega})}^{(3)} + S\Gamma_{(\chi, \bar{\omega})}^{(3)}G\Gamma_{(\bar{\chi}, \bar{\omega})}^{(3)}\right\} \\ &= \frac{1}{2}\text{Tr}\left\{S_{dd}\Gamma_{\bar{d}c\bar{\chi}}^{(3)}G_{c\bar{c}}\Gamma_{\bar{c}d\chi}^{(3)} + S_{\bar{d}d}\Gamma_{\bar{d}c\chi}^{(3)}G_{\bar{c}c}\Gamma_{\bar{c}\bar{d}\bar{\chi}}^{(3)}\right\} \\ &= \int'_{\omega} S_{\Lambda, \omega}^d \Gamma_{\Lambda, \omega, \bar{\omega}+\omega, \bar{\omega}}^{\bar{d}c\bar{\chi}} G_{\bar{\omega}+\omega}^c \Gamma_{\Lambda, \bar{\omega}+\omega, \omega, \bar{\omega}}^{\tilde{c}d\chi} = \int'_{\omega} S_{\Lambda, \omega}^d G_{\bar{\omega}+\omega}^c (\tilde{\Gamma}_{\Lambda, \bar{\omega}+\omega, \omega, \bar{\omega}}^{\tilde{c}d\chi})^2, \end{aligned} \quad (2.64)$$

$$\begin{aligned} \partial_{\Lambda}\Pi_{\Lambda, \bar{\omega}}^{\psi} &= \partial_{\Lambda}\Gamma_{\Lambda, (\bar{\psi}, \bar{\omega})(\bar{\psi}, \bar{\omega})}^{(2)} = -\frac{1}{2}\text{STr}\left\{S\Gamma_{(\bar{\psi}, \bar{\omega})}^{(3)}G\Gamma_{(\psi, \bar{\omega})}^{(3)} + S\Gamma_{(\psi, \bar{\omega})}^{(3)}G\Gamma_{(\bar{\psi}, \bar{\omega})}^{(3)}\right\} \\ &= \frac{1}{2}\text{Tr}\left\{S_{dd}\Gamma_{\bar{d}c\bar{\psi}}^{(3)}G_{c\bar{c}}\Gamma_{\bar{c}d\psi}^{(3)} + S_{\bar{d}d}\Gamma_{\bar{d}c\psi}^{(3)}G_{\bar{c}c}\Gamma_{\bar{c}\bar{d}\bar{\psi}}^{(3)}\right\} \\ &= -\int'_{\omega} S_{\Lambda, \omega}^d \Gamma_{\Lambda, \omega, \bar{\omega}-\omega, \bar{\omega}}^{\bar{d}c\bar{\psi}} G_{\bar{\omega}-\omega}^c \Gamma_{\Lambda, \bar{\omega}-\omega, \omega, \bar{\omega}}^{\tilde{c}d\psi} = \int'_{\omega} S_{\Lambda, \omega}^d G_{\bar{\omega}-\omega}^c (\tilde{\Gamma}_{\Lambda, \bar{\omega}-\omega, \omega, \bar{\omega}}^{\tilde{c}d\psi})^2. \end{aligned} \quad (2.65)$$

Referring to S_{HS} in Eq. (2.24), $\tilde{\Gamma}^{\tilde{c}d\chi} = \sqrt{\beta V}\Gamma^{\tilde{c}d\chi}$ and $\tilde{\Gamma}^{\tilde{c}d\psi} = \sqrt{\beta V}\Gamma^{\tilde{c}d\psi}/i$ have the initial conditions $\tilde{\Gamma}_{\Lambda_0, \bar{\omega}+\omega, \omega, \bar{\omega}}^{\tilde{c}d\chi} = 1$ and $\tilde{\Gamma}_{\Lambda_0, \bar{\omega}-\omega, \omega, \bar{\omega}}^{\tilde{c}d\psi} = 1$.

The flow of the three-point vertices, without a five-point or the fermionic four-point vertex, is determined by the coupling of different three-point vertices. In the exchange

channel, we get the flow equation

$$\begin{aligned}
\partial_\Lambda \tilde{\Gamma}_{\Lambda, \omega_c, \omega_c - \bar{\omega}, \bar{\omega}}^{\tilde{c}d\chi} &= \sqrt{\beta V} \partial_\Lambda \Gamma_{\Lambda, (\bar{c}, \omega_c)(d, \omega_c - \bar{\omega})(\bar{\chi}, \bar{\omega})}^{(3)} \\
&= -\frac{\sqrt{\beta V}}{2} \text{STr} \left\{ S \Gamma_{(\chi, \bar{\omega})}^{(3)} G \Gamma_{(d, \omega_c - \bar{\omega})}^{(3)} G \Gamma_{(\bar{c}, \omega_c)}^{(3)} + S \Gamma_{(\bar{c}, \omega_c)}^{(3)} G \Gamma_{(d, \omega_c - \bar{\omega})}^{(3)} G \Gamma_{(\chi, \bar{\omega})}^{(3)} \right\} \\
&= \frac{\sqrt{\beta V}}{2} \text{Tr} \left\{ S_{dd} \Gamma_{d\bar{c}\chi}^{(3)} G_{\bar{c}\bar{c}} \Gamma_{c\bar{\psi}d}^{(3)} G_{\bar{\psi}\bar{\psi}} \Gamma_{\psi d\bar{c}}^{(3)} + S_{dd} \Gamma_{d\bar{\psi}\bar{c}}^{(3)} G_{\bar{\psi}\bar{\psi}} \Gamma_{\bar{\psi}cd}^{(3)} G_{c\bar{c}} \Gamma_{\bar{c}d\chi}^{(3)} \right\} \\
&= \int_\omega S_{\Lambda, \omega}^d \tilde{\Gamma}_{\Lambda, \bar{\omega} + \omega, \omega, \bar{\omega}}^{\tilde{c}d\chi} G_{\bar{\omega} + \omega}^c \tilde{\Gamma}_{\Lambda, \bar{\omega} + \omega, \omega_c - \bar{\omega}, \omega_c + \omega}^{\tilde{c}d\psi} G_{\Lambda, \omega_c + \omega}^\psi \tilde{\Gamma}_{\Lambda, \omega_c, \omega, \omega_c + \omega}^{\tilde{c}d\psi} \quad (2.66)
\end{aligned}$$

and similarly for the pairing channel

$$\begin{aligned}
\partial_\Lambda \tilde{\Gamma}_{\Lambda}^{\tilde{c}d\bar{\psi}}(\omega_c, \bar{\omega} - \omega_c, \bar{\omega}) &= \frac{\sqrt{\beta V}}{i} \partial_\Lambda \Gamma_{\Lambda, (\bar{c}, \omega_c)(d, \bar{\omega} - \omega_c)(\bar{\psi}, \bar{\omega})}^{(3)} \\
&= -\frac{\sqrt{\beta V}}{2i} \text{STr} \left\{ S \Gamma_{(\psi, \bar{\omega})}^{(3)} G \Gamma_{(d, \bar{\omega} - \omega_c)}^{(3)} G \Gamma_{(\bar{c}, \omega_c)}^{(3)} + S \Gamma_{(\bar{c}, \omega_c)}^{(3)} G \Gamma_{(d, \bar{\omega} - \omega_c)}^{(3)} G \Gamma_{(\psi, \bar{\omega})}^{(3)} \right\} \\
&= \frac{\sqrt{\beta V}}{2i} \text{Tr} \left\{ S_{dd} \Gamma_{d\bar{c}\psi}^{(3)} G_{\bar{c}\bar{c}} \Gamma_{c\bar{\chi}d}^{(3)} G_{\bar{\chi}\bar{\chi}} \Gamma_{\chi d\bar{c}}^{(3)} + S_{dd} \Gamma_{d\bar{\chi}\bar{c}}^{(3)} G_{\bar{\chi}\bar{\chi}} \Gamma_{\bar{\chi}cd}^{(3)} G_{c\bar{c}} \Gamma_{\bar{c}d\psi}^{(3)} \right\} \\
&= \int_\omega S_{\Lambda, \omega}^d \tilde{\Gamma}_{\Lambda, \bar{\omega} - \omega, \omega, \bar{\omega}}^{\tilde{c}d\bar{\psi}} G_{\bar{\omega} - \omega}^c \tilde{\Gamma}_{\Lambda, \bar{\omega} - \omega, \bar{\omega} - \omega_c, \omega_c - \omega}^{\tilde{c}d\chi} G_{\Lambda, \omega_c - \omega}^\chi \tilde{\Gamma}_{\Lambda, \omega_c, \omega, \omega_c - \omega}^{\tilde{c}d\chi} . \quad (2.67)
\end{aligned}$$

2.3 Computational considerations

The flow equations in the different forms stated throughout section 2.2 can be solved numerically. Generally speaking, after discretization of continuous variables, one has a first-order ordinary differential equation for a large vector containing the different 1PI vertices at any of their argument configurations. The numerical difficulty lies in the size of this vector.

We are mainly concerned with an infinite valence-band mass. In this case, all relevant quantities are effectively only frequency-dependent. This can be shown by a transformation in the functional integral, as done in reference 2. Here, let us confine ourselves to a diagrammatic argument. The bare vertices are momentum-independent. Any renormalization via connected diagrams contains propagating lines of the valence-band electron, which absorbs any momentum dependence without being affected. Merely the conduction-band propagator has to be integrated over its momentum dependence, yielding a local c propagator.

Even without momentum dependencies in the 1PI vertices, in principle, infinitely many Matsubara frequencies contribute. However, there are two limitations to this.

Sharp cutoff in G^c : In the flow equations, there always appears at least one conduction-band propagator. Its local, purely frequency-dependent form is obtained after integration (note that, being a fermionic Matsubara frequency, $\omega \neq 0$):

$$\begin{aligned}
G_\omega^c &= \int_{\mathbf{k}} \frac{1}{i\omega - \xi_{\mathbf{k}}^c} = \rho \int_0^{\mu + \xi_0} d\epsilon \frac{1}{i\omega - \epsilon + \mu} = \rho \int_{-\xi_0}^{\xi_0} d\xi \frac{1}{i\omega - \xi} = -2i\rho \arctan\left(\frac{\xi_0}{\omega}\right) \\
&= -i\pi\rho \text{sgn}(\omega) \left[1 - \frac{2}{\pi} \arctan\left(\frac{|\omega|}{\xi_0}\right) \right] \approx -i\pi\rho \text{sgn}(\omega) \Theta(\xi_0 - |\omega|) . \quad (2.68)
\end{aligned}$$

With the last approximation, we ignore any details of the cutoff, which are of no physical relevance. Note that, in the third step, we made use of a half-filled band, $\mu = \xi_0$ (cf. section 1.4), which renders the propagator purely imaginary.

Due to the sharp cutoff, in each integration in the flow equations, only a finite number of summands appear. Still, the c propagator and not the vertices themselves have a sharp cutoff. The highest frequency value appearing on the right-hand side of a flow equation always exceeds the one on the left-hand side. To deal with this, we give a second argument.

Analyticity of Green's functions: The Matsubara formalism is well suited for calculations with a relatively small number of data points. Retarded Green's functions are analytic in the upper-half complex plane; all poles lie on or below the real axis. Therefore, the structure encoded in such functions in terms of Matsubara frequencies decreases with the distance of the frequency to the poles on the real axis, i.e., with its modulus. Furthermore, the problem at hand is known to be infrared-divergent. The physically interesting part of the corresponding functions happens at $i\bar{\omega} + \xi^d \rightarrow \omega - \omega_0 \ll \xi_0$. At large enough frequencies, we can thus approximate a 1PI vertex to be constant.

The size of the vector, comprising all vertices and subject to the differential equation, is dominated by the number of frequency configurations of its constituent with the largest number of arguments. By energy conservation, an n -point 1PI vertex $\Gamma^{(n)}$ has $n - 1$ independent arguments. If we have $2N$ data points for each Matsubara frequency, including $\Gamma^{(n)}$ in our solution requires (in principle) storing $(2N)^{n-1}$ complex values. Reasonably demanding a number of positive Matsubara frequencies on the order of 100 (in fact, we mostly take $N = 200$ in our calculations), one clearly sees a limit at the four-point vertex:

$$\Gamma^{(4)}, \quad N = 200 : \\ 400^3 \text{ data points} \sim 6 \cdot 10^7 \text{ complex values} \sim 10^9 \text{ Bytes} . \quad (2.69)$$

All higher-order 1PI vertices are impossible to treat exactly¹⁸. Including the symmetry of a Green's function upon inversion of all Matsubara frequencies and the symmetry of $\Gamma^{(4)}$ in its first two arguments (cf. section 2.2), we ultimately have to store $N^2 \cdot (2N + 1)$ data points for $\Gamma^{(4)}$.

Finally, let us justify the choice of parameters for our numerical calculations. In section 1.4, we have pointed out the special diagrammatic situation of the Fermi-edge problem. In particular, we argued that neither valence-band particle-hole bubbles nor closed loops occur. It follows, that there always is exactly one valence-band hole in diagrams for the particle-hole susceptibility. The bosonic frequency $\bar{\omega}$ can be chosen to be always carried by the valence band. Hence, it is always accompanied by the band gap encoded in ξ^d , which, after the above mentioned manual adjustments, has the single effect of shifting arguments in the logarithm away from the branch cut (cf. section A.2). Since we want to notably observe the infrared singularities close to the threshold ω_0 also in Matsubara frequency space, we choose ξ^d to be small but finite. Moreover, the parquet result (1.8) is usually obtained in a zero-temperature formalism. In order to reproduce this behavior with sufficient resolution in imaginary-frequency space, we choose temperature small enough compared to $\xi_0 = \mu$. In practice, we take the following values

$$\beta\xi_0 = 500 , \quad \xi^d/\xi_0 = -1/25 , \quad u = \rho U = 0.28 . \quad (2.70)$$

The value for the coupling parameter u comes from the following consideration: It should be large enough to see the influence of high powers of $u \ln |\xi_0/(i\bar{\omega} + \xi^d)|$; nevertheless, neglecting higher-order vertices is a perturbative strategy, and we need small enough u to justify this. The strictest limitation comes from the dynamic χ propagator, since the

¹⁸In the finite-mass case, already a three-point vertex has five arguments (two frequencies, two moduli of momenta, and a relative angle) and is out of reach for an exact treatment.

χ self-energy, similarly to the photon self-energy, diverges at small frequencies. In the function $G_{\bar{\omega}}^{\chi} = -U_x/(1 + U_x\Pi_{\bar{\omega}}^{\chi})$, $\Pi_{\bar{\omega}}^{\chi}$ acquires large negative values. Thus, the condition for stability is $|U_x\Pi^{\chi}| < 1$. For $U_x = U/2$, this turns out to be fulfilled only for $u < 0.3$. The corresponding perturbative parameter at $u = 0.28$,

$$u \ln \left(\frac{\xi_0}{|i\bar{\omega} + \xi^d|} \right) \leq u \ln \left(\frac{\xi_0}{|\xi^d|} \right) \approx 0.9 , \quad (2.71)$$

is perfectly suited for our needs.

The differential equation will ultimately be solved with a Runge-Kutta-4 algorithm. Settled by convergence studies, we choose the initial value to be $\rho V \Lambda_0 = 10^4 \Lambda_0/xi_0 = 2 \times 10^3$ and evolve in a few hundred iteration steps on a logarithmic grid. In a δ -regulated scheme, all functions are considered piecewise constant, and the δ distribution acquires finite weight $\beta/(2\pi)$. The Litim regulator is perfectly applicable to finite-temperature calculations but requires significantly higher computational effort as a whole sum over frequencies has to be performed.

3 Analysis

Having collected a variety of computational tools (section 2) and theoretical background (section 1.4), we begin our analysis of the Fermi-edge singularity. Any of our results for the particle-hole susceptibility will be tested against the famous parquet formulae (1.8) and (1.10), originating from an exact summation of all leading log. diagrams. We aim not only to resolve the infrared singularity, but to find exact agreement with the power-law divergence of the first-order parquet result.

Foremost, it is important to bear in mind that we can tackle this problem following *two different approaches*. On the one hand, we can consider the particle-hole susceptibility as a correlation function of four fermionic operators and express it via 1PI vertices. In the matter system, we only need the appropriate fermionic four-point vertex; in the HS-transformed matter system, also three-point vertices connecting auxiliary fields to fermions are of importance. These vertices can be computed via the flow equations, and only at the very end of the flow, the correlator is constructed. On the other hand, noting that the four-point correlation function is integrated over two external (fermionic) variables, we can view the particle-hole susceptibility as the leading contribution to a bosonic (photon) self-energy¹⁹. In this light-matter system, the correlator, expressed as the self-energy, is directly included in a system of coupled flow equations. Hubbard-Stratonovich fields are not used anymore because the additional irreducibility in the exchange channel hinders the equivalence between the photon self-energy and the particle-hole susceptibility.

Either way, we have *different means* to apply the fRG flow equations. First, for infinite hole mass, the flow equations can be solved numerically and their solution presented as curves for the particle-hole susceptibility in terms of Matsubara frequencies. Knowing the parquet result analytically, we can simply transform it to imaginary frequencies and compare it to the numerical data. Secondly, a diagrammatic validation of the fRG flow sheds light on the underlying structure of the system of differential equations. Examining the involved parquet graphs, one can explain why certain curves match the prediction better than others. In a third approach, we are able to extract analytic solutions from the flow equations in the light-matter system. Truncating the flow at the level of a constant four-point vertex, we find, without further approximations, that we exactly reproduce the parquet result (1.8). In the finite-mass situation, a few hand-waving arguments allow us to get close to the functional dependence from Eq. (1.10).

We will combine all these insights to address the question of how the fRG results can—or cannot—be generalized to other problems or even used to gain solutions beyond first-order parquet. Beforehand, let us, however, calculate the lowest-order parquet graphs by standard perturbation theory to introduce the diagrammatic language used throughout our analysis and get familiar with the parquet formula in imaginary-frequency space.

¹⁹This seems very natural, given our introduction in terms of polariton physics, but can also be seen as a computational trick.

3.1 Perturbative calculation

The lowest-order parquet graphs are obtained by expanding the four-point correlator in the interaction parameter U . Given the restriction to leading log. diagrams (by applying the simplifications of section 1.4), a certain order in the coupling $u = \rho U$ is equivalent to this order in the parameter $u \ln \xi_0 / \tilde{w}$ (\tilde{w} measured from the threshold). For the scope of this work, full lines denote conduction (c) and dashed lines valence-band (d) propagators. A bare vertex, symbolized by a solid circle, demands energy-momentum conservation and multiplication by $-U$. Summations over internal variables include the appropriate prefactor corresponding to dimension-full integrals. Apart from that, there are no combinatorial or sign factors attached to diagrams. In diagrams for the particle-hole susceptibility,

$$\Pi(\bar{\omega}) = \int'_{\omega, \nu} \langle \bar{d}_\omega d_\nu \bar{c}_{\bar{\omega}+\nu} c_{\bar{\omega}+\omega} \rangle, \quad (3.1)$$

conduction- and valence-band-electron energy-momentum will differ by $\bar{\omega}$ at the boundary points. As we ignore self-energies, we will denote bare propagators without the index 0. Modifications to that in the finite-mass case will be treated separately in section 3.3.2.

The lowest-order diagrams of the particle-hole susceptibility are shown in Fig. 3.1. While the first three diagrams belong to the class of ladder diagrams, the last diagram, which by contrast contains a conduction-band hole, is the crossed diagram already mentioned in section 1.4. The zeroth-order contribution is simply a non-interacting particle-hole bubble:

$$U^0 : \int'_{\omega, \nu} \langle \bar{d}_\omega d_\nu \bar{c}_{\bar{\omega}+\nu} c_{\bar{\omega}+\omega} \rangle_0 = \int'_\omega G_\omega^d G_{\bar{\omega}+\omega}^c. \quad (3.2)$$

In higher-orders, only connected (index c) expectation values remain, since loops and retarded valence-band propagators are excluded (cf. section 1.4). The first-order diagram shows how multiple bubbles factorize in the integral:

$$\begin{aligned} -U^1 : & \int''_{\omega, \nu, \bar{\omega}_1, \omega_1, \nu_1} \langle \bar{d}_\omega d_\nu \bar{d}_{\nu_1 - \bar{\omega}_1} d_{\nu_1} \bar{c}_{\bar{\omega}+\nu} c_{\bar{\omega}+\omega} \bar{c}_{\bar{\omega}_1 + \omega_1} c_{\omega_1} \rangle_{0,c} \\ & = \int''_{\omega, \nu} G_\omega^d G_\nu^d G_{\bar{\omega}+\omega}^c G_{\bar{\omega}+\nu}^c. \end{aligned} \quad (3.3)$$

The crossed diagram in second order does not factorize. Wick's theorem gives

$$\begin{aligned} U^2 : & \frac{1}{2} \int'''_{\omega, \nu, \bar{\omega}_1, \omega_1, \nu_1, \bar{\omega}_2, \omega_2, \nu_2} \langle \bar{d}_\omega d_\nu \bar{d}_{\nu_1 - \bar{\omega}_1} d_{\nu_1} \bar{d}_{\nu_2 - \bar{\omega}_2} d_{\nu_2} \bar{c}_{\bar{\omega}+\nu} c_{\bar{\omega}+\omega} \bar{c}_{\bar{\omega}_1 + \omega_1} c_{\omega_1} \bar{c}_{\bar{\omega}_2 + \omega_2} c_{\omega_2} \rangle_{0,c} \\ & = \int'''_{\omega, \nu, \eta, \omega_1, \nu_1, \omega_2} G_\omega^d G_\nu^d G_\eta^d \langle \bar{c}_{\bar{\omega}+\nu} c_{\bar{\omega}+\omega} \bar{c}_{\eta-\nu+\omega_1} c_{\omega_1} \bar{c}_{\omega-\eta+\omega_2} c_{\omega_2} \rangle_{0,c} \\ & = \int'''_{\omega, \nu, \eta} G_\omega^d G_\nu^d G_\eta^d [G_{\bar{\omega}+\omega}^c G_{\bar{\omega}+\nu}^c G_{\bar{\omega}+\eta}^c + G_{\bar{\omega}+\omega}^c G_{\bar{\omega}+\omega+\nu-\eta}^c G_{\bar{\omega}+\nu}^c]. \end{aligned} \quad (3.4)$$

We calculate the integrals within logarithmic accuracy, for infinite hole mass and frequencies close to the threshold in the appendix, section A.2. Due to factorization, the

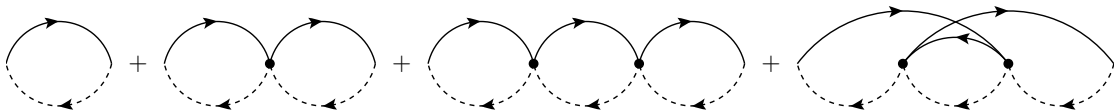


Figure 3.1: Four-point correlator $\langle \bar{d} \bar{d} \bar{c} c \rangle$ up to second order, consisting of the first three ladder diagrams [(0L), (1L), (2L)] and the crossed diagram [(2C)]. Full (dashed) lines denote conduction- (valence-) electron propagators. Dots represent bare vertices with a factor $-U$.

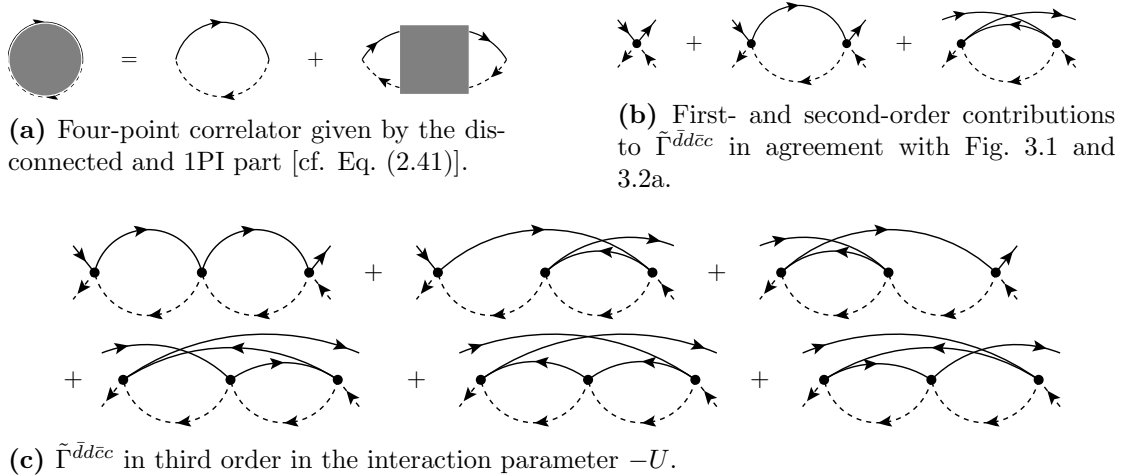


Figure 3.2: Diagrammatic relations for the four-point 1PI vertex $\Gamma^{\tilde{d}d\bar{c}c}$ determining the four-point correlator in the matter system. External lines represent amputated legs.

ladder diagrams $\Pi^{(n,L)}$ can be computed at any order, and, consistent with Mahan [15], the crossed diagram $\Pi^{(2C)}$ has reduced weight compared to $\Pi^{(2L)}$ with opposite sign:

$$\Pi^{(n,L)}(\bar{\omega}) = (-U)^n \left[\rho \ln \left(\frac{-i\bar{\omega} - \xi^d}{\xi_0} \right) \right]^{n+1}, \quad \Pi^{(2C)}(\bar{\omega}) = -\frac{1}{3} \Pi^{(2L)}(\bar{\omega}). \quad (3.5)$$

For higher-order contributions to the four-point correlator, let us merely show the diagrams. In fact, as “the absence of closed dotted loops severely limits possible graphs” [3], one only has to connect the interaction vertices between a series of d lines in all possible ways with conduction-band lines. In Fig. 3.2b and Fig. 3.2c, we show the diagrams up to third order for the one-particle-irreducible four-point vertex. As already seen in Eq. (2.41), the four-point correlator is given by the non-interacting and the connected contribution. According to Eq. (2.33), in the absence of vertices with an odd number of fields, the connected four-point correlator can be expressed by the 1PI four-point vertex only; external legs attached appropriately. Fig. 3.2a shows this relation with the four-point correlator on the left-hand side and the four-point vertex $\tilde{\Gamma}^{\tilde{d}d\bar{c}c}$ denoted by a full square.

The summation of all leading log. diagrams produces the power law in the infinite-mass parquet result (1.8). Its representation in terms of Matsubara frequencies and, particularly, the real part, which will be compared to numerical data in the following sections, read

$$\begin{aligned} \Pi_{\bar{\omega}}^{\gamma} &= \frac{1}{2U} \left[1 - \left(\frac{-i\bar{\omega} - \xi^d}{\xi_0} \right)^{-2u} \right] = \frac{\rho}{2u} \left[1 - e^{-2u \ln \left(\frac{-i\bar{\omega} - \xi^d}{\xi_0} \right)} \right], \\ \text{Re } \Pi_{\bar{\omega}}^{\gamma} &= \frac{\rho}{2u} \left[1 - e^{-2u \ln \left(\frac{|i\bar{\omega} - \xi^d|}{\xi_0} \right)} \cos \left(2u \arg(i\bar{\omega} + \xi^d) \right) \right] \\ &= \frac{\rho}{2u} \left[1 - \left(\frac{\bar{\omega}^2 + (\xi^d)^2}{\xi_0^2} \right)^{-u} \cos \left(2u \arctan \left(\frac{\bar{\omega}}{\xi^d} \right) \right) \right]. \end{aligned} \quad (3.6)$$

Note that, in the chosen frequency regime $|i\bar{\omega} + \xi^d| \rightarrow |\omega - \omega_0| \ll \xi_0$, every summand in a power series in u is negative and that the functions remain finite even at zero Matsubara frequency. It is easy to check that, indeed, the first two orders in u equal the sum of the diagrams shown in Fig. 3.1. In Fig. 3.3, one can see how the orders build up to the power law; in the logarithmic inset, here and henceforth, the constant $1/(2u)$ is subtracted for all functions before the negative part is plotted.

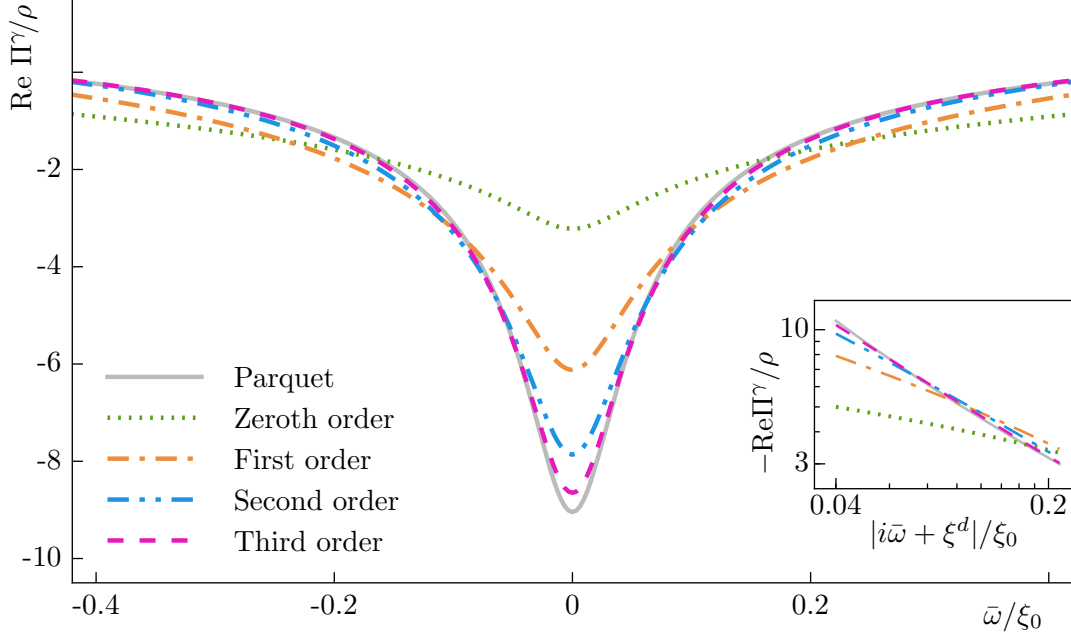


Figure 3.3: Parquet formula in terms of Matsubara frequencies [Eq. (3.6)] at increasing orders in the coupling u . In the logarithmic plot of the negative parts, the constant $1/(2u)$ is subtracted for all functions.

3.2 Numerical data and diagrammatic validation

We commence the fRG analysis by studying the four-point correlator obtained from the flow of 1PI vertices. After examining the diagrammatic structure of the flow in the pure matter system, we consider the resummation effects of dynamic HS fields. In section 3.2.3, we include the photon and allow its self-energy to flow in the light-matter system. The leading contribution, the particle-hole susceptibility, is produced, since the flow equations in section 2.2.4 do not allow intermediate photon propagation, corresponding to the limit $|M|^2 \rightarrow 0$ [cf. Eq. (2.12)].

3.2.1 Four-point correlator in the matter system

The mathematical relation between the four-point correlator and the four-point 1PI vertex from Fig. 3.2a [cf. Eq. (2.41)] reads

$$\begin{aligned} \langle \bar{d}_\omega d_\nu \bar{c}_{\bar{\omega}+\omega} c_{\bar{\omega}+\nu} \rangle_c &= -G_\omega^d G_\nu^d G_{\bar{\omega}+\omega}^c G_{\bar{\omega}+\nu}^c \Gamma_{\omega,\nu,\bar{\omega}+\omega,\bar{\omega}+\nu}^{\bar{d}d\bar{c}c}, \\ \Pi^\gamma(\bar{\omega}) &= \int'_\omega G_\omega^d G_{\bar{\omega}+\omega}^c + \int''_{\omega,\nu} G_\omega^d G_\nu^d G_{\bar{\omega}+\omega}^c G_{\bar{\omega}+\nu}^c \tilde{\Gamma}_{\omega,\nu,\bar{\omega}+\omega,\bar{\omega}+\nu}^{\bar{d}d\bar{c}c}. \end{aligned} \quad (3.7)$$

Inserting the numerical solution for $\tilde{\Gamma}^{\bar{d}d\bar{c}c}$ from the flow of Eq. (2.58) results in the correlator shown in Fig. 3.5.

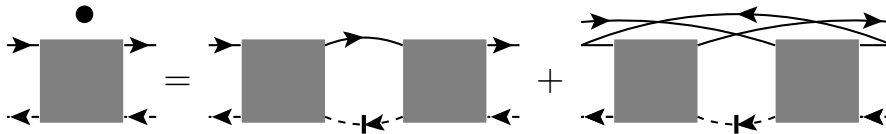


Figure 3.4: Diagrammatic representation of the flow equation (2.58) for the four-point 1PI vertex $\tilde{\Gamma}^{\bar{d}d\bar{c}c}$. A dot denotes a fully differentiated diagram; lines with a vertical dash symbolize the single-scale propagator. The contribution of the six-point vertex is neglected [Eq. (2.56)].

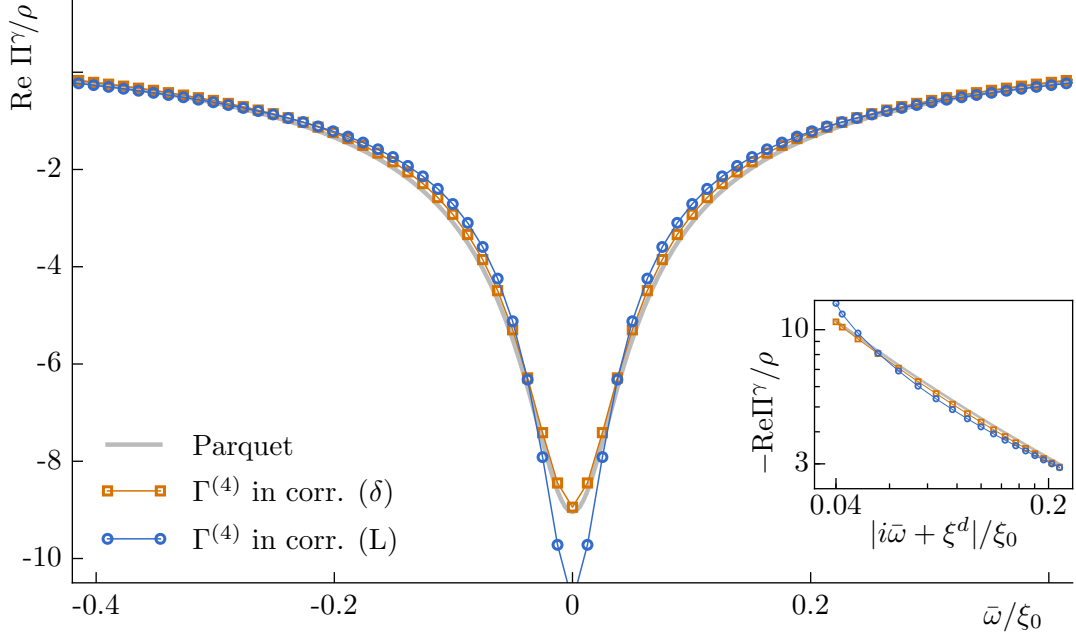


Figure 3.5: Four-point correlator Π^γ or $\langle \bar{d}d\bar{c}c \rangle$ computed via $\Gamma^{(4)}$ [Eq. (3.7)], where $\Gamma^{(4)}$ is obtained from a numeric solution of the fRG flow equation (2.58). Different results are generated using a δ or Litim (L) regulator [cf. Eq. (2.43)] and compared to the parquet formula (3.6). Neglecting $\Gamma^{(6)}$ by truncation, the flow misses parquet graphs starting at third order in U (cf. Fig. 3.9).

We observe qualitative agreement of the curves. The δ -regularized solution follows the exact curve extremely well. By contrast, the curve which results from using a Litim regulator overestimates the singularity and shows deviations from a pure power law, as seen in the logarithmic inset.

Let us try to understand the numerical outcome, based on a solution of the flow equation (2.58), from a diagrammatic perspective. The truncated flow equation is represented graphically in Fig. 3.4. A d line with a vertical dash next to the arrow represents the single-scale propagator; the derivative of a whole diagram is denoted by a dot on top of it. As we know all diagrams of the four-point vertex up to third order (Fig. 3.2), we can check whether they are generated by the flow. For this, note that since, in the infinite-mass case, we can neglect any self-energy contributions, a d propagator is simply differentiated by changing it to a single-scale propagator. A diagram containing multiple d lines is differentiated by respecting the product rule, i.e., summing all diagrams where one d line is changed to a single-scale line at a time.

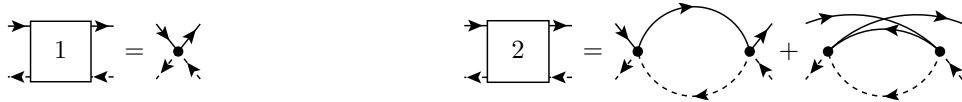


Figure 3.6: First- and second-order diagrams of $\tilde{\Gamma}^{\bar{d}d\bar{c}c}$ group together.

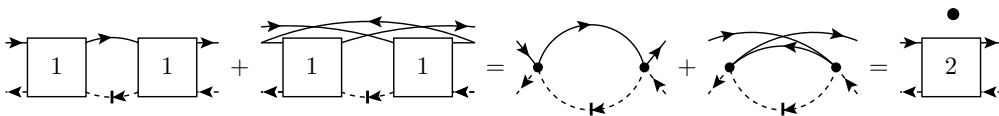


Figure 3.7: The flow equation of $\tilde{\Gamma}^{\bar{d}d\bar{c}c}$ is fulfilled in second order (cf. Fig. 3.4, 3.6).

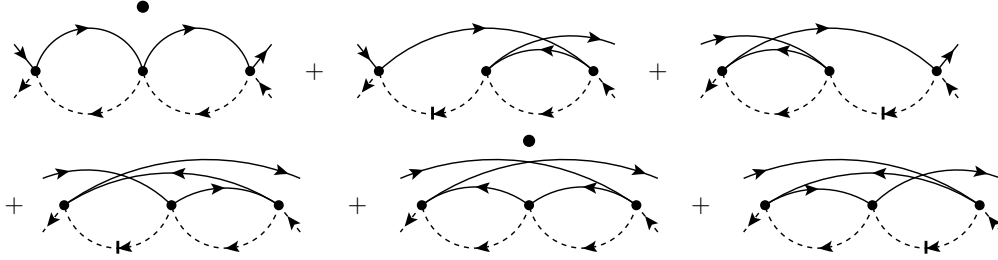


Figure 3.8: First- and second-order diagrams of $\tilde{\Gamma}^{\bar{d}\bar{d}\bar{c}\bar{c}}$ (Fig. 3.6) are inserted in the right-hand side of the flow equation (Fig. 3.4) to form $\partial_\Lambda \tilde{\Gamma}^{\bar{d}\bar{d}\bar{c}\bar{c}}$ at third order. Four diagrams can be grouped together to form two fully differentiated (dotted) ones.



Figure 3.9: The missing diagrams in Fig. 3.8 to complete the derivative of $\tilde{\Gamma}^{\bar{d}\bar{d}\bar{c}\bar{c}}$ at third order come from $\text{Tr}\{S\Gamma^{(6)}\}$ contributions (S is graphically separated) to the flow [cf. Eq. (2.56)].

If we group the leading-order diagrams of Fig. 3.2 according to Fig. 3.6, we immediately see that only diagrams starting at second order contain d lines and thus are scale dependent. Inserting the first-order diagram on the right-hand side of the flow equation (Fig. 3.4), we find that, indeed, the derivative of the four-point vertex at second order is generated (cf. Fig. 3.6, 3.7). To study the flow equation at the next order, we have to insert first- and second-order diagrams on the right-hand side of Fig. 3.4, forming the third-order diagrams shown in Fig. 3.8. Four diagrams can be grouped as two fully differentiated ones (having a dot on top of them); the other contributions cannot be expressed in this way. In light of our earlier observation that, due to the simplified flow, $\Gamma^{\bar{d}\bar{d}\bar{c}\bar{c}}$ is symmetric in the external valence-band frequencies (cf. section 2.2.3), it is not surprising that the fully differentiated diagrams are exactly the ones respecting this symmetry. It is interesting to note that precisely these two diagrams are the ones giving a negative contribution to the particle-hole susceptibility at third order [15]. Assuming a similar imbalance for higher orders as well, one might expect the approximate solution to exaggerate the negative divergence (cf. Fig. 3.5).

The reason why the derivatives of the other diagrams of $\Gamma^{\bar{d}\bar{d}\bar{c}\bar{c}}$ are only partly contained stems from the fact that we neglected the six-point vertex in our truncation of the hierarchy of flow equations. In fact, the missing terms that would be needed to fully recover the derivative of $\Gamma^{\bar{d}\bar{d}\bar{c}\bar{c}}$ at third order come from the contribution of Eq. (2.56), $\text{Tr}\{S_{d\bar{d}}\Gamma_{\bar{d}\bar{d}\bar{d}\bar{d}\bar{c}\bar{c}}\}$, as illustrated in Fig. 3.9. (Out of twelve inequivalent possibilities for diagrams of $\Gamma^{(6)}$ at third order, only the four diagrams shown in Fig. 3.9 are one-particle-irreducible.)

Since a numerical calculation of $\Gamma^{(6)}$ is hopeless (cf. section 2.3), we conclude that the approach via the fermionic four-point vertex deviates from the parquet result starting at third order. It seems therefore legitimate, that the Litim result deviates at small enough frequencies. Surprisingly however, the δ solution matches the prediction extraordinarily well. Next, we will explore whether a better approximation is obtained after using a Hubbard-Stratonovich transformation.

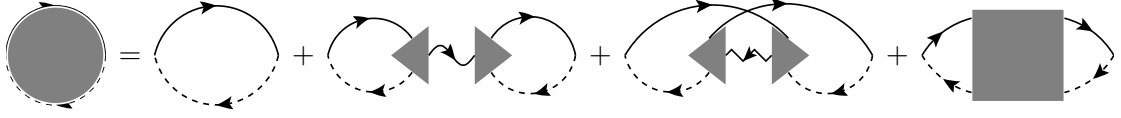


Figure 3.10: Four-point correlator $\langle \bar{d}\bar{d}\bar{c}\bar{c} \rangle$ after a HS transformation determined by HS three-point vertices and the fermionic four-point vertex [cf. Eq. (3.8)]. A wavy (zig-zag) line denotes a full χ (ψ) propagator. Both three-point vertices $\tilde{\Gamma}^{\bar{c}d\chi}$ and $\tilde{\Gamma}^{\bar{c}d\psi}$ are depicted by a full triangle and can be distinguished by the attached bosonic line.

3.2.2 Four-point correlator in the HS-transformed matter system

In the presence of Hubbard-Stratonovich fields, the new relation from Eq. (2.33) between the (connected) correlator and 1PI vertices is given by the equation

$$\begin{aligned} \langle \bar{d}_\omega d_\nu \bar{c}_{\bar{\omega}+\omega} c_{\bar{\omega}+\nu} \rangle_c &= G_\omega^d G_\nu^d G_{\bar{\omega}+\omega}^c G_{\bar{\omega}+\nu}^c \left(-\Gamma_{\omega,\nu,\bar{\omega}+\omega,\bar{\omega}+\nu}^{\bar{d}\bar{d}\bar{c}\bar{c}} \right) \\ &+ G_\omega^d G_\nu^d G_{\bar{\omega}+\omega}^c G_{\bar{\omega}+\nu}^c G_{\bar{\omega}}^\chi \Gamma_{\bar{\omega}+\nu,\nu,\bar{\omega}}^{\bar{c}d\chi} \Gamma_{\omega,\bar{\omega}+\omega,\bar{\omega}}^{\bar{d}\bar{c}\bar{\chi}} \\ &+ G_\omega^d G_\nu^d G_{\bar{\omega}+\omega}^c G_{\bar{\omega}+\nu}^c G_{\bar{\omega}+\omega+\nu}^\psi \left(\Gamma_{\bar{\omega}+\nu,\omega,\bar{\omega}+\omega+\nu}^{\bar{c}d\psi} / i \right) \left(\Gamma_{\nu,\bar{\omega}+\omega,\bar{\omega}+\omega+\nu}^{d\bar{c}\bar{\psi}} / i \right) \end{aligned} \quad (3.8)$$

and illustrated in Fig. 3.10. Graphically, we represent the full χ propagator by a wavy and the full ψ propagator by a zig-zag line. Both three-point vertices (recall the symmetry relations derived in section 2.1.4) $\tilde{\Gamma}^{\bar{c}d\chi}$ and $\tilde{\Gamma}^{\bar{c}d\psi}$ are denoted by a full triangle and can be distinguished by their attached lines.

Note that a bosonic χ or ψ propagator to lowest order is simply given by $-U_x$ or $-U_p$, respectively. A bare propagating boson thus reduces to the instantaneous interaction with adjusted weight U_x or U_p . At second order, the propagators are renormalized by the leading self-energy contributions. For χ , this gives a bubble of antiparallel lines [Eq. (2.26)] times U_x^2 ; for ψ , it is a bubble of parallel lines [Eq. (2.27)] multiplied by U_p^2 . Second-order diagrams from the second and third summand in Fig. 3.10, of course, also come from two first-order three-point vertices and a bare bosonic propagator. The lowest-order diagrams of the three-point vertices in the exchange and pairing channel are shown in Fig. 3.11. The bare three-point vertices (gray circles) require energy-momentum conservation and simply have a prefactor of unity.

If we put bosonic self-energies and three-point vertices together in Fig. 3.10, we get:

$$\begin{aligned} \text{Exchange channel: } &U_x \times (1L) + (U_x^2 + 2U_x U_p) \times (2L) , \\ \text{Pairing channel: } &U_p \times (1L) + (U_p^2 + 2U_x U_p) \times (2C) , \end{aligned} \quad (3.9)$$

where (1L), (2L) are the first- and second-order ladder, (2C) the crossed diagram, which were already shown in Fig. 3.1. With $U_x + U_p = U$ according to Eq. (2.23), combining both channels, the first-order contribution is fully contained. However, at second order, the weight U^2 is not fully recovered. In fact, although the HS transformation by construction ensures that the four-point vertex $\Gamma^{\bar{d}\bar{d}\bar{c}\bar{c}}$ does not contribute to first order, it does contribute to second order. The second-order diagrams for $\tilde{\Gamma}^{\bar{d}\bar{d}\bar{c}\bar{c}}$ which are irreducible in fermionic as well as bosonic lines are the ones represented in Fig. 3.12. Their



Figure 3.11: First-order diagrams of the three-point vertices $\tilde{\Gamma}^{\bar{c}d\chi}$ and $\tilde{\Gamma}^{\bar{c}d\psi}$. The bare vertex, a gray circle, requires energy-momentum conservation with weight unity; the χ or ψ propagator to lowest order is given by $-U_x$ or $-U_p$, respectively.

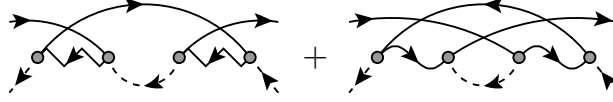


Figure 3.12: After a HS transformation, $\tilde{\Gamma}^{\bar{d}d\bar{c}c}$ contributes, with the above diagrams, starting at second order. It is therefore needed to produce all parquet graphs (up to second order) in the correlator via the relation in Fig. 3.10.

contribution

$$\text{Four-point vertex: } U_x^2 \times (2C) + U_p^2 \times (2L) \quad (3.10)$$

completes the weight to fully recover the second-order graphs (Fig. 3.1), since adding Eq. (3.9) and Eq. (3.10) yields

$$U \times (1L) + U^2 \times [(2L) + (2C)] . \quad (3.11)$$

We conclude that the use of a HS transformation does not save us from having to calculate the four-point vertex even at second order in U . Nevertheless, it is interesting to numerically check how the three-point vertices, evolved by the flow in the HS-transformed matter system, form the four-point correlator, where the computational advantage of this strategy is only present if the four-point 1PI vertex is excluded from the system. By using only the first three terms on the right-hand side of Fig. 3.10, but discarding the fourth, we incorporate the hypothetically useful resummation of dynamic HS fields but omit important contributions starting at second order in U .

In the plot in Fig. 3.13, we show the four-point correlator obtained via the HS three-point vertices. The curves give qualitatively reasonable results at intermediate frequencies, but for small enough frequencies the penalty of ignoring $\Gamma^{(4)}$ manifests itself in strong deviations from the analytic formula. This time, the δ regularized solution shows a stronger divergence, and the Litim curve seems to fit somewhat better.

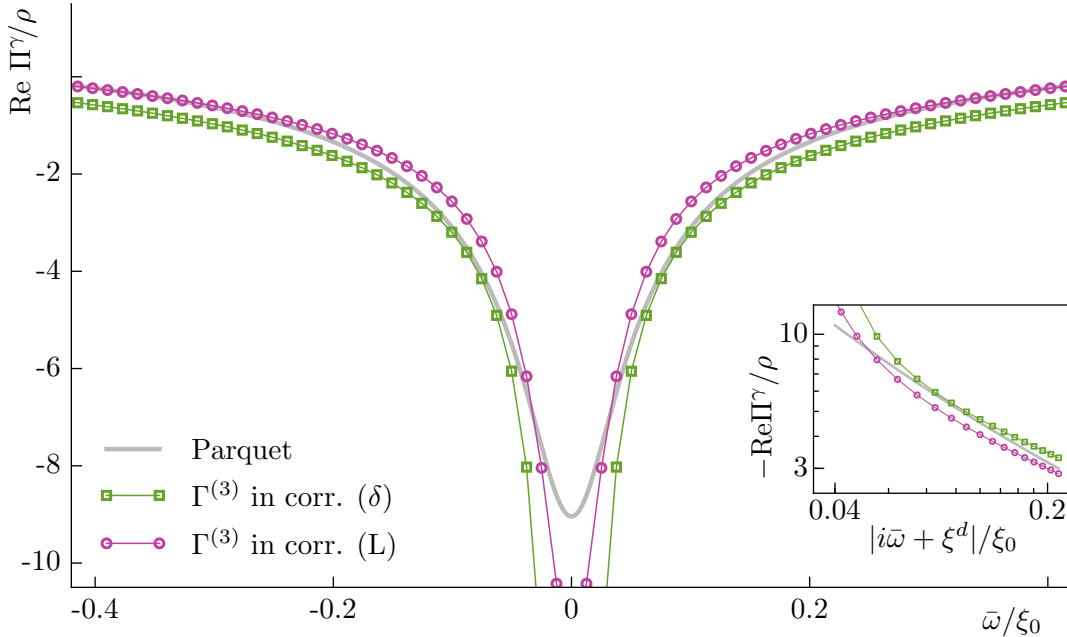


Figure 3.13: Four-point correlator Π^γ or $\langle \bar{d}d\bar{c}c \rangle$ obtained from $\tilde{\Gamma}^{\bar{c}d\bar{x}}$ and $\tilde{\Gamma}^{\bar{c}d\bar{\psi}}$ according to the first three terms on the right-hand side of Fig. 3.10. Contributions from $\tilde{\Gamma}^{\bar{d}d\bar{c}c}$, starting at second order (cf. Fig. 3.12), are neglected. The three-point vertices were obtained by solving the flow equations in section 2.2.5, using the two (δ and Litim) regulators.



Figure 3.14: Truncated flow equations of the photon self-energy (Π^γ , circle) and three-point vertex ($\tilde{\Gamma}^{cd\gamma}$, triangle) in the light-matter system [Eq. (2.61) and (2.63)], where the contributions of $\Gamma^{\bar{d}d\gamma\bar{\gamma}}$ [for Π^γ , Eq. (2.60)] and $\Gamma^{\bar{d}dc̄d\gamma}$ [for $\tilde{\Gamma}^{cd\gamma}$, Eq. (2.62)] are neglected. External wavy lines denote amputated photon legs, and the flow of the four-point vertex $\tilde{\Gamma}^{\bar{d}dc̄c}$ is still given by Eq. (2.58) (i.e., Fig. 3.4).

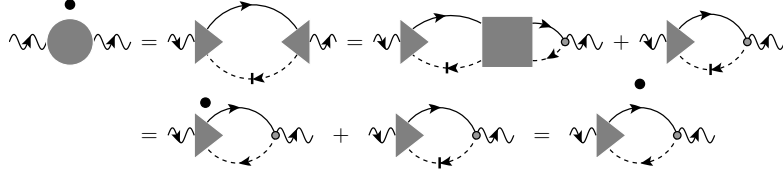


Figure 3.15: Given the approximate flow of Π^γ and $\tilde{\Gamma}^{cd\gamma}$ according to Eq. (2.61) and Eq. (2.63) (i.e., Fig. 3.14), the evolution of Π^γ respects the Schwinger-Dyson equation (2.39).

3.2.3 Self-energy in the light-matter system

We move on to the light-matter system, including the photon into the theory (but disregarding HS fields). One obtains the particle-hole susceptibility in the form of the photon self-energy, since the fRG scheme set up in section 2.2.4 incorporates the limit $|M|^2 \rightarrow 0$. The truncated flow equations involving the photon, Eq. (2.61) and (2.63), are graphically represented in Fig. 3.14. External (quickly oscillating) wavy lines symbolize the amputated photon legs, the full circle the photon self-energy, and the full triangle attached to a photonic line the three-point vertex $\tilde{\Gamma}^{cd\gamma}$ (not to be confused with the HS three-point vertices from the previous section). The fermionic four-point vertex, relevant for the flow of $\tilde{\Gamma}^{cd\gamma}$, still obeys the flow equation in Fig. 3.4, which is closed in itself.

The flow of the γ self-energy only depends on $\tilde{\Gamma}^{cd\gamma}$. In fact, given a three-point vertex

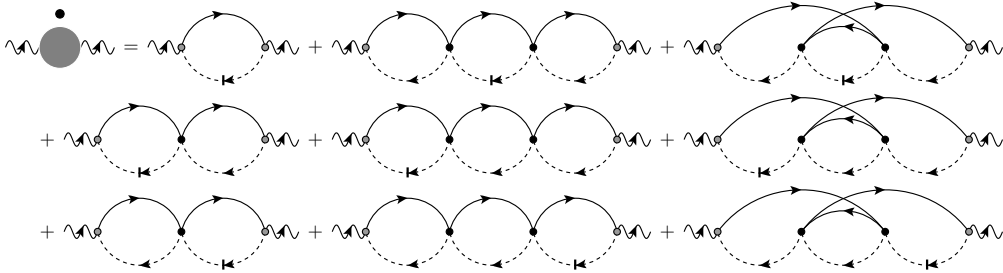


Figure 3.16: Derivative of the leading-order photon self-energy Π^γ (i.e., the four-point correlator) up to second order obtained from Fig. 3.1 by changing a d line to a single-scale propagator in all possible ways. The gray circle attached to amputated photon legs is the bare (rescaled) photon three-point vertex equal to unity.



Figure 3.17: Flow equation of Π^γ up to second order in terms of $\tilde{\Gamma}^{cd\gamma}$ (cf. Fig. 3.16, 3.18). Whereas neglected in Fig. 3.14, the four-point vertex $\Gamma^{\bar{d}d\gamma\bar{\gamma}}$ is needed for parallel S^d - G^c lines and contributes via $\text{Tr}\{S\Gamma^{(4)}\}$ (cf. Eq. (2.60), S is graphically separated).

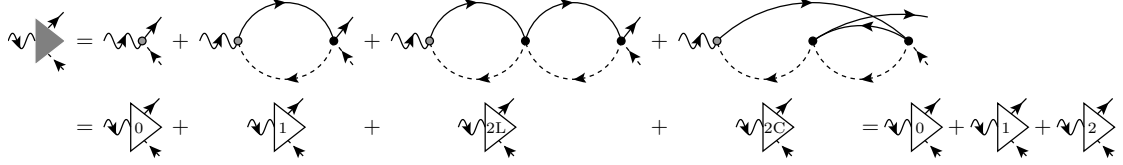


Figure 3.18: Low-order contributions to $\tilde{\Gamma}^{cd\gamma}$ following from the Schwinger-Dyson equation (2.41) and the diagrammatic expansion of $\tilde{\Gamma}^{\bar{d}dc}$ (Fig. 3.2). Definitions are made for future purposes.

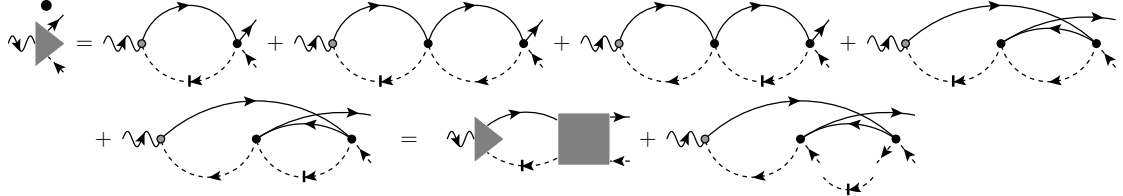


Figure 3.19: Flow of $\tilde{\Gamma}^{cd\gamma}$ up to second order. Rewriting via $\tilde{\Gamma}^{\bar{d}dc}$ as in Eq. (2.63) shows that the five-point vertex $\Gamma^{\bar{d}dc\gamma}$ [cf. Eq. (2.62)], neglected in Fig. 3.14, is needed for parallel S^d - G^c lines. (S is graphically separated in the term $\text{Tr}\{S\Gamma^{(5)}\}$).

obeying the truncated flow of Fig. 3.14 (right), it is equivalent to calculate the self-energy from its respective, approximate flow (Fig. 3.14, left) or from the (exact) Schwinger-Dyson equation (2.39). This is diagrammatically proven in Fig. 3.15. Inserting the form of the photonic three-point vertex given by the fermionic four-point vertex [Eq. (2.41)] into the derivative of the self-energy, and using its flow of Fig. 3.14, the derivative of the self-energy is equally obtained as if the Schwinger-Dyson equation (2.39) were differentiated in the first place. As a minor remark, one can understand the approximate nature of the truncated flow of $\tilde{\Gamma}^{cd\gamma}$ in Fig. 3.14 also by differentiating the second

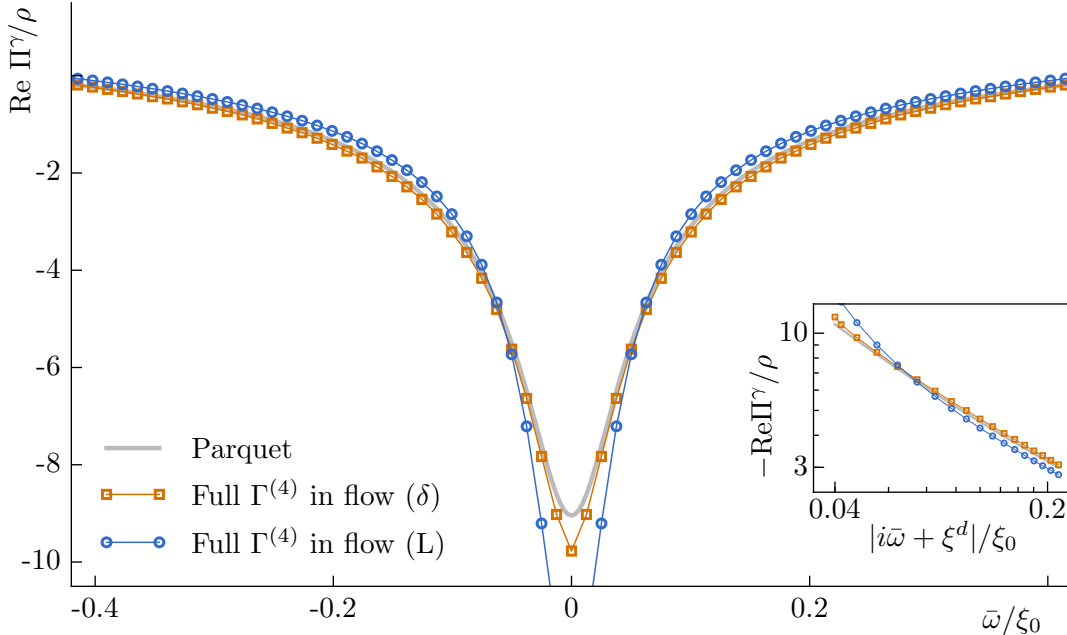


Figure 3.20: Self-energy obtained from the flow of the light-matter system (Fig. 3.14), where the evolving $\Gamma^{\bar{d}dc}$ (Fig. 3.4) is used. Stronger deviations (for both regulating schemes) from the parquet curve compared to Fig. 3.5 are explained by the neglected contributions of the truncated flow (cf. Fig. 3.17, Fig. 3.19), omitting the derivatives of parallel bubbles.

Schwinger-Dyson equation (2.41). Inserting the exact flow of $\Gamma^{\bar{d}d\bar{c}c}$, one finds that the truncated flow of $\Gamma^{\bar{c}d\gamma}$ not only neglects $\Gamma^{(6)}$ contributions but also the “crossed” part of the derivative of $\Gamma^{(4)}$, i.e., the second summand in Fig. 3.4.

The diagrams forming the derivative of Π^γ up to second order can be deduced from the low-order diagrammatic representation of the particle-hole susceptibility in Fig. 3.1. By changing a d line to single-scale propagator in all possible ways, we arrive at the set of graphs shown in Fig. 3.16. A gray circle denotes the bare (rescaled) photon three-point vertex equal to unity. Rewriting these second-order diagrams in terms of the three-point 1PI vertex, known from its connection to the four-point vertex [Eq. (2.41)] and graphically represented up to second order in Fig. 3.18, one obtains the relation shown in Fig. 3.17.

We see that a diagram with a single-scale propagator parallel to a c line cannot be rephrased in terms of only two photonic three-point vertices. Instead, the four-point vertex $\Gamma^{\bar{d}d\bar{\gamma}\gamma}$, connecting photons and fermions, is needed (cf. Eq. (2.60), second diagram on the right-hand side of Fig. 3.17). Similarly, expressing the second-order derivative of $\tilde{\Gamma}^{\bar{c}d\gamma}$ according to Fig. 3.14, parallel single-scale and c lines require a higher-order, viz., five-point vertex (cf. Fig. 3.19). In the truncated flow equations of section 2.2.4, represented in Fig. 3.14, these higher-order, initially vanishing contributions are neglected. Here, we see that, at second order, they contain important contributions originating from the derivative of the crossed diagram.

The numeric solutions in the light-matter system also omits these contributions, since generating $\Gamma^{\bar{d}d\bar{\gamma}\gamma}$ or $\Gamma^{\bar{d}d\bar{c}d\gamma}$ in the flow requires at least five-point vertices (cf. section 2.2.4), which are inaccessible due to computational limitations (cf. section 2.3). The results for the particle-hole susceptibility obtained from the truncated flow (Fig. 3.14, 3.4) are shown in Fig. 3.20. The curves differ more strongly from the analytic formula than the ones which are obtained by forming the correlator via the four-point vertex directly (Fig. 3.5). This is understood as the approximations in the photonic flow weaken

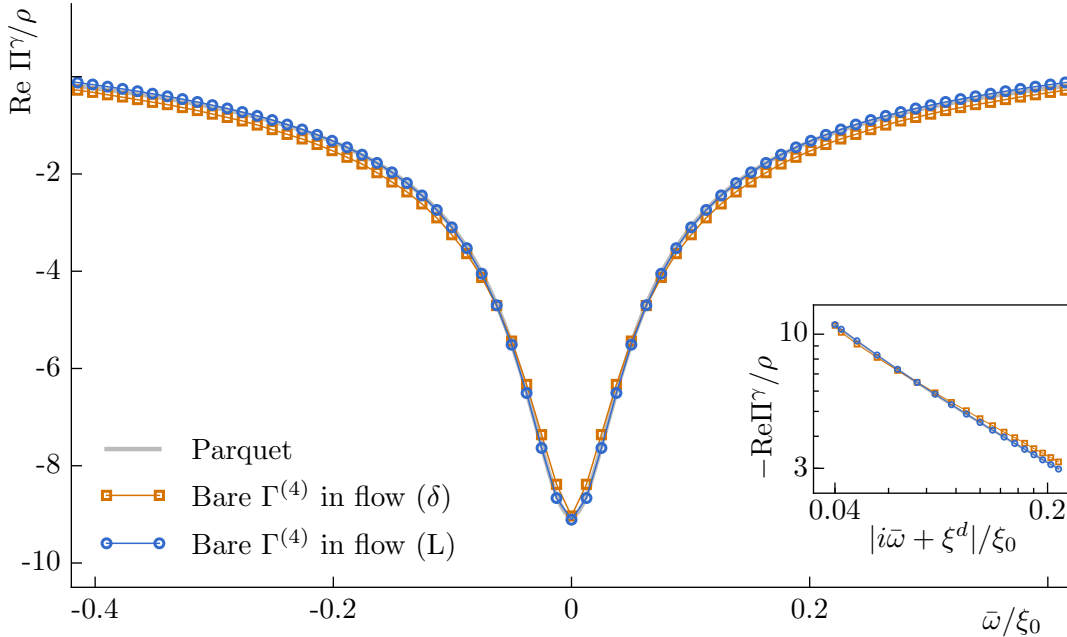


Figure 3.21: Self-energy obtained from the flow of the light-matter system (Fig. 3.14), where the bare four-point vertex $\tilde{\Gamma}^{\bar{d}d\bar{c}c} = -U$ is used. The outstandingly good agreement with the parquet formula, independent of the regulating scheme, is explained by partial diagrammatic cancellations (cf. Fig. 3.26). Increasing β and N enables perfect congruence with the prediction.

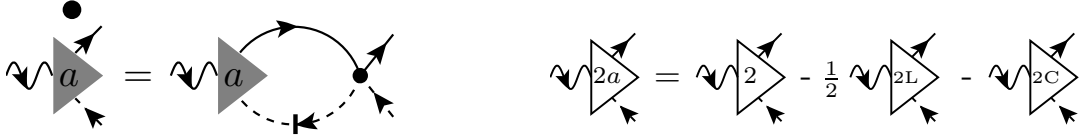


Figure 3.22: Flow equation for an approximate photonic three-point vertex, when $\tilde{\Gamma}^{\bar{d}d\bar{c}c}$ is reduced to its bare part (cf. Eq. (2.63), Fig. 3.14), and its solution at second order (whose ingredients are defined in Fig. 3.18).

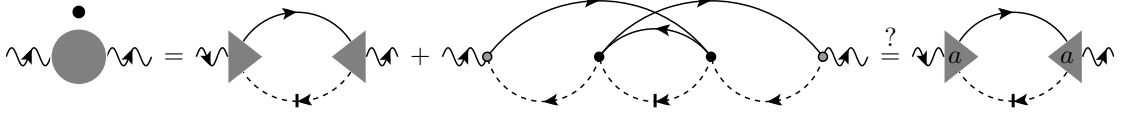


Figure 3.23: Second order flow of Π^γ according to Fig. 3.17 and in the truncated form of Fig. 3.14 with the approximate three-point vertex from Fig. 3.22.

the predictive power of the fRG solution. One can even employ the following argument. The simplifications in the flow equations neglect the derivatives of parallel bubbles at all orders. At second order, we have explicitly seen that the parallel bubble is part of the crossed diagram (cf. Fig. 3.1), which gives a positive contribution and reduces the singularity arising from the summation of (negative) ladder diagrams. Missing diagrams with parallel bubbles should therefore lead to a more strongly diverging result.

Now, observe a surprising effect. The numerical effort in solving the system of flow equations decreases dramatically when using a static four-point vertex. Instead of $\tilde{\Gamma}^{\bar{d}d\bar{c}c}$ being evolved and generating all sorts of diagrams, it is kept at the initial value of a constant, bare vertex $\tilde{\Gamma}^{\bar{d}d\bar{c}c} = -U$ (granted energy conservation in the arguments). In Fig. 3.21, we see an agreement of the corresponding numerical solution to the analytic prediction superior to any previous treatment (especially when using the Litim regulator). In fact, the system of differential equations is simplified so much that it is numerically feasible to increase β and N until a perfect matching (of both numeric curves) to the parquet formula is achieved.

Let us explain this outcome. First, we show the underlying idea at second order; then, we extend our argument to all orders. Fig. 3.22 depicts the flow equation for an approximate three-point vertex $\tilde{\Gamma}^{\bar{c}d\bar{\gamma}}$ without higher-order vertices and where the fermionic four-point vertex (as in Fig. 3.14) is kept bare, i.e., $\tilde{\Gamma}^{\bar{d}d\bar{c}c} = -U$. Its solution at second order can be obtained by modifying the original three-point vertex from Fig. 3.18, subtracting the crossed part and half of the second-order ladder diagram (Fig. 3.22). Making use of the factorizing properties of ladder diagrams, the solution to the simplified

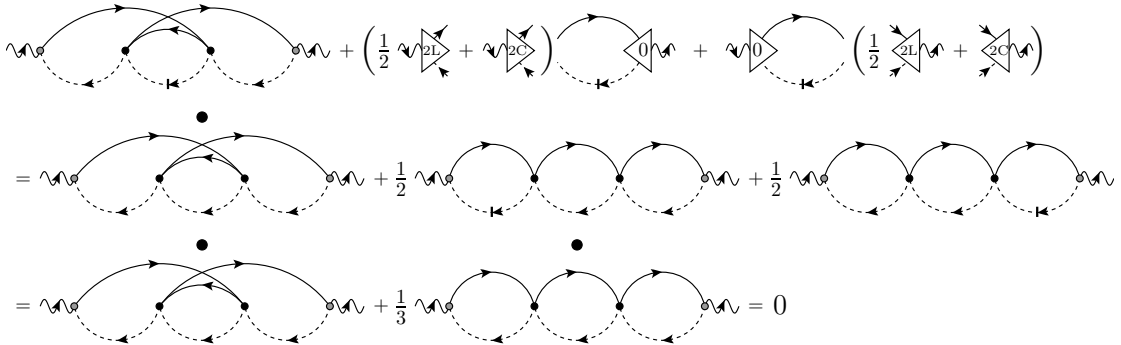


Figure 3.24: Inserting the approximate three-point vertex from Fig. 3.22 in Fig. 3.23, and bringing its modifications to the left-hand side, we see that the additional terms exactly cancel the $\Gamma^{\bar{d}d\bar{\gamma}\gamma}$ contribution in the flow of Π^γ , using the factorization of subsequent bubbles and $\Pi^{(2L)} = -3\Pi^{(2C)}$ [Eq. (3.5)].

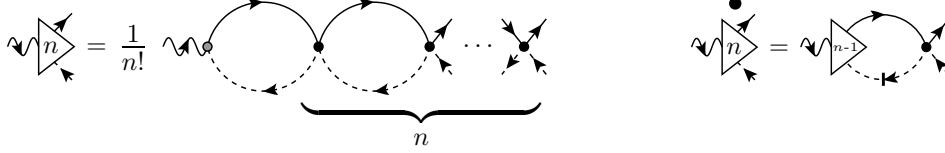


Figure 3.25: Approximate three-point vertex at order n and its derivative fulfilling the approximate flow equation with bare $\Gamma^{(4)}$ (cf. Fig. 3.22).

flow equation is easily confirmed. Can this approximate three-point vertex give a correct photon self-energy upon neglecting the four-point photon-fermion vertex $\Gamma^{dd\bar{\gamma}\gamma}$, i.e., does the equality in Fig. 3.23 hold?

This is indeed true thanks to a cancellation procedure. Inserting the approximate three-point vertex in the approximate flow of Π^γ (rightmost diagram in Fig. 3.23), one finds that the subtracted terms exactly make up for the four-point vertex contribution (second summand in the middle of Fig. 3.23). A diagrammatic proof is shown in Fig. 3.24, where the modifications of $\tilde{\Gamma}^{cd\gamma}$ are brought to the left-hand side and combined with the $\Gamma^{dd\bar{\gamma}\gamma}$ graph. Using the factorization properties of ladder diagrams and the fact that, for infinite hole mass and with logarithmic accuracy, the crossed diagram counts $-1/3$ of the value of the second-order ladder diagram [cf. Eq. (3.5)], the cancellation is perfect. Consequently, the diagrammatic solution of the simplified system of flow equations exactly agrees with the parquet graphs up to and including second order.

A closer look at the approximate three-point vertex in Fig. 3.22 reveals that it consists only of ladder diagrams with a factor of $1/2$ in second order; as a matter of fact, the crossed contribution has been completely subtracted. If we extrapolate this to all orders, we can define a new three-point vertex as in Fig. 3.25. Clearly, the simplified flow equation is fulfilled. In fact, one can easily see that it is the unique solution of this flow equation: Starting by inserting the bare vertex in the flow equation, the derivative of the first-order ladder diagram is generated. Iterating this procedure, only ladder diagrams are possible and the appropriate prefactor is $1/n!$.

Inserting this three-point vertex in the truncated self-energy flow (as in Fig. 3.14), we can simplify the equation, again using the factorizing properties of ladder diagrams. In Fig. 3.26, the flow of the self-energy at order n , $\partial_\Lambda \Pi^{\gamma,(n)}$, determined by both ladder-type three-point vertices summed up to the same order, is related to the derivative of the n^{th} -order ladder diagram $\Pi^{(n,L)}$. In the last step, we made use of the following identity,

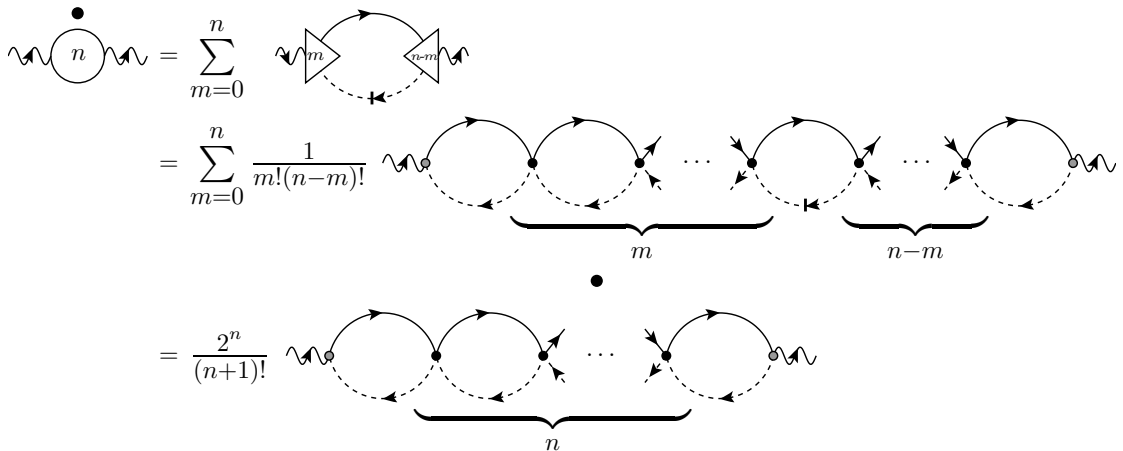


Figure 3.26: Inserting the approximate three-point vertex from Fig. 3.25 in the approximate flow of Π^γ (cf. Fig. 3.23), we relate the self-energy to ladder diagrams at arbitrary order n in exact agreement with the parquet result [cf. Eq. (3.14)].

and $\Pi^{(n,L)}$ is known from Eq. (3.5):

$$\sum_{m=0}^n \frac{1}{m!(n-m)!} = \frac{2^n}{n!}, \quad \Pi^{(n,L)} = (-U)^n (\rho L)^{n+1}, \quad L = \ln \left(\frac{-i\bar{\omega} - \xi^d}{\xi_0} \right). \quad (3.12)$$

The last line in Fig. 3.26 relates two derivatives of diagrams, where both sides contain d -lines, thus vanish at the initial scale $\Lambda = \infty$. Consequently, they remain equal throughout the flow:

$$\Pi^{\gamma,(n)} = \frac{2^n}{(n+1)!} \Pi^{(n,L)}. \quad (3.13)$$

Summation of all orders precisely yields the parquet result [cf. Eq. (3.6)]

$$\begin{aligned} \Pi_{\bar{\omega}}^{\gamma} &= \sum_{n=0}^{\infty} \Pi^{\gamma,(n)} = \sum_{n=0}^{\infty} \frac{2^n}{(n+1)!} \Pi^{(n,L)} = -\frac{1}{2U} \sum_{n=0}^{\infty} \frac{(-2uL)^{n+1}}{(n+1)!} \\ &= -\frac{1}{2U} \left(e^{-2uL} - 1 \right) = \frac{1}{2U} \left[1 - \left(\frac{-i\bar{\omega} - \xi^d}{\xi_0} \right)^{-2u} \right]. \end{aligned} \quad (3.14)$$

We conclude that in the combined, truncated flow of the light-matter system parquet graphs are missed starting at second order due to a mistreatment of parallel bubbles. If, however, only the bare fermionic four-point vertex $\tilde{\Gamma}^{\bar{d}d\bar{c}c} = -U$ is used, the indispensable and initially neglected contributions to Π^{γ} from higher-point vertices are fortuitously generated by the approximate flow itself, resulting in the full parquet result.

3.3 Analytic results

Inspired by numerical data and diagrammatic considerations from the previous section, we are able to reproduce the infinite-mass parquet result analytically (and purely algebraically). This proceeds in a straightforward manner from a truncated system of flow equations. Hereafter, we will extend our arguments to the finite-hole-mass case and with a few ideas come close to the generalized parquet result of Eq. (1.10).

3.3.1 Parquet formula from a static four-point vertex

Let us adopt a harsh but sensible truncation of the flow equations: we keep all 1PI vertices starting from the four-point vertex at their initial value. Only the (energy-momentum conserving) fermionic four-point vertex has a non-vanishing value at $\Lambda = \infty$ and is constantly equal to $-U$. The simplified flow equations [Eq. (2.61), (2.63)] then read

$$\begin{aligned} \partial_{\Lambda} \Pi_{\Lambda, \bar{\omega}}^{\gamma} &= \int_{\omega} S_{\Lambda, \omega}^d G_{\bar{\omega}+\omega}^c \left(\tilde{\Gamma}_{\Lambda, \bar{\omega}+\omega, \omega, \bar{\omega}}^{\bar{c}d\gamma} \right)^2, \\ \partial_{\Lambda} \tilde{\Gamma}_{\Lambda, \omega_c, \omega_c - \bar{\omega}, \bar{\omega}}^{\bar{c}d\gamma} &= \int_{\omega} S_{\Lambda, \omega}^d \tilde{\Gamma}_{\Lambda, \bar{\omega}+\omega, \omega, \bar{\omega}}^{\bar{c}d\gamma} G_{\bar{\omega}+\omega}^c \tilde{\Gamma}_{\Lambda, \omega, \omega_c - \bar{\omega}, \omega_c, \bar{\omega}+\omega}^{\bar{d}d\bar{c}c} \\ &= -U \int_{\omega} S_{\Lambda, \omega}^d G_{\bar{\omega}+\omega}^c \tilde{\Gamma}_{\Lambda, \bar{\omega}+\omega, \omega, \bar{\omega}}^{\bar{c}d\gamma} \end{aligned} \quad (3.15)$$

and can be visualized by replacing the full four-point vertex in Fig. 3.14 by its bare part (cf. Fig. 3.2b, 3.22).

The important observation is that the first derivative (and consequently any higher derivative) of $\tilde{\Gamma}_{\Lambda}^{\bar{c}d\gamma}$ is independent of ω_c , i.e., completely independent of the first argument. (The second argument is fixed by conservation anyway.) Since also the initial condition is independent of the first argument, the vertex only depends on $\bar{\omega}$ for all

scales. It is easy to see that the (2C) diagram from Fig. 3.18 in the three-point vertex is not independent of fermionic frequencies. Hence, this is a violation of the actual properties of the renormalized three-point vertex and corresponds to the fact that one effectively only sums up ladder diagrams (cf. Fig. 3.25).

It follows that $\bar{\omega}$ merely acts as an external parameter for these flow equations, and its effect can be restricted considerably. The solution of the differential equations (3.15) is easily obtained with the definition $g_{\Lambda, \bar{\omega}} = (\tilde{\Gamma}_{\Lambda, \cdot, \cdot, \bar{\omega}}^{cd\gamma})^2$, such that

$$\begin{aligned}\partial_{\Lambda} g_{\Lambda, \bar{\omega}} &= -2U g_{\Lambda, \bar{\omega}} \int_{\omega}' S_{\Lambda, \omega}^d G_{\bar{\omega}+\omega}^c, \\ \partial_{\Lambda} \Pi_{\Lambda, \bar{\omega}}^{\gamma} &= g_{\Lambda, \bar{\omega}} \int_{\omega}' S_{\Lambda, \omega}^d G_{\bar{\omega}+\omega}^c = -\frac{1}{2U} \partial_{\Lambda} g_{\Lambda, \bar{\omega}}.\end{aligned}\quad (3.16)$$

Evidently, $g_{\Lambda, \bar{\omega}}$ is given by an exponential of an auxiliary function $f_{\Lambda, \bar{\omega}}$:

$$g_{\Lambda, \bar{\omega}} = g_{\Lambda_0, \bar{\omega}} e^{-2u f_{\Lambda, \bar{\omega}}}, \quad f_{\Lambda, \bar{\omega}} = \int_{\Lambda_0}^{\Lambda} d\Lambda' \int_{\omega}' S_{\Lambda', \omega}^d G_{\bar{\omega}+\omega}^c / \rho. \quad (3.17)$$

The self-energy is directly related and becomes

$$\Pi_{\Lambda, \bar{\omega}}^{\gamma} = \Pi_{\Lambda_0, \bar{\omega}}^{\gamma} - \frac{g_{\Lambda, \bar{\omega}} - g_{\Lambda_0, \bar{\omega}}}{2U} = \Pi_{\Lambda_0, \bar{\omega}}^{\gamma} - \frac{g_{\Lambda_0, \bar{\omega}}}{2U} [e^{-2u f_{\Lambda, \bar{\omega}}} - 1]. \quad (3.18)$$

Inserting the boundary conditions when Λ flows from ∞ to 0 gives the following result, where the external energy-momentum $\bar{\omega}$ enters only as parameter for the auxiliary function:

$$f_{\bar{\omega}} = \int_{\infty}^0 d\Lambda \int_{\omega}' S_{\Lambda, \omega}^d G_{\bar{\omega}+\omega}^c / \rho, \quad \Pi_{\bar{\omega}}^{\gamma} = \frac{1}{2U} [1 - e^{-2u f_{\bar{\omega}}}] . \quad (3.19)$$

This result is as applicable for infinite hole mass as it is to the finite-mass case; the valence-band self-energy is still included in the single-scale propagator. However, in the infinite-mass case, where self-energies are irrelevant, we have the tremendous simplification $S_{\Lambda}^d = \partial_{\Lambda} G_{\Lambda}^d$. A trivial integration yields the parquet result [cf. Eq. (3.6)]:

$$f_{\bar{\omega}} = \int_{\omega}' G_{\omega}^d G_{\bar{\omega}+\omega}^c / \rho = \ln \left(\frac{-i\bar{\omega} - \xi^d}{\xi_0} \right), \quad \Pi_{\bar{\omega}}^{\gamma} = \frac{1}{2U} \left[1 - \left(\frac{-i\bar{\omega} - \xi^d}{\xi_0} \right)^{-2u} \right]. \quad (3.20)$$

Note that, our numerical solution solves the set of differential equations as stated in Eq. (3.15). In particular, this amounts to calculating the ‘‘single-scale bubble’’ $\int_{\omega}' S_{\omega}^d G_{\bar{\omega}+\omega}^c$ first and then evolving in flow parameter space. This can also be done analytically; details for illustration are shown in the appendix, section A.3. If desired, in the advanced form of Eq. (3.19) and in the more general case of $S_{\Lambda}^d \neq \partial_{\Lambda} G_{\Lambda}^d$, one can interchange the limits and compute an adjusted bubble,

$$f_{\bar{\omega}} = \int_{\omega}' \tilde{G}_{\omega}^d G_{\bar{\omega}+\omega}^c / \rho, \quad \tilde{G}_{\omega}^d = \int_{\infty}^0 d\Lambda S_{\Lambda, \omega}^d. \quad (3.21)$$

Let us give a minor remark about a possible extension beyond leading-order parquet, where the valence-band self-energy Σ^d needs to be accounted for. The next-order correction to the exponent is $-2u \rightarrow -2u + u^2$, as can be extracted from the exact solution of Nozières and De Dominicis [5]. We have already explained that, attributing the constant Hartree part to the renormalized gap, Σ^d starts at second order in the interaction. Correspondingly, for weak coupling, its exact solution is an even function of u [5]. Therefore, including Σ^d in the single-scale bubble cannot generate the correction linear in u , $f = L \rightarrow L \cdot (1 - u/2)$, needed for the exponent of the extended parquet result. Similarly as the diagrammatic cancellations relied on leading log. arguments, the above analytic solution does not extend beyond first-order parquet.

3.3.2 Application for finite hole mass

The flow equations in section 2 have been stated in full generality. For finite hole mass, every 1PI vertex also has momentum dependencies; one merely has to identify each label ω with a multi-index (ω, \mathbf{k}) . Due to the increased number of arguments, a numeric treatment along the lines of the infinite-mass case is impossible.

On the other hand, the finite-mass case (still in first-order parquet) involves a new, important aspect: at the direct threshold ω_D , the valence-band self-energy can no longer be neglected (cf. section 1.4) and incorporates the “dramatic consequence of [...] indirect transitions” [9]. We have already clarified that a resummation of infinitely many diagrams is only needed when the mass ratio b is exponentially small in the coupling. Using $\ln(bu^2) \approx \ln b$, the crossed diagram is proportional to the ladder diagram [cf. Eq. (1.9)] with the same factor as for infinite hole mass. Hence, we can hope that the cancellation of diagrams that led to the parquet result using a static four-point vertex is similarly applicable in the finite-mass situation. Thus, Eq. (3.19) has to be solved with the finite-mass single-scale propagator.

Given the smallness of b , it is easy to believe that the qualitative difference of the finite-mass case does not arise from the modification of the valence-band propagator by changing $\xi^d \rightarrow \xi_k^d = \xi_0^d + b\epsilon_k$. It arises from the self-energy, which can be treated very simplistically, namely to cut the integration range [cf. [9], Eq. (22), (23), appendix A; [11], Eq. (2.129), (4.44)–(4.48)]. The real-frequency self-energy at Fermi momentum is taken to be very large for $\omega < -\omega_I$ and to vanish otherwise, such that, for some function h ,

$$\frac{1}{h(\omega, \mathbf{k}) - \Sigma_{\text{real freq.}}^d(\omega, k_F)} \approx \frac{\Theta(\omega + \omega_I)}{h(\omega, \mathbf{k})} = \frac{\Theta(\omega - b\mu + \omega_D)}{h(\omega, \mathbf{k})}. \quad (3.22)$$

Using k_F in Σ^d is justified by the presence of the conduction-band propagator centered around the Fermi momentum [cf. Eq. (3.23)]. The Θ function will eventually produce cut logarithms, which are treated with logarithmic accuracy again, $\ln(u^2b) \sim \ln(b)$, etc., such that factors exceeding orders of magnitude next to b can be ignored.

It will be advantageous to set the frequency threshold $\xi_{k_F}^d = \omega_D$ to zero. In our discussion in section 2.3, we have already mentioned that, after including all physical implications of a large gap energy, ξ^d merely gives a real shift to the imaginary-frequency dependence encoded in $i\bar{\omega}$. However, since intermediate calculations in imaginary-frequency space are discontinuous with respect to ξ^d at $\xi^d = 0$ [cf. Eq. (A.27)], one loses analytic properties via the phase of the logarithm and is limited to the real part $\ln|\bar{\omega}|/\xi_0$. Thankfully, one can use general analyticity properties such as Kramers-Kronig relations for the real-frequency Green’s function to revert to the full functional form a posteriori.

Going back to the valence-band self-energy in Eq. (3.22) and changing to Matsubara frequencies, we cannot expect to get such a sharp cutoff. The singularity at the threshold frequency appears in real-frequency space only. However, if—with logarithmic accuracy as just discussed—we measure the imaginary frequencies right from the threshold frequency, we can use the following consideration. Σ^d is analytic in the upper-half complex plane, and its modulus for real frequencies above $\omega_I = \omega_D - b\mu \rightarrow -b\mu$ is considered large enough to completely suppress the integral. For small enough temperature, the Matsubara frequencies come arbitrarily close to the real axis, and in a neighborhood of ω_I extending into the upper half-plane²⁰, Σ^d will still have a large value and dominate the integral at small Matsubara frequencies. The cutoff in our treatment comes from the scale dependence seen as follows.

²⁰The Matsubara self-energy in the lower half-plane is of course related via $\Sigma^d(-w, k) = \Sigma^d(w, k)^*$.

We follow the strategy of integrating first in frequency and then in parameter space (as done in the appendix, section A.3, for infinite hole mass). Recalling the local form of the c propagator [Eq. (2.68)], and $|\bar{\omega}| \ll \xi_0$ when setting $\xi_{k_F}^d = \omega_D \rightarrow 0$, we calculate the single-scale bubble (at zero external momentum) using a δ -regulated procedure:

$$\begin{aligned} \int_{\omega, \mathbf{k}}' S_{\Lambda, \omega, \mathbf{k}}^d G_{\bar{\omega}+\omega, \mathbf{k}}^c / \rho &= \frac{1}{\rho} \int_{\omega, \mathbf{k}}' \frac{-\delta(|\omega| - \Lambda)}{i\omega - \xi_k^d - \Sigma_{\Lambda}^d(\omega, k)} \frac{1}{i\omega + i\bar{\omega} - \xi_k^c} \\ &\approx \frac{1}{\rho} \int_{\omega}' \frac{-\delta(|\omega| - \Lambda)}{i\omega - \xi_{k_F}^d - \Sigma_{\Lambda}^d(\omega, k_F)} \int_{\mathbf{k}}' \frac{1}{i\omega + i\bar{\omega} - \xi_k^c} \\ &\approx \frac{i}{2} \int_{-\xi_0}^{\xi_0} d\omega \operatorname{sgn}(\bar{\omega} + \omega) \frac{\delta(|\omega| - \Lambda)}{i\omega - \Sigma_{\Lambda}^d(\omega, k_F)}. \end{aligned} \quad (3.23)$$

The self-energy's frequency argument is determined by the flow parameter. In the finite-mass regime, a small energy scale is given by the recoil energy $b\mu$. Factors multiplying this cutoff are ignored anyway. We make the approximation

$$\Sigma_{\Lambda > b\mu}^d(|\omega| > b\mu) \approx \Sigma_{\Lambda=\infty}^d = 0, \quad \Sigma_{\Lambda < b\mu}^d(|\omega| < b\mu) \approx \Sigma_{\Lambda=0}^d(|\omega| < b\mu), \quad (3.24)$$

where the value $\Sigma^d(|\omega| < b\mu)$ is dominantly large. We thus have

$$\frac{1}{i\omega - \Sigma_{|\omega|}^d(\omega, k_F)} \approx \frac{\Theta(|\omega| - b\mu)}{i\omega}. \quad (3.25)$$

Inserting this self-energy in the single-scale bubble yields

$$\begin{aligned} \int_{\omega, \mathbf{k}}' S_{\Lambda, \omega, \mathbf{k}}^d G_{\bar{\omega}+\omega, \mathbf{k}}^c / \rho &= \frac{i}{2} \int_{-\xi_0}^{\xi_0} d\omega \delta(|\omega| - \Lambda) \frac{\operatorname{sgn}(\bar{\omega} + \omega)}{i\omega - \Sigma_{|\omega|}^d(\omega, k_F)} \\ &\approx \frac{i}{2} \Theta(\xi_0 - \Lambda) \Theta(\Lambda - b\mu) \sum_{\omega=\pm\Lambda} \frac{\operatorname{sgn}(\bar{\omega} + \omega)}{i\omega} \\ &= \Theta(\xi_0 - \Lambda) \Theta(\Lambda - b\mu) \Theta(\Lambda - |\bar{\omega}|) \frac{1}{\Lambda} \\ &= \frac{\Theta(\xi_0 - \Lambda) \Theta(\Lambda - \max\{|\bar{\omega}|, b\mu\})}{\Lambda}. \end{aligned} \quad (3.26)$$

Compared to the infinite-mass case [Eq. (A.40), Eq. (3.29)], we find the additional factor $\Theta(\Lambda - b\mu)$ and, thus, have the interpretation that the recoil energy cuts off the flow. This results in a real part (due to $\omega_D \rightarrow 0$) of the parquet formula with the modification

$$\ln \frac{|\bar{\omega}|}{\xi_0} \rightarrow \ln \frac{\max\{|\bar{\omega}|, b\mu\}}{\xi_0}. \quad (3.27)$$

Assuming that the analytic version of the full finite-mass parquet function has a similar effect in a neighborhood sufficiently close to the threshold, we arrive at the real-frequency result known from [9, 11, 12] and anticipated in Eq. (1.10):

$$\operatorname{Re} \Pi(\omega, 0) = \frac{1}{2U} \left[1 - \left(\frac{\max\{|\omega - \omega_D|, b\mu\}}{\xi_0} \right)^{-2u} \right]. \quad (3.28)$$

Yet, the above hand-waving arguments about the structure of the self-energy at variable scale in imaginary-frequency space seem rather tricky and far from optimal to decode single, physically distinctive features of the real-frequency particle-hole susceptibility.

3.4 Comparison to a related work

In a recent publication, Lange, Drukier, Sharma, and Kopietz (LDSK) [2] treated the X-ray-edge problem similarly as done in this work. In fact, it is their paper which has drawn our attention to the problem at hand and deeply inspired our approach. LDSK, too, obtain the parquet formula in the infinite-mass case and from this draw conclusions about the relation between parquet resummations and the functional renormalization group. We hope that our analysis has further elucidated the derivation of the analytic parquet result and added valuable arguments to the discussion about fRG and parquet graphs. Let us comment on various interesting points from LDSK's treatment in detail and relate them to our work.

Interchangeability of γ and χ : LDSK extract the particle-hole susceptibility from a bosonic (χ) self-energy arising from a multi-channel Hubbard-Stratonovich transformation in the exchange (χ , U_x) and pairing (ψ , U_p) channel with $U_x = U_p$. We have shown that χ couples similarly to fermions as the photon γ ; in fact, the leading-order self-energies of both γ and χ are given by the four-point correlator. Crucially however, to obtain the parquet result for the particle-hole susceptibility, only the leading-order χ self-energy (i.e., the part of the self-energy without internal χ propagation) can be used. This is easily seen in terms of diagrams: The χ self-energy at zeroth order is given by a conduction-valence-band particle-hole bubble. At first order in the interaction, it is only affected by ψ propagation, since an intermediate χ line would result in a reducible diagram. Hence, to fully account for the first-order ladder diagram, the ψ propagator must have full weight, $U_p = U$. On the other hand, at second and higher orders, irreducible diagrams with internal χ lines occur. Allowing for $U_x > 0$ then overcounts these contributions. Summarizing, the exact parquet graphs for the particle-hole susceptibility can only be reproduced from the χ self-energy by using $U_p = U$ and $U_x = 0$.

Interestingly enough, the latter choice simplifies the approximate analytic approach of LDSK compared to their choice $U_x = U_p$. In an integration of the frequency-independent, squared χ three-point vertex g_l from a logarithmic scale parameter $l = 0$ up to $l^* = \ln(\xi_0/|\bar{\omega}|)$, LDSK approximated $\cosh(2ul)$ by unity (Eq. (52) in [2]) although, in the first-order parquet regime, $u \ln(\xi_0/|\bar{\omega}|) \lesssim 1$. However, the need for such an approximation does not arise if one uses $U_x = 0$, since in the previous equation (Eq. (49) in [2]), $U_x = 0$, $U_p = U$ naturally yield $g_l = e^{2ul}$ instead of $g_l = e^{2ul}/\cosh(2ul)$. According to the diagrammatic argument above, it is not surprising that the error introduced by using $U_x \neq 0$ alters g_l and consequently the particle-hole susceptibility²¹ at second order in U , where $\cosh(2ul) \neq 1$.

It is worth noting that we were able to produce the parquet formula by employing a simplification of the fermionic four-point vertex and LDSK's argumentation remains valid for $U_x = 0$, i.e., without propagation in the exchange channel. Thus, our analysis suggests that a multi-channel Hubbard-Stratonovich approach has no advantage over the version advocated in this work, based on the flow in the light-matter system.

Restricted flow $\xi_0 \geq \Lambda \geq \bar{\omega}$: We find that our analytic study comparing different regulators can be used to shine light on the intriguing approximate derivation of the parquet formula presented by LDSK. They used an approximation scheme where frequency dependencies in all 1PI vertices were omitted initially. Viewing this as a low-energy approximation, they chose to perform the flow in parameter space from ξ_0 to $\bar{\omega}$ instead of the expected range ∞ to 0. The fact that this scheme successfully reproduces²² the

²¹Carrying out the calculation (Eq. (52) in [2]) including $\cosh(2ul)$ in the denominator yields the function $-\frac{p}{2u} \ln[(e^{2ul^*} + 1)/2]$, which deviates from the parquet formula starting at second order in u .

²²In fact, in logarithmic accuracy one only produces the real part after choosing $\xi^d = 0$ (cf. our discussion in section 3.3.2).

parquet result can also be seen from another perspective.

With $U_x = 0$, the three-point vertex $\tilde{\Gamma}^{\bar{c}d\psi}$ remains equal to unity, and, without bosonic self-energy reinsertions, $G^\psi = -U_p = -U$. Hence, the flow equations for Π^χ and $\Gamma^{\bar{c}d\chi}$ reduce to exactly the same ones as in Eq. (3.15) (with $\Gamma^{\bar{c}d\gamma}/i$ replaced by $\Gamma^{\bar{c}d\chi}$). In section 3.3, we have explained that the effect of $\bar{\omega}$ is limited to that of a parameter only relevant in the single-scale bubble [cf. Eq. (3.19)]. This single-scale bubble can be integrated first in frequency and then in parameter space (as done in section A.3), which is very simple making use of the δ regulator [Eq. (2.46)], $\xi^d = 0$ (such that $|\bar{\omega}| \ll \xi_0$), and the (simplified) local c propagator [Eq. (2.68)]:

$$\begin{aligned} \int_{\omega} S_{\Lambda, \omega}^d G_{\bar{\omega}+\omega}^c / \rho &= \int_{-\xi_0-\bar{\omega}}^{\xi_0-\bar{\omega}} d\omega \operatorname{sgn}(\bar{\omega} + \omega) \frac{\delta(|\omega| - \Lambda)}{2\omega} \\ &\approx \int_{-\xi_0}^{\xi_0} d\omega \operatorname{sgn}(\bar{\omega} + \omega) \frac{\delta(|\omega| - \Lambda)}{2\omega} \\ &= \Theta(\xi_0 - \Lambda) \sum_{\omega=\pm\Lambda} \frac{\operatorname{sgn}(\bar{\omega} + \omega)}{2\omega} = \frac{\Theta(\xi_0 - \Lambda)\Theta(\Lambda - |\bar{\omega}|)}{\Lambda}. \end{aligned} \quad (3.29)$$

Using this single-scale bubble as a factor in the relevant flow equations, similarly as in Eq. (3.16), naturally restricts the integration range for Λ precisely in the way chosen by LDSK.

Applications beyond: To focus on the diagrammatic representation of the flow equations most relevant for the particle-hole susceptibility, let us compare the flow of Π^χ , $\Gamma^{\bar{c}d\chi}$ (Figure 4 in [2]) and Π^γ , $\Gamma^{\bar{c}d\gamma}$ in Fig. 3.14. All of these exclusively contain antiparallel S^d - G^c lines. Therefore, the derivatives of diagrams with parallel G^d - G^c lines [as, e.g., coming from the crossed diagram (cf. Fig. 3.1)] are never fully generated. Obtaining a full result in this manner can only be possible due to fortuitous partial cancellation of diagrams. For the specific bare propagators of the X-ray-edge problem and for infinite hole mass, a cancellation due to relations such as $\Pi^{(2L)} = -3\Pi^{(2C)}$ holds with logarithmic accuracy (cf. section A.2). Already in the finite-mass case (cf. section 1.4) and surely for more general actions, such a cancellation can only occur if additional simplifying assumptions are made.

Staying with the (infinite-mass) X-ray-edge singularity but aspiring a higher-order parquet result, we have mentioned in section 3.3 that the relevant, full valence-band self-energy is symmetric in u . Merely inserting Σ^d in the existent analytic approach cannot suffice to produce a correction in the single-scale bubble linear in u , required for a second-order correction in the exponent of the particle-hole susceptibility.

As already indicated above, our calculation of Π^γ with the simplified $\tilde{\Gamma}^{\bar{d}d\bar{c}c} = -U$ is equivalent to the study of Π^χ as in LDSK's work using $U_x = 0$ and no insertion of Π^ψ . One can easily convince oneself that, to get parallel S^d - G^c lines, higher-order vertices like $\Gamma^{\bar{d}d\chi\bar{\chi}}$ (for Π^χ) or $\Gamma^{\bar{d}d\bar{c}d\chi}$ (for $\Gamma^{\bar{c}d\chi}$) are needed. Furthermore, we have already mentioned that $\Gamma^{\bar{d}d\bar{c}c}$ is of importance in the HS system starting at second order. We have numerically checked that the perfect agreement with the parquet result of the particle-hole susceptibility, obtained by using $U_x = 0$ (cf. Fig. 3.21), is spoilt when including bosonic self-energies, see Fig. 3.27. This applies to both subdivisions of the interaction strength, i.e., to $U_x = 0$, $U_p = U$ as well as to $U_x = U_p$. With two dynamic and equally contributing channels, $U_x = U_p = U/2$, the result is more similar to that of the parquet formula with $U/2$, since the effect of using $U_x > 0$ enters only at second and higher orders. As a minor remark, we attribute the numerical sensitivity, attested by strongly differing δ and Litim solutions, for $U_x = U_p$ to internal G^χ lines, containing themselves the singular self-energy (cf. section 2.3).

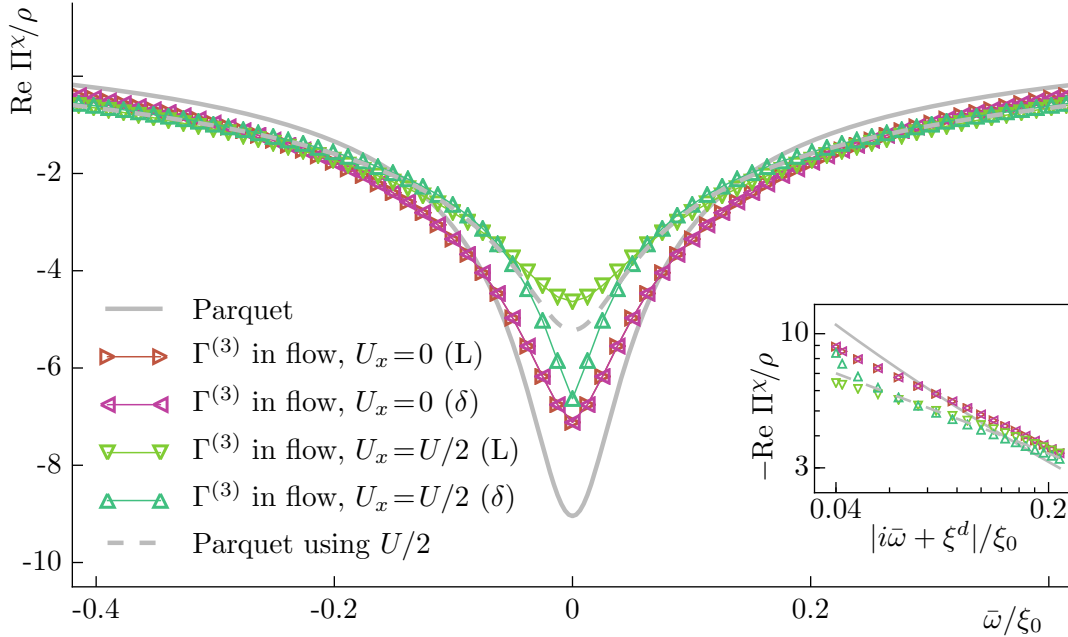


Figure 3.27: Self-energy in the exchange channel, Π^χ , obtained by a numerical solution of the flow equations in the HS-transformed system (section 2.2.5). Whereas using $U_x = 0$ and *no* reinsertion of bosonic self-energies during the flow is equivalent to the scenario which lead to perfect agreement (Fig. 3.21), allowing for a dynamic field in the pairing channel spoils the compatibility with the parquet result. Giving both HS fields equal weight, $U_x = U_p = U/2$, results in a curve more similar to the particle-hole susceptibility at $U/2$, since intermediate χ lines only occur at second order. The divergent nature of Π^χ present in full χ lines (if $U_x \neq 0$) is responsible for strong deviations between the two regulating schemes when $U_x > 0$.

3.5 Limitations of the fRG treatment

The parquet resummation covers all leading log. diagrams. As mentioned in section 1.4, these can be obtained by successively replacing bare vertices by parallel and antiparallel bubbles. It is not possible to reproduce all these parquet graphs from a truncated system of fRG flow equations for 1PI vertices. This is due to the simple fact that the parquet graphs comprise 1PI vertices of all orders. Consider, e.g., the flow of $\Gamma^{\bar{d}\bar{d}c}$ (cf. Fig. 3.9). Cutting a valence-band line that is not accompanied by a single conduction-band line yields to amputated d legs, thus generating a six-point vertex, which contributes to the flow via $\text{Tr} S_{d\bar{d}} \Gamma_{\bar{d}\bar{d}c}$. This can be iterated to arbitrarily high order without leaving the class of parquet graphs. The part of the flow equation

$$\partial_\Lambda \Gamma_{\Lambda, \alpha_1 \dots \alpha_n}^{(n)} = \text{Tr} \{ S_{d\bar{d}} \Gamma_{\Lambda, \bar{d} d \alpha_1 \dots \alpha_n}^{(n+2)} + \dots \} \quad (3.30)$$

is present for any $n \in 2\mathbb{N}$ [23] and requires the 1PI vertex of order two higher. This does not change at all after performing a Hubbard-Stratonovich transformation. In Fig. 3.12, we have seen that when computing the four-point vertex in the presence of auxiliary fields, leading log. diagrams start contributing at second order. Obviously, there exist one-particle-irreducible contributions at all orders in the coupling; e.g., the diagrams in Fig. 3.12 could be connected iteratively. Similarly to the procedure just described, by cutting d lines at appropriate places, higher-order 1PI vertices are generated, which encode indispensable parquet graphs.

Now, which ingredient of the parquet algebra of Roulet et al. [3] is missing in our treatment? It is the right classification of diagrams. Even though the language of *one*-particle-irreducible vertices decisively groups diagrams, we have just seen that parquet

graphs enter in 1PI vertices of arbitrary order. These diagrams are of divergent nature, and, consequently, leaving out any of these vertices is fatal. The proper parquet classification proceeds via reducibility in *two* lines. Any graph of $\Gamma^{(4)}$, which determines the four-point correlator of interest is either reducible in parallel or antiparallel c - d lines [3]. To relate such components of the four-point vertex self-consistently, one has to insert a vertex that is totally irreducible with respect to two lines (i.e., in both channels). This quantity no longer contains leading log. contributions and can be replaced by its trivial part: the bare interaction [3].

Using the Fermi-edge singularity as a counterexample, we can conclude that, in general, a truncated fRG flow formulated in terms of 1PI vertices is *not* equivalent to parquet resummation. Nonetheless, the fundamental Wetterich equation is exact and the computational flexibility thanks to the freedom of choice for the regulator is advantageous. It might therefore be worthwhile to consider different expansion and truncation schemes in the fRG flow. One might even step back and examine other functionals paraphrasing the many-body problem. Particularly, formulations of a two-particle-irreducible functional renormalization group (cf. e.g. [24]) seem suitable to reproduce the parquet algebra used in [3]. Such studies are, however, beyond the scope of this work.

4 Summary

In this work, we applied the functional renormalization group to the Fermi-edge singularity, aspiring to a resummation of diagrams as achieved by solving parquet equations. This problem—also referred to as X-ray-edge problem—is motivated by its experimental applications in, e.g., the vivid field of polariton physics as well as by its theoretical relevance, being a typical problem with a logarithmically diverging perturbation series. The quantity of interest is the particle-hole susceptibility, a four-point correlation function describing the evolution of a conduction-valence particle-hole pair in an interacting many-body environment.

The fRG formalism was motivated and developed in an imaginary-time action framework, transferring energy configurations in correlators and one-particle-irreducible vertices to discrete Matsubara frequencies. Its flow equations were set up for the different theories of a pure matter, Hubbard-Stratonovich-transformed matter, and a light-matter system. In the latter formulation, we expressed the particle-hole susceptibility as the leading-order contribution (in the light-matter coupling) to the photon self-energy. This seems natural talking about polariton physics, but can also be seen as a computational trick to incorporate an integrated, fermionic four-point correlator directly in the flow.

For an infinite valence-band (hole) mass, the different sets of differential equations were solved numerically. Among various solution schemes, we included a dynamic, fully frequency-dependent, fermionic four-point vertex and comparatively employed a δ and Litim regulator. Whereas the δ regulator not only proved useful for analytic calculations but is also favorable in terms of computational effort, results from a second, Litim-regulated procedure allowed to make statements about the error originating from an approximate solution of the fRG flow—without truncations all regulators would give equivalent results. In particular, we observed high numerical sensitivity to the choice of regulator when reinserting the divergent self-energy in the flow.

From the numerical data as well as from diagrammatic considerations, usually focused on low-order parquet graphs, we were able to draw a number of conclusions about the structure of solutions obtained from the fRG scheme. First, we constructed the four-point correlator from fully evolved 1PI vertices. We found that including dynamic HS fields in the exchange and pairing channel does not suffice for a parquet-like resummation. In fact, although the HS transformation ensures that the fermionic four-point vertex does not contribute to first order, it does comprise important parquet graphs starting at second order. A numerical solution of the particle-hole susceptibility matched the parquet result much better if the fermionic four-point vertex was used without a HS transformation. As we included the photon into the flow, extracting the correlator from the self-energy, the truncated flow equations relating the photon self-energy, three-point vertex, and full, fermionic four-point vertex were shown to dismiss relevant contributions from parallel bubbles. The numerical solution followed the prediction reasonably well but still worse than when evolving only the four-point vertex. Finally, a perfect match of numerical curves to the parquet formula was obtained in the light-matter system as the fermionic four-point vertex was kept constant at its initial value—the bare interaction. We diagrammatically proved that ladder diagrams are generated with the correct prefactor at all orders. The perfect match is thus due to a partial cancellation procedure. Intermediate quantities such as the interacting three-point vertex between a photon and a particle-hole pair are mistreated—one loses any dependence on a fermionic energy.

However, for the particle-hole susceptibility, the simplified flow generates the right result; we explicitly illustrated the partial cancellation of crossed and ladder contributions at second order.

This reproduction of the parquet formula was also performed analytically. Setting any 1PI vertex starting from four-point vertices to their initial value, we exactly solved the corresponding system of flow equations in the light-matter system. The simplification is due to the reduced frequency dependence of the three-point vertex, reminiscent of the effective ladder structure. The infinite-mass parquet result was recovered without further approximations. For an exponentially small mass ratio, where the above mentioned cancellations are still expected to hold, hand-waving arguments allowed us to reproduce an infrared cutoff, which was related to the recoil energy of the valence-band hole.

Judging from our treatment of the Fermi-edge singularity as a counter-example, a solution of a truncated fRG flow expanded in terms of one-particle-irreducible vertices is in general not able to resum all parquet graphs; n -point vertices for arbitrarily high n contain singular, non-negligible contributions irrespective of the introduction of Hubbard-Stratonovich fields or inclusion of photonic vertices in the flow. Compared to the parquet algebra of Roulet et al. [3], the classification into diagrams irreducible in two lines is not performed and the reduction to the regular, totally irreducible vertex not possible. Nonetheless, the flexibility and computational access of the fRG flow has allowed us to resolve the infrared divergence of the particle-hole susceptibility extraordinarily well. Even if not incorporating the fortuitous partial cancellation of diagrams, we found very good agreement to the predicted power law. For future studies, we suggest the consideration of different expansion and truncation techniques and especially point out the development of two-particle-irreducible fRG formulations in order to find equivalent resummation procedures to the solution of parquet equations.

References

- [1] T. Giamarchi. *Quantum Physics in One Dimension*. Oxford University Press Inc., New York (2003).
- [2] P. Lange, C. Drukier, A. Sharma, P. Kopietz. *Summing parquet diagrams using the functional renormalization group: X-ray problem revisited*. Journal of Physics A: Math. Theor. **48**, 395001 (2015).
- [3] B. Roulet, J. Gavoret, P. Nozières. *Singularities in the X-Ray Absorption and Emission of Metals. I. First-Order Parquet Calculation*. Phys. Rev. **178**, 1072 (1969).
- [4] S. Smolka, W. Wuester, F. Haupt, S. Faelt, W. Wegscheider, A. Imamoglu. *Cavity quantum electrodynamics with many-body states of a two-dimensional electron gas*. Science **346**, 6207 (2014).
- [5] P. Nozières, C. T. De Dominicis. *Singularities in the X-Ray Absorption and Emission of Metals. III. One-Body Theory Exact Solution*. Phys. Rev. **178**, 1084 (1969).
- [6] I. Carusotto, C. Ciuti. *Quantum Fluids of Light*. Rev. Mod. Phys. **85**, 299 (2013).
- [7] M. Sidler, P. Back, O. Cotlet, A. Srivastava, T. Fink, M. Kroner, E. Demler, A. Imamoglu. *Fermi polaron-polaritons in charge-tunable atomically thin semiconductors*. arXiv:1603.09215 (2016).
- [8] G. D. Mahan. *Excitons in Degenerate Semiconductors*. Phys. Rev. **153**, 882 (1967).
- [9] J. Gavoret, P. Nozières, B. Roulet, and M. Combescot. *Optical Absorption in Degenerate Semiconductors*. Journal de Physique, 30 (11-12), 987 (1969).
- [10] P. Nozières, J. Gavoret, B. Roulet. *Singularities in the X-Ray Absorption and Emission of Metals. II. Self-Consistent Treatment of Divergences*. Phys. Rev. **178**, 1084 (1969).
- [11] D. Pimenov. *Fermi-edge polaritons for finite hole mass*. Master's Thesis at LMU Munich (2015).
- [12] D. Pimenov, J. von Delft, L. Glazman, M. Goldstein. *Fermi-edge exciton-polaritons in doped semiconductor microcavities with finite hole mass*. To be published.
- [13] M. Baeten, M. Wouters. *Polariton formation in a microcavity with a doped quantum well: Roles of the Fermi edge singularity and Anderson orthogonality catastrophe*. Phys. Rev. B **89**, 245301 (2014).
- [14] M. Baeten, M. Wouters. *Mahan polaritons and their lifetime due to hole recoil*. Eur. Phys. J. D, 69: 243 (2015).
- [15] G. D. Mahan. *Excitons in Metals: Infinite Hole Mass*. Phys. Rev. **163**, 612 (1967).
- [16] Y. Yamamoto, A. Imamoglu. *Mesoscopic Quantum Optics*. John Wiley & Sons, Inc., New York, Vol. 1 (1999).
- [17] C. F. Klingshirn. *Semiconductor Optics*. Springer-Verlag, Berlin Heidelberg (2007).

- [18] P. Kopietz, L. Bartosch, F. Schütz. *Introduction to the Functional Renormalization Group*. Lecture Notes Phys. 789. Springer-Verlag, Berlin Heidelberg (2010).
- [19] C. Wetterich. *Exact evolution equation for the effective potential*. Phys. Lett. B **301**, 90 (1993).
- [20] D. F. Litim. *Optimized renormalization group flows*. Phys. Rev. D **64**, 105007 (2001).
- [21] S. Jakobs. *Renormierungsgruppen-Methoden für nichtlinearen Transport*. Diploma Thesis at RWTH Aachen (2003).
- [22] C. Karrasch. *The Functional Renormalization Group for Zero-Dimensional Quantum Systems in and out of Equilibrium*. PhD Thesis at RWTH Aachen (2010).
- [23] V. Meden. *Lecture Notes on the Functional Renormalization Group*. (2003).
- [24] J. F. Rentrop, S. G. Jakobs, V. Meden. *Two-particle irreducible functional renormalization group schemes—a comparative study*. J. Phys. A: Math. Theor. **48**, 145002 (2015).

A Appendix

A.1 Derivation of the flow equation

The derivation of the fundamental fRG flow equation, as already sketched in section 2.2.2, starts with the modified quadratic part of the action

$$S_{0,\Lambda}[\Phi] = -\frac{1}{2}(\Phi, G_{0,\Lambda}^{-1}\Phi) . \quad (\text{A.1})$$

Our aim is to see how this functional dependence is carried over to the 1PI generating functional Γ in terms of a derivative. According to the equation

$$\Gamma_\Lambda[\Phi] = (J_\Lambda[\bar{\Phi}], \bar{\Phi}) - \mathcal{G}_{c,\Lambda}[J_\Lambda[\bar{\Phi}]] + \frac{1}{2}(\bar{\Phi}, G_{0,\Lambda}^{-1}\bar{\Phi}) , \quad (\text{A.2})$$

it is sensible to start by differentiating the generating functional for connected Green's functions with respect to the flow parameter. We have

$$\begin{aligned} \partial_\Lambda \mathcal{G}_{c,\Lambda}[J] &= \partial_\Lambda \ln \frac{\int \mathcal{D}[\Phi] e^{-S_{0,\Lambda}[\Phi] - S_1[\Phi] + (J,\Phi)}}{\int \mathcal{D}[\Phi] e^{-S_{0,\Lambda}[\Phi]}} \\ &= \partial_\Lambda \ln \int \mathcal{D}[\Phi] e^{-S_{0,\Lambda}[\Phi] - S_1[\Phi] + (J,\Phi)} - \partial_\Lambda \ln Z_{0,\Lambda} , \end{aligned} \quad (\text{A.3})$$

and further

$$\begin{aligned} \partial_\Lambda \ln \int \mathcal{D}[\Phi] e^{-S_{0,\Lambda}[\Phi] - S_1[\Phi] + (J,\Phi)} &= \frac{1}{\int \mathcal{D}[\Phi] e^{-S[\Phi] + (J,\Phi)}} \partial_\Lambda \int \mathcal{D}[\Phi] e^{-S_{0,\Lambda}[\Phi] - S_1[\Phi] + (J,\Phi)} \\ &= \frac{1}{\int \mathcal{D}[\Phi] e^{-S[\Phi] + (J,\Phi)}} \frac{1}{2} \int \mathcal{D}[\Phi] \left(\Phi, (\partial_\Lambda G_{0,\Lambda}^{-1}) \Phi \right) e^{-S+(J,\Phi)} \\ &= \frac{Z_{0,\Lambda}}{\int \mathcal{D}[\Phi] e^{-S+(J,\Phi)}} \frac{1}{2} \left(\frac{\delta}{\delta J}, (\partial_\Lambda G_{0,\Lambda}^{-1}) \frac{\delta}{\delta J} \right) \frac{\int \mathcal{D}[\Phi] e^{-S+(J,\Phi)}}{Z_{0,\Lambda}} \\ &= e^{-\mathcal{G}_{c,\Lambda}} \frac{1}{2} \left(\frac{\delta}{\delta J}, (\partial_\Lambda G_{0,\Lambda}^{-1}) \frac{\delta}{\delta J} \right) e^{\mathcal{G}_{c,\Lambda}} . \end{aligned} \quad (\text{A.4})$$

This expression can be rewritten as (summation over repeated indices)

$$\begin{aligned} \left(\partial_\Lambda [G_{0,\Lambda}^{-1}]_{\alpha\beta} \right) e^{-\mathcal{G}_{c,\Lambda}} \frac{\delta}{\delta J_\alpha} \frac{\delta}{\delta J_\beta} e^{\mathcal{G}_{c,\Lambda}} &= \left(\partial_\Lambda [G_{0,\Lambda}^{-1}]_{\alpha\beta} \right) \left(\frac{\delta \mathcal{G}_{c,\Lambda}}{\delta J_\alpha} \frac{\partial \mathcal{G}_{c,\Lambda}}{\partial J_\beta} + \frac{\delta^2 \mathcal{G}_{c,\Lambda}}{\delta J_\alpha \delta J_\beta} \right) \\ &= \left(\bar{\Phi}, (\partial_\Lambda G_{0,\Lambda}^{-1}) \bar{\Phi} \right) - (\partial_\Lambda [G_{0,\Lambda}^{-1}]_{\alpha\beta}) G_{\Lambda,\alpha\beta}^J , \end{aligned} \quad (\text{A.5})$$

where the Green's function in presence of sources $G_{\Lambda,\alpha\beta}^J$ is fundamentally related to the Legendre transform of \mathcal{G}_c . By definition, we have

$$\mathcal{L}[\bar{\Phi}] = (J[\bar{\Phi}], \bar{\Phi}) - \mathcal{G}_c[J[\bar{\Phi}]] , \quad \frac{\delta \mathcal{L}[\bar{\Phi}]}{\delta \bar{\Phi}_\alpha} = \zeta_\alpha J_\alpha , \quad (\text{A.6})$$

and a short calculation shows

$$\delta_{\alpha,\gamma} = \frac{\delta \bar{\Phi}_\gamma}{\delta \bar{\Phi}_\alpha} = \frac{\delta J_\beta}{\delta \bar{\Phi}_\alpha} \frac{\delta \bar{\Phi}_\gamma}{\delta J_\beta} = \zeta_\beta \frac{\delta^2 \mathcal{L}}{\delta \bar{\Phi}_\alpha \delta \bar{\Phi}_\beta} \frac{\delta^2 \mathcal{G}_c}{\delta J_\beta \delta J_\gamma} = -\frac{\delta^2 \mathcal{L}}{\delta \bar{\Phi}_\alpha \delta \bar{\Phi}_\beta} G_{\gamma\beta}^J . \quad (\text{A.7})$$

It directly follows that

$$G_{\gamma\beta}^J = - \left[\left(\frac{\delta^2 \mathcal{L}}{\delta \bar{\Phi} \delta \Phi} \right)^{-1} \right]_{\beta\gamma}, \quad \text{where} \quad \left[\frac{\delta^2 \mathcal{L}}{\delta \bar{\Phi} \delta \Phi} \right]_{\alpha\beta} = \frac{\delta^2 \mathcal{L}}{\delta \bar{\Phi}_\alpha \delta \Phi_\beta}. \quad (\text{A.8})$$

We summarize, using transposition and the supertrace (which subjoins ζ , i.e., a minus sign for fermions, to the summation index),

$$\begin{aligned} \partial_\Lambda \mathcal{G}_{c,\Lambda}[J] - \frac{1}{2} (\bar{\Phi}, (\partial_\Lambda G_{0,\Lambda}^{-1}) \bar{\Phi}) &= -\frac{1}{2} (\partial_\Lambda [G_{0,\Lambda}^{-1}]_{\alpha\beta}) G_{\Lambda,\alpha\beta}^J - \partial_\Lambda \ln Z_{0,\Lambda} \\ &= \frac{1}{2} (\partial_\Lambda [G_{0,\Lambda}^{-1}]_{\alpha\beta}) \left\{ \left[\left(\frac{\delta^2 \mathcal{L}}{\delta \bar{\Phi} \delta \Phi} \right)^{-1} \right]_{\beta\alpha} + G_{0,\Lambda,\alpha\beta} \right\} \\ &= \frac{1}{2} \text{STr} \left\{ (\partial_\Lambda [G_{0,\Lambda}^{-1}]) \left[\left(\frac{\delta^2 \mathcal{L}}{\delta \bar{\Phi} \delta \Phi} \right)^{-1, \text{T}} + G_{0,\Lambda} \right] \right\}. \end{aligned} \quad (\text{A.9})$$

Finally, for the 1PI generating functional, we have

$$\Gamma_\Lambda[\Phi] = (J_\Lambda[\bar{\Phi}], \bar{\Phi}) - \mathcal{G}_{c,\Lambda}[J_\Lambda[\bar{\Phi}]] + \frac{1}{2} (\bar{\Phi}, G_{0,\Lambda}^{-1} \bar{\Phi}), \quad (\text{A.10})$$

and due to a typical cancellation in the derivatives of the first two summands

$$\begin{aligned} \partial_\Lambda \Gamma_\Lambda[\Phi] &= -\partial_\Lambda \mathcal{G}_{c,\Lambda}[J] \Big|_{J=J_\Lambda[\bar{\Phi}]} + \frac{1}{2} (\bar{\Phi}, \partial_\Lambda G_{0,\Lambda}^{-1} \bar{\Phi}) \\ &= -\frac{1}{2} \text{STr} \left\{ (\partial_\Lambda G_{0,\Lambda}^{-1}) \left(\left[\left(\frac{\delta^2 \Gamma_\Lambda[\bar{\Phi}]}{\delta \bar{\Phi} \delta \Phi} \right)^{\text{T}} - G_{0,\Lambda}^{-1} \right]^{-1} + G_{0,\Lambda} \right) \right\}. \end{aligned} \quad (\text{A.11})$$

This is the flow equation for the generating functional of the one-particle-irreducible vertices stated in Eq. (2.51).

A.2 Ladder diagrams and the crossed diagram

We will derive explicit expressions for the diagrams which determine the four-point correlator up to second order in the interaction parameter U . We confine ourselves to infinite hole mass and calculations in the zero-temperature limit with logarithmic accuracy. As already explained, in this work, a diagram exclusively specifies the propagators and their functional dependencies, which are integrated over. Each vertex requires energy-momentum conservation and a multiplication by $-U$.

In section 2.3, we already argued that, due to the immobile valence-band hole, the correlation function is only frequency-dependent. The conduction-band propagator appears in its local form [cf. Eq. (2.68)].

Ladder diagrams, like the first three ones in Fig. A.1, factorize for each bubble and can therefore be calculated at any order. One has

$$\Pi^{(n,L)} = (-U)^n \left(\Pi^{(0L)} \right)^{n+1}, \quad \Pi^{(0L)}(\bar{\omega}) = \int_\omega G_{\omega-\bar{\omega}}^d G_\omega^c. \quad (\text{A.12})$$

In the zero-temperate limit, the integral is evaluated to be

$$\frac{-i\pi\rho}{2\pi} \int_{-\xi_0}^{\xi_0} d\omega \frac{\text{sgn}(\omega)}{i\omega - i\bar{\omega} - \xi^d} = \frac{\rho}{2} \left[\ln \left(\frac{-i\bar{\omega} - \xi^d}{i\xi_0 - i\bar{\omega} - \xi^d} \right) + \ln \left(\frac{-i\bar{\omega} - \xi^d}{-i\xi_0 - i\bar{\omega} - \xi^d} \right) \right]. \quad (\text{A.13})$$

Note that $-\xi^d = \mu - E_0 = E_G + \mu = \omega_0$ is the threshold frequency for photon absorption. After analytic continuation $i\bar{\omega} \rightarrow \omega + i0^+$, $\omega - \omega_0$ will be very small, in

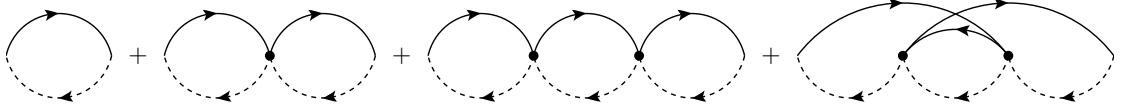


Figure A.1: Four-point correlator $\langle \bar{d}d\bar{c}c \rangle$ up to second order, consisting of the first three ladder diagrams [(0L), (1L), (2L)] and the crossed diagram [(2C)].

particular small compared to ξ_0 . Therefore, we can make the approximation $\pm i\xi_0 - i\bar{\omega} - \xi^d \approx \pm i\xi_0$ and have the simplified form

$$\Pi^{(0L)}(\bar{\omega}) \approx \rho \ln \left(\frac{-i\bar{\omega} - \xi^d}{\xi_0} \right), \quad \Pi^{(n,L)}(\bar{\omega}) \approx (-U)^n \left[\rho \ln \left(\frac{-i\bar{\omega} - \xi^d}{\xi_0} \right) \right]^{n+1}. \quad (\text{A.14})$$

In Eq. (A.13), the real additive $-\xi^d = \omega_0$ has shifted the argument of the logarithm away from the negative real axis and therefore saved us any troubles with the logarithm's branch cut. When we carry the external frequency $\bar{\omega}$ always in the d propagator, we can spare notation by including ξ^d in $i\bar{\omega}$ and perform the analytic continuation afterwards by $i\bar{\omega} \rightarrow \omega - \omega_0 + i0^+$. Yet, we have to keep in mind the real part in $i\bar{\omega}$ for the logarithms to be well-defined. More details are given in the next section.

Employing this, let us calculate the crossed diagram (the fourth one in Fig. A.1). The integral we have to compute [cf. Eq. (3.4)] is

$$\begin{aligned} \mathcal{I} &= \int_{\omega, \nu, \eta}''' G_{\omega-\bar{\omega}}^d G_{\omega+\nu-\eta-\bar{\omega}}^d G_{\nu-\bar{\omega}}^d G_{\omega}^c G_{\nu}^c G_{\eta}^c \\ &= \left(\frac{-i\pi\rho}{2\pi} \right)^3 \int_{-\xi_0}^{\xi_0} d\omega d\nu d\eta \frac{\text{sgn}(\omega)}{i\omega - i\bar{\omega}} \frac{\text{sgn}(\nu)}{i\nu - i\bar{\omega}} \frac{\text{sgn}(\eta)}{i\omega + i\nu - i\eta - i\bar{\omega}}. \end{aligned} \quad (\text{A.15})$$

We begin by integrating over η :

$$\int_{-\xi_0}^{\xi_0} d\eta \frac{\text{sgn}(\eta)}{i\bar{\Omega} - i\eta} = i \ln \left(\frac{i\bar{\Omega} - i\xi_0}{i\bar{\Omega}} \right) + i \ln \left(\frac{i\bar{\Omega} + i\xi_0}{i\bar{\Omega}} \right) \approx -2i \ln \left(\frac{i\bar{\Omega}}{\xi_0} \right). \quad (\text{A.16})$$

Here, $\bar{\Omega} = \omega + \nu - \bar{\omega}$ is composed of integration variables and not always small compared to ξ_0 . However, in order to proceed with a simple calculation, we make the more severe approximation anyhow to obtain

$$\mathcal{I} \approx \frac{\rho^3}{4} \int_{-\xi_0}^{\xi_0} d\omega d\nu \frac{\text{sgn}(\omega)}{i\omega - i\bar{\omega}} \frac{\text{sgn}(\nu)}{i\nu - i\bar{\omega}} \ln \left(\frac{i\omega - i\bar{\omega} + i\nu}{\xi_0} \right). \quad (\text{A.17})$$

For the next integral, let us first use symmetry

$$\begin{aligned} &\int_{-\xi_0}^{\xi_0} d\nu \frac{\text{sgn}(\nu)}{i\nu - i\bar{\omega}} \ln \left(\frac{i\omega - i\bar{\omega} + i\nu}{\xi_0} \right) \\ &= \int_0^{\xi_0} d\nu \frac{1}{i\nu - i\bar{\omega}} \ln \left(\frac{i\omega - i\bar{\omega} + i\nu}{\xi_0} \right) + [(\xi_0, \omega, \bar{\omega}) \rightarrow -(\xi_0, \omega, \bar{\omega})] \end{aligned} \quad (\text{A.18})$$

and then employ logarithmic accuracy via

$$\ln \left(i\omega + i\nu - i\bar{\omega} \right) \approx \ln \left(i \max\{\omega, \nu\} - i\bar{\omega} \right). \quad (\text{A.19})$$

With the known approximation of a dominant ξ_0 in succeeding steps, we get

$$\begin{aligned} \int_0^{\xi_0} \frac{d\nu}{i\nu - i\bar{\omega}} \ln \left(\frac{i\omega - i\bar{\omega} + i\nu}{\xi_0} \right) &\approx \int_0^{\omega} \frac{d\nu}{i\nu - i\bar{\omega}} \ln \left(\frac{i\omega - i\bar{\omega}}{\xi_0} \right) + \int_{\omega}^{\xi_0} \frac{d\nu}{i\nu - i\bar{\omega}} \ln \left(\frac{i\nu - i\bar{\omega}}{\xi_0} \right) \\ &= -i \ln \left(\frac{i\omega - i\bar{\omega}}{-i\bar{\omega}} \right) \ln \left(\frac{i\omega - i\bar{\omega}}{\xi_0} \right) - \frac{i}{2} \ln^2 \left(\frac{i\nu - i\bar{\omega}}{\xi_0} \right) \Big|_{\omega}^{\xi_0} \\ &\approx -i \ln \left(\frac{i\omega - i\bar{\omega}}{-i\bar{\omega}} \right) \ln \left(\frac{i\omega - i\bar{\omega}}{\xi_0} \right) + \frac{i}{2} \ln^2 \left(\frac{i\omega - i\bar{\omega}}{\xi_0} \right) \end{aligned} \quad (\text{A.20})$$

and in total

$$\begin{aligned}
\mathcal{I} &\approx \frac{i\rho^3}{2} \int_{-\xi_0}^{\xi_0} d\omega \frac{\text{sgn}(\omega)}{i\omega - i\bar{\omega}} \left[\frac{1}{2} \ln^2 \left(\frac{i\omega - i\bar{\omega}}{\xi_0} \right) - \ln \left(\frac{i\omega - i\bar{\omega}}{-i\bar{\omega}} \right) \ln \left(\frac{i\omega - i\bar{\omega}}{\xi_0} \right) \right] \\
&= \frac{i\rho^3}{2} \int_0^{\xi_0} \frac{d\omega}{i\omega - i\bar{\omega}} \left[\frac{1}{2} \ln^2 \left(\frac{i\omega - i\bar{\omega}}{\xi_0} \right) - \ln \left(\frac{i\omega - i\bar{\omega}}{-i\bar{\omega}} \right) \ln \left(\frac{i\omega - i\bar{\omega}}{\xi_0} \right) \right] \\
&\quad + [(\xi_0, \bar{\omega}) \rightarrow -(\xi_0, \bar{\omega})] .
\end{aligned} \tag{A.21}$$

Starting from left, we finally calculate

$$\begin{aligned}
\frac{1}{2} \int_0^{\xi_0} \frac{d\nu}{i\nu - i\bar{\omega}} \ln^2 \left(\frac{i\nu - i\bar{\omega}}{\xi_0} \right) &= \frac{-i}{6} \ln^3 \left(\frac{i\nu - i\bar{\omega}}{\xi_0} \right) \Big|_0^{\xi_0} \approx \frac{i}{6} \ln^3 \left(\frac{-i\bar{\omega}}{\xi_0} \right) , \\
- \int_0^{\xi_0} \frac{d\nu}{i\nu - i\bar{\omega}} \ln \left(\frac{i\nu - i\bar{\omega}}{-i\bar{\omega}} \right) \ln \left(\frac{i\nu - i\bar{\omega}}{\xi_0} \right) \\
&= - \int_0^{\xi_0} \frac{d\nu}{i\nu - i\bar{\omega}} \left[\ln \left(\frac{i\nu - i\bar{\omega}}{\xi_0} \right) - \ln \left(\frac{-i\bar{\omega}}{\xi_0} \right) \right] \ln \left(\frac{i\nu - i\bar{\omega}}{\xi_0} \right) \\
&= \frac{i}{3} \ln^3 \left(\frac{i\nu - i\bar{\omega}}{\xi_0} \right) \Big|_0^{\xi_0} - \frac{i}{2} \ln^2 \left(\frac{i\nu - i\bar{\omega}}{\xi_0} \right) \Big|_0^{\xi_0} \ln \left(\frac{-i\bar{\omega}}{\xi_0} \right) \approx \frac{i}{6} \ln^3 \left(\frac{-i\bar{\omega}}{\xi_0} \right) .
\end{aligned} \tag{A.22}$$

Bringing everything together and reinserting the shift, it remains the simple result

$$\Pi^{(2C)}(\bar{\omega}) = U^2 \mathcal{I} \approx -U^2 \frac{\rho^3}{3} \ln^3 \left(\frac{-i\bar{\omega} - \xi^d}{\xi_0} \right) \approx -\frac{1}{3} \Pi^{(2L)}(\bar{\omega}) , \tag{A.23}$$

and we see that the crossed diagram takes away part of the weight of the ladder diagram.

A.3 Calculations of the single-scale bubble

In the following, we will calculate the single-scale bubble $\int_{\omega}^{\prime} S_{\Lambda, \omega}^d G_{\bar{\omega}+\omega}^c / \rho$ for infinite hole mass and the different regulating schemes [cf. Eq. (2.43)]. Since without fermionic self-energies $S_{\Lambda, \omega}^d = \partial_{\Lambda} G_{\Lambda, \omega}^d$, it is the total derivative of the particle-hole bubble, for the use in Eq. (3.19), where the single-scale bubble is integrated in parameter space, such a procedure is merely a computational gimmick. However, in the finite-mass case (section 3.3.2) and for some arguments in this work, we use the single-scale bubble; plus, for insight into the regulating scheme, it is interesting to perform the calculation. In order to point out the relevance of the real constant $-\xi^d = E_G + \mu = \omega_0$ in the valence-band propagator $G^d = 1/(i\omega - \xi^d)$, let us take a step back to the ordinary particle-hole bubble. The integral [using the local c propagator, Eq. (2.68)]

$$I(\bar{\omega}) = \int_{\omega}^{\prime} G_{\omega}^d G_{\bar{\omega}+\omega}^c / \rho = \frac{-i}{2} \int_{-\xi_0 - \bar{\omega}}^{\xi_0 - \bar{\omega}} d\omega \frac{\text{sgn}\bar{\omega} + (\omega)}{i\omega - \xi^d} \tag{A.24}$$

can be divided into three sections, and due to general Matsubara Green's function properties, it is sufficient to calculate the integrals for $\bar{\omega} > 0$:

$$\begin{aligned}
[-\xi_0 - \bar{\omega}, \xi_0 - \bar{\omega}] &= [-\xi_0 - \bar{\omega}, -\bar{\omega}] \cup [-\bar{\omega}, \bar{\omega}] \cup (\bar{\omega}, \xi_0 - \bar{\omega}) , \\
I &= I_1 + I_2 + I_3 , \quad I(-\bar{\omega}) = I(\bar{\omega})^* .
\end{aligned} \tag{A.25}$$

With $\bar{\omega} > 0$, it is then computed as follows:

$$\begin{aligned} I_1 &= \frac{-i}{2} \int_{\bar{\omega}}^{\xi_0 - \bar{\omega}} \frac{d\omega}{i\omega - \xi^d} = \frac{1}{2} \ln \left(\frac{i\bar{\omega} - \xi^d}{i\xi_0 - i\bar{\omega} - \xi^d} \right), \\ I_2 &= \frac{-i}{2} \int_{-\bar{\omega}}^{\bar{\omega}} \frac{d\omega}{i\omega - \xi^d} = \frac{1}{2} \ln \left(\frac{-i\bar{\omega} - \xi^d}{i\bar{\omega} - \xi^d} \right), \end{aligned} \quad (\text{A.26})$$

$$I_2 = i \int_0^{\bar{\omega}} d\omega \frac{\xi^d}{(\xi^d)^2 + (\bar{\omega})^2} = i \arctan \left(\frac{\bar{\omega}}{\xi^d} \right), \quad (\text{A.27})$$

$$I_3 = \frac{i}{2} \int_{-\xi_0 - \bar{\omega}}^{-\bar{\omega}} \frac{d\omega}{i\omega - \xi^d} = \frac{1}{2} \ln \left(\frac{-i\bar{\omega} - \xi^d}{-i\xi_0 - i\bar{\omega} - \xi^d} \right). \quad (\text{A.28})$$

We have written I_2 in two ways. In Eq. (A.26), we see that, by addition of I_1 and I_2 , the numerator in the logarithm's argument of I_1 is adjusted. Only then, we get, using the argument that upon continuation $i\bar{\omega} + \xi^d \rightarrow \omega - \omega_0 + i0^+ \ll \xi_0$, the correct result,

$$\begin{aligned} I &= \frac{1}{2} \ln \left(\frac{-i\bar{\omega} - \xi^d}{i\xi_0 - i\bar{\omega} - \xi^d} \right) + \frac{1}{2} \ln \left(\frac{-i\bar{\omega} - \xi^d}{-i\xi_0 - i\bar{\omega} - \xi^d} \right) \\ &\approx \frac{1}{2} \ln \left(\frac{-i\bar{\omega} - \xi^d}{i\xi_0} \right) + \frac{1}{2} \ln \left(\frac{-i\bar{\omega} - \xi^d}{-i\xi_0} \right) = \left(\frac{-i\bar{\omega} - \xi^d}{\xi_0} \right) \\ &\rightarrow \ln \left(\frac{-(\omega - \omega_0) - i0^+}{\xi_0} \right). \end{aligned} \quad (\text{A.29})$$

In the end, I depends on precisely the same expression $-i\bar{\omega} - \xi^d$ as the propagator $G_{\omega - \bar{\omega}}^d = 1/(i\omega - i\bar{\omega} - \xi^d)$. Can one ignore ξ^d in all calculations and reinsert it by continuing $i\bar{\omega} \rightarrow \omega - \omega_0 + i0^+ \ll \xi_0$ at the end? No, one cannot, since intermediate calculations, such as the integral I_2 , are discontinuous with respect to ξ^d at $\xi^d = 0$. For illustration, we initially set $\xi^d = 0$ in Eq. (A.27), I_2 vanishes²³, and one gets

$$\begin{aligned} \tilde{I} &= \frac{1}{2} \ln \left(\frac{i\bar{\omega}}{i\xi_0 - i\bar{\omega}} \right) + \frac{1}{2} \ln \left(\frac{-i\bar{\omega}}{-i\xi_0 - i\bar{\omega}} \right) \approx \frac{1}{2} \ln \left(\frac{i\bar{\omega}}{i\xi_0} \right) + \frac{1}{2} \ln \left(\frac{-i\bar{\omega}}{-i\xi_0} \right) \\ &\approx \ln \left(\frac{\bar{\omega}}{\xi_0} \right), \quad \bar{\omega} > 0 \quad \Rightarrow \quad \tilde{I} = \ln \left(\frac{|\bar{\omega}|}{\xi_0} \right). \end{aligned} \quad (\text{A.30})$$

This result is still useful, since it correctly gives the logarithmic singularity of the bubble. Only the logarithm's phase, being of order one, is ignored. However, the analytic structure of a Green's function is lost and has to be adjusted a posteriori.

Since the single-scale bubble is the derivative of the particle-hole bubble I , the same phenomenon occurs. Due to the boundary condition of a regulated propagator $G_{\Lambda=0} = G_{\Lambda}$, we have

$$I = I(\Lambda = 0), \quad I(\Lambda) = \int_{\omega}^{\prime} G_{\Lambda, \omega}^d G_{\bar{\omega} + \omega}^c / \rho, \quad I'(\Lambda) = \int_{\omega}^{\prime} S_{\Lambda, \omega}^d G_{\bar{\omega} + \omega}^c / \rho. \quad (\text{A.31})$$

Using the Litim regulator [Eq. (2.43)], the bubbles are given by

$$\begin{aligned} I_L(\Lambda) &= \frac{-i}{2} \int_{-\xi_0 - \bar{\omega}}^{\xi_0 - \bar{\omega}} d\omega \frac{\text{sgn}(\bar{\omega} + \omega)}{i\omega - \xi^d + i \text{sgn}(\omega)(\Lambda - |\omega|)\Theta(\Lambda - |\omega|)}, \\ I_L'(\Lambda) &= \frac{-1}{2} \int_{-\xi_0 - \bar{\omega}}^{\xi_0 - \bar{\omega}} d\omega \frac{\text{sgn}(\bar{\omega} + \omega) \text{sgn}(\omega) \Theta(\Lambda - |\omega|)}{[i \text{sgn}(\omega) \Lambda - \xi^d]^2}. \end{aligned} \quad (\text{A.32})$$

²³Note that, for a fermionic frequency ω and any temperature, $\frac{1}{\beta} \sum_{|\omega| < \Omega} \frac{1}{i\omega} = 0$ such that, even in the zero-temperature limit, $\int_{|\omega| < \Omega} \frac{1}{i\omega}$ is well-defined and equal to zero.

With the same division into three parts as in Eq. (A.28), one calculates

$$\begin{aligned}
I'_{L,1}(\Lambda) &= -\frac{1}{2} \int_{\bar{\omega}}^{\xi_0 - \bar{\omega}} d\omega \frac{\Theta(\Lambda - |\omega|)}{(i\Lambda - \xi^d)^2} = \Theta(\Lambda - |\bar{\omega}|) \frac{\min\{\Lambda, \xi_0 - \bar{\omega}\} - \bar{\omega}}{-2(i\Lambda - \xi^d)^2}, \\
\int_{\infty}^0 d\Lambda I'_{L,1}(\Lambda) &= -\frac{1}{2} \left[\int_{\infty}^{\xi_0 - \bar{\omega}} d\Lambda \frac{\xi_0 - 2\bar{\omega}}{(i\Lambda - \xi^d)^2} + \int_{\xi_0 - \bar{\omega}}^{\bar{\omega}} d\Lambda \frac{\Lambda - \bar{\omega}}{(i\Lambda - \xi^d)^2} \right] \\
&= \frac{1}{2} \ln \left(\frac{i\bar{\omega} - \xi^d}{i\xi_0 - i\bar{\omega} - \xi^d} \right), \tag{A.33}
\end{aligned}$$

as the non-logarithmic terms all cancel.

$$\begin{aligned}
I'_{L,2}(\Lambda) &= \frac{-1}{2} \int_{-\bar{\omega}}^{\bar{\omega}} d\omega \frac{\text{sgn}(\omega)\Theta(\Lambda - |\omega|)}{[i\text{sgn}(\omega)\Lambda - \xi^d]^2} = \frac{\min\{\Lambda, \bar{\omega}\}}{2(i\Lambda + \xi^d)^2} - \frac{\min\{\Lambda, \bar{\omega}\}}{2(i\Lambda - \xi^d)^2}, \\
\int_{\infty}^0 d\Lambda I'_{L,2}(\Lambda) &= \frac{1}{2} \int_{\infty}^{\bar{\omega}} d\Lambda \bar{\omega} \left[\frac{1}{(i\Lambda + \xi^d)^2} - \frac{1}{(i\Lambda - \xi^d)^2} \right] + \frac{1}{2} \int_{\bar{\omega}}^0 d\Lambda \Lambda \\
&\quad \times \left[\frac{1}{(i\Lambda + \xi^d)^2} - \frac{1}{(i\Lambda - \xi^d)^2} \right] = \frac{1}{2} \ln \left(\frac{-i\bar{\omega} - \xi^d}{i\bar{\omega} - \xi^d} \right). \tag{A.34}
\end{aligned}$$

As before, the final integral is already treated due to symmetry, and we conclude

$$\begin{aligned}
I'_{L,3}(\Lambda) &= \frac{-1}{2} \int_{-\xi_0 - \bar{\omega}}^{-\bar{\omega}} d\omega \frac{\Theta(\Lambda - |\omega|)}{(i\Lambda + \xi^d)^2} = I'_{L,1}(\Lambda)|_{\xi^d \rightarrow -\xi^d, \xi_0 \rightarrow \xi_0 + 2\bar{\omega}}, \\
\int_{\infty}^0 d\Lambda I'_{L,3}(\Lambda) &= \frac{1}{2} \ln \left(\frac{-i\bar{\omega} - \xi^d}{-i\xi_0 - i\bar{\omega} - \xi^d} \right), \quad \int_{\infty}^0 d\Lambda I'_L(\Lambda) = I. \tag{A.35}
\end{aligned}$$

Note that with the simplified usage of $\xi^d = 0$, $\xi_0 \gg \bar{\omega}$, the full derivative becomes

$$\tilde{I}'_L(\Lambda) = \Theta(\Lambda - |\bar{\omega}|) \frac{\min\{\Lambda, \xi_0\} - \bar{\omega}}{\Lambda^2}. \tag{A.36}$$

Only when integrating over the whole semiaxis, due to scale invariance of measure and boundaries, two parts cancel, and we get as expected:

$$\begin{aligned}
\int_{\infty}^0 \frac{d\Lambda}{\Lambda} \left[\Theta(\Lambda - \xi_0) \frac{\xi_0}{\Lambda} - \Theta(\Lambda - \bar{\omega}) \frac{\bar{\omega}}{\Lambda} \right] &= 0, \\
\int_{\infty}^0 d\Lambda \tilde{I}'_L(\Lambda) &= \int_{\xi_0}^{|\bar{\omega}|} \frac{d\Lambda}{\Lambda} = \ln \left(\frac{|\bar{\omega}|}{\xi_0} \right) = \tilde{I}. \tag{A.37}
\end{aligned}$$

With the δ regulator, the algebra is much simpler:

$$\begin{aligned}
I_{\delta}(\Lambda) &= -\frac{i}{2} \int_{-\xi_0 - \bar{\omega}}^{\xi_0 - \bar{\omega}} d\omega \text{sgn}(\bar{\omega} + \omega) \frac{\Theta(|\omega| - \Lambda)}{i\omega - \xi^d}, \\
I'_{\delta,1}(\Lambda) &= \frac{i}{2} \int_{\bar{\omega}}^{\xi_0 - \bar{\omega}} d\omega \frac{\delta(|\omega| - \Lambda)}{i\omega - \xi^d} = \frac{i}{2} \frac{\Theta(\Lambda - |\bar{\omega}|)\Theta(\xi_0 - \bar{\omega} - \Lambda)}{i\Lambda - \xi^d}, \\
I'_{\delta,2}(\Lambda) &= \frac{i}{2} \int_{-\bar{\omega}}^{\bar{\omega}} d\omega \frac{\delta(|\omega| - \Lambda)}{i\omega - \xi^d} = \frac{i\Theta(|\bar{\omega}| - \Lambda)}{2} \left(\frac{1}{i\Lambda - \xi^d} - \frac{1}{i\Lambda + \xi^d} \right), \\
I'_{\delta,3}(\Lambda) &= I'_{L,1}(\Lambda)|_{\xi^d \rightarrow -\xi^d, \xi_0 \rightarrow \xi_0 + 2\bar{\omega}}. \tag{A.38}
\end{aligned}$$

Naturally, one reproduces the correct results

$$\begin{aligned}
\int_{\infty}^0 d\Lambda I'_{\delta,1}(\Lambda) &= \int_{\xi_0 - \bar{\omega}}^{\bar{\omega}} d\Lambda \frac{i}{2} \frac{1}{i\Lambda - \xi^d} = \frac{1}{2} \ln \left(\frac{i\bar{\omega} - \xi^d}{i\xi_0 - i\bar{\omega} - \xi^d} \right), \\
\int_{\infty}^0 d\Lambda I'_{\delta,2}(\Lambda) &= \int_{-\bar{\omega}}^0 d\Lambda \frac{i}{2} \left(\frac{1}{i\Lambda - \xi^d} - \frac{1}{i\Lambda + \xi^d} \right) = \frac{1}{2} \ln \left(\frac{-i\bar{\omega} - \xi^d}{i\bar{\omega} - \xi^d} \right), \\
\int_{\infty}^0 d\Lambda I'_{\delta,3}(\Lambda) &= \frac{1}{2} \ln \left(\frac{-i\bar{\omega} - \xi^d}{-i\xi_0 - i\bar{\omega} - \xi^d} \right).
\end{aligned} \tag{A.39}$$

In this case, again using $\xi^d = 0$, $\xi_0 \gg \bar{\omega}$, the full derivative directly simplifies to the minimal structure:

$$\tilde{I}'_{\delta}(\Lambda) = \frac{\Theta(\Lambda - |\bar{\omega}|)\Theta(\xi_0 - \Lambda)}{\Lambda}, \quad \int_{\infty}^0 d\Lambda \tilde{I}'_{\delta}(\Lambda) = \int_{\xi_0}^{|\bar{\omega}|} \frac{d\Lambda}{\Lambda} = \ln \left(\frac{|\bar{\omega}|}{\xi_0} \right) = \tilde{I}. \tag{A.40}$$

Acknowledgment

I express my gratitude to Prof. Dr. Jan von Delft for the supervision of this thesis and for the opportunity to be part of his excellent and stimulating group. I also want to thank Prof. Dr. Matthias Punk for bringing my fascination to many-body physics and answering many questions. A special thanks goes to Dimitri Pimenov, Dennis Schimmel, and Lukas Weidinger for numerous very helpful discussions and to the whole group for providing an enjoyable environment in the course of this project.

Statement of Authorship

I hereby certify that this thesis is the result of my own work. Used material from published or unpublished work of others is referenced clearly in the text.

Fabian Kugler

Munich, September 1, 2016